Title
Electronic Band Structure Tuning of Highly-Mismatched-Alloys for Energy Conversion Applications

Author
Ting, Min

Publication Date
2016

Peer reviewed|Thesis/dissertation

Electronic Band Structure Tuning of Highly-Mismatched-Alloys for Energy Conversion Applications

by

Min Ting

A dissertation submitted in partial satisfaction of the

requirements for the degree of

Doctor of Philosophy

in

Engineering — Mechanical Engineering

in the

Graduate Division

of the

University of California, Berkeley

Committee in charge:

Professor Samuel S. Mao, Co-chair
Professor Ralph Greif, Co-chair
Professor Chris Dames
Professor Oscar Dubon

Summer 2017

Electronic Band Structure Tuning of Highly-Mismatched-Alloys for Energy Conversion Applications

Abstract

Electronic Band Structure Tuning of Highly-Mismatched-Alloys for Energy Conversion Applications

by

Min Ting

Doctor of Philosophy in Engineering — Mechanical Engineering

University of California, Berkeley

Professor Samuel S. Mao, Co-chair

Professor Ralph Greif, Co-chair

Highly-mismatched alloys: $ZnO_{1-x}Te_x$ and $GaN_{1-x}Sb_x$ are discussed within the context of finding the suitable material for a cost-effective Si-based tandem solar cell (SBTSC). SBTSC is an attractive concept for breaking through the energy conversion efficiency theoretical limit of a single junction solar cell. Combining with a material of 1.8 eV band gap, SBTSC can theoretically achieve energy conversion efficiency $> 45\%$.

ZnO and GaN are wide band gap semiconductors. Alloying Te in ZnO and alloying Sb in GaN result in large band gap reduction to < 2 eV from 3.3 eV and 3.4 eV respectively. The band gap reduction is majorly achieved by the upward shift of valence band (VB). Incorporating Te in ZnO modifies the VB of ZnO through the valence-band anticrossing (VBAC) interaction between localized Te states and ZnO VB delocalized states, which forms a Te-derived VB at 1 eV above the host VB. Similar band structure modification is resulted from alloying Sb in GaN. $ZnO_{1-x}Te_x$ and $GaN_{1-x}Sb_x$ thin films are synthesized across the whole composition range by pulsed laser deposition (PLD) and low temperature molecular beam epitaxy (LT-MBE) respectively. The electronic band edges of these alloys are measured by synchrotron X-ray absorption, emission, and the X-ray photoelectron spectroscopies. Modeling the optical absorption coefficient with the band anticrossing (BAC) model revealed that the Te and Sb defect levels to be at 0.99 eV and 1.2 eV above the VB of ZnO and GaN respectively. Electrically, $ZnO_{1-x}Te_x$ is readily n-type conductive and $GaN_{1-x}Sb_x$ is strongly p-type conductive. A heterojunction device of p-type $GaN_{0.93}Sb_{0.07}$ with n-type $ZnO_{0.77}Te_{0.93}$ upper cell (band gap at 1.8 eV) on Si bottom cell is proposed as a promising SBTSC device.

Contents

Contents **i**

List of Figures **iii**

List of Tables **viii**

1 Introduction **1**

2 Background **5**
2.1 ZnO and GaN material properties 5
2.2 Highly mismatched alloys and band anticrossing 5
2.3 This dissertation 9

3 $ZnO_{1-x}Te_x$ highly mismatched alloy synthesis and structural properties **11**
3.1 Pulsed laser deposition of $ZnO_{1-x}Te_x$ 11
3.2 Characterization techniques used in this chapter 13
3.3 Effects of growth on the structural and chemical properties 15
3.4 Summary 27

4 $ZnO_{1-x}Te_x$ electronic band structure **29**
4.1 Optical band gap measurement by optical absorption 29
4.2 Valence band edge measurement by X-ray photoelectron spectroscopy 31
4.3 Band edge measurements using synchrontron X-ray absorption / emission spectroscopies 34
4.4 Theoretical determination of the $ZnO_{1-x}Te_x$ dispersion relation 36
4.5 Summary 43

5 $ZnO_{1-x}Te_x$ doping and electrical properties **45**
5.1 Undoped $ZnO_{1-x}Te_x$ 45
5.2 P-type doping of $ZnO_{1-x}Te_x$ with nitrogen 48
5.3 Summary 51

6 $GaN_{1-x}Sb_x$ Synthesis and Electronic Band Structure **52**

6.1 Molecular beam epitaxy growth of $GaN_{1-x}Sb_x$ . . . 52
6.2 Growth conditions and structural properties . . . 53
6.3 Electronic band structure . . . 56
6.4 Summary . . . 60

7 $GaN_{1-x}Sb_x$ electrical properties **62**
7.1 Electrical properties of as-grown and annealed $GaN_{1-x}Sb_x$ . . . 62
7.2 BAC modeling of hole concentration . . . 67
7.3 Seebeck coefficient and thermoelectric application . . . 72
7.4 Enhanced P-type ohmic contact in GaN-based light emitting diodes . . . 73
7.5 Summary . . . 75

8 Energy conversion application and conclusion **76**
8.1 $ZnO_{1-x}Te_x$ / $GaN_{1-x}Sb_x$ on Si double junction solar cell . . . 76

9 Conclusion and outlook **83**

A Rutherford backscattering spectrometry **86**

B Nuclear reaction experiment for nitrogen detection **88**

C X-ray photoelectron spectroscopy full spectrum for $ZnO_{1-x}Te_x$ **91**

D Low temperature hall effect measurement of $GaN_{1-x}Sb_x$ **92**

E Low temperature hall effect measurement of $ZnO_{1-x}Te_x$ **94**

F Atomic force microscopy for $ZnO_{1-x}Te_x$ **97**

G Photoluminescence of $ZnO_{1-x}Te_x$ **99**

H Seebeck coefficient measurement **100**

Bibliography **102**

List of Figures

1.1 3-E trilemma, the most important task assigned to 21st century civilization. The key way to solve this trilemma is developing clean energy technologies. [38]. . . 1
1.2 The National Renewable Energy Laboratory (NREL) maintains a plot of compiled values of highest confirmed conversion efficiencies for research cells, from 1976 to the present, for a range of photovoltaic technologies. 2
1.3 The Shockley-Quessier (SQ) limit efficiency map for a double junction solar cell with respect to the E_{gap} of bottom and upper cells. The black line illustrates the efficiency limit when the bottom cell is Si with E_{gap} of 1.1 eV. [3] 3

2.1 An illustration of electronic band alignment between Si, ZnO, and GaN. 6
2.2 Conduction sub-band dispersion relations as predicted by the BAC model [120]. 7
2.3 Valence sub-band dispersion relations of $GaSb_{0.04}As_{0.96}$ [2]. 8
2.4 Dependence of the optical band gap energy on the value of x for crystalline and amorphous $GaN_{1-x}Asx$. Calculated composition dependence of the band gap of $GaN_{1-x}Asx$ alloys based on the Band anticrossing (BAC) and Virtual crystal approximation (VCA). [129] 9
2.5 An illustration of expected electronic band structure of Highly mismatched alloy (HMA) ZnOTe, and GaNSb. 10

3.1 Schematic of a Pulsed laser deposition (PLD) and ZnO laser ablation plume. . . 12
3.2 PLD growth chamber used in this study. The laser channel is positioned at 45° towards the target. The dimension of the PLD target is shown with the marked laser ablation spot. 14
3.3 The correlation of Te content between the PLD target and the resulting film. Te content measured by Rutherford backscattering spectroscopy (RBS) and X-ray diffraction (XRD) are shown as black squares and red triangles respectively. The dotted diagonal shows 1:1 ratio. 17
3.4 Te content comparison between XRD and RBS measurement of vacuum grown $ZnO_{1-x}Te_x$ alloy thin films. 18

3.5 (a)-(c) Structural characterization of the sample with 4.5% of Te . (a) X-section micrograph showing a columnar-like film with 80 nm of thickness. (b) shows in detail a columnar grain (7 nm) taken from an area in the middle of the layer. The diffraction pattern (c) presents a dotted-ring pattern (arrowhead 1 points at the strong (100), (002) and (101) set of planes). (d) HAADF image of the same sample along with the chemical maps of (e) Zn and (f) Te. 19
3.6 (a)-(c) Structural characterization of the sample with 12% of Te. (a) X-section TEM micrograph showing a growth of 40 nm thick film with a polycrystalline-like structure, detailed on (b). Diffraction pattern on (c) confirms the disordered film by showing a ring pattern with faint dots within the rings (arrowhead 2 points at the strong (100), (002) and (101) set of planes). (d) HAADF image along with the chemical maps of (e) Zn and (f) Te within the 12%Te film. 20
3.7 Impact of substrate temperature effect on absorption coefficient and film Te %. . 21
3.8 The impact of substrate temperature effects on $ZnO_{1-x}Te_x$ XRD patterns. . . . 22
3.9 Film Te content with respect to N_2, O_2 or Ar background gas pressure. 22
3.10 Optical absorption α of $ZnO_{1-x}Te_x$ under N_2 , O_2 , and Ar pressure. 24
3.11 Optical absorption with respect to laser fluence. 24
3.12 The impact of laser fluence effects on $ZnO_{1-x}Te_x$ crystallinity. 25
3.13 The impact of laser fluence on film thickness and Te% uniformity. 26
3.14 Laser fluence effect on $ZnO_{1-x}Te_x$ electrical properties. 26
3.15 Film thickness of $ZnO_{1-x}Te_x$ with different substrate-target distances. 27
3.16 Full width half maximum (FWHM) and grain size of $ZnO_{1-x}Te_x$ with different substrate-target distances. 27
3.17 Electrical properties of $ZnO_{1-x}Te_x$ with different substrate-target distances. . . 28

4.1 (a) Optical absorption coefficient α of a polycrystalline ZnO synthesized in this study. (b) α of polycrystalline $ZnO_{1-x}Te_x$, with x = 0 to 0.23. 31
4.2 (a) Illustration of the physical process of X-ray photoelectron spectroscopy (XPS) experiment with the electronic band alignment of sample and XPS detector. (b) Example XPS spectrum of a Au sample, showing three energy regimes in the spectrum: 1) Valence band (VB) regime, 2) core-level regime, and 3) secondary electron cut-off regime. 33
4.3 (Left) The XPS spectra near the carbon 1s peak for both dark, and laser illumination conditions for $ZnO_{0.854}Te_{0.146}$. (Right) The band bending energy determined by the shifts of the carbon 1s peaks for 6 $ZnO_{1-x}Te_x$ samples ranging from x = 0.006 to 0.32. 34
4.4 Cumulative distributed Gaussian function fitting of XPS spectrum in VB energy regime for six selected samples for Te = 0.6% to 32%. 35
4.5 The Energy of valence band maximum (VBM) positions determined from the Gaussian fit and the E_F with respect to vacuum level. 35

4.6 (a) Illustration of physical process during an X-ray absorption and emission experiment within the electronic band structure of a material. (b) An example $Soft$ X-ray absorption spectroscopy (XAS) / $Soft$ X-ray emission spectroscopy (XES) spectrum of Mn Nitrido [9] plotted on the same energy scale. 37
4.7 XES and XAS spectra for $ZnO_{1-x}Te_x$ samples with x = 0 to 32 %. 38
4.8 A zoomed view of XES/XAS spectra showing a monotonic right shift of VBM with respect to film Te content. 38
4.9 Calculated electronic band structure of $ZnO_{1-x}Te_x$ with the BAC model at x = 0, 0.25, 0.5, 0.75, 1. 40
4.10 BAC calculated electronic band structure of ($ZnO_{0.77}Te_{0.23}$), and calculated optical absorption for each of the eight transitions discussed in 4.4. 42
4.11 (a) Fitting α calculated from BAC to measured optical absorption spectra. (b) E_{gap} values determined from α fitting. 42
4.12 Comparison of VBM and Energy of conduction band minimum (CBM) predicted by BAC model and experimentally determined values from XPS, and XES\XAS. 43
4.13 Comparison of E_{gap} predicted by BAC model and experimentally determined E_{gap} from optical absorption α, XPS, and XES\XAS. 44

5.1 (a) The grain size of the selected samples are around 20 nm. (b) Both of the electron concentration and mobility decrease with increasing Te content. (c) The variation of the electron mobility with respect to electron concentration. (d) Resistivity has increased over three orders of magnitude with increasing Te content from 0.6 % to 13.4 %. 46
5.2 Calculated dependence between electron concentration and mobility at different carrier compensation ratios, and different Te %. 47
5.3 (a) $ZnO_{1-x}Te_x$ electron concentration and (b) mobility variation with respect to N_2 background pressure applied. 48
5.4 Electron concentration of $ZnO_{1-x}Te_x$ and ZnO under Ar and N_2 background pressure. 49
5.5 Seebeck coefficient for nitrogen doped and undoped $ZnO_{1-x}Te_x$, ZnO with respect to electron concentration. 50

6.1 Molecular beam epitaxy (MBE) system schematic with Ga, Sb, N-plasma source. 53
6.2 Film Sb content with respect to substrate temperature. 54
6.3 Film Sb % and III-V ratio under different Ga flux growth regime [128]. 55
6.4 XRD patterns for $GaN_{1-x}Sb_x$ films under different Ga flux growth regime [128]. 55
6.5 Transmission electron microscopy (TEM) and Selected area diffraction (SAD) patterns for pure GaN, and film with 9.4% Sb. 56
6.6 (Left) XES and XAS spectra of $GaN_{1-x}Sb_x$, for Sb = 0 to 10%. (Right) Zoomed-in spectra illustrating the Conduction band (CB) , VB position change with respect to Sb content. 57
6.7 Optical absorption of $GaN_{1-x}Sb_x$ with Sb = 0 to 42 %. 58

6.8 (a). Calculated dispersion relation of $GaN_{1-x}Sb_x$ at Sb = 18%. (b). Calculated Joint-density-of-states (JDOS) of all possible optical couplings for Sb = 18%, and the total absorption coefficient is shown as the black dashed-line. 59
6.9 The fitting of the measured optical absorption spectra α of $GaN_{1-x}Sb_x$ with respect to the BAC calculation (black dashed-line). 59
6.10 (a) CBM, VBM and (b) E_{gap} of the $GaN_{1-x}Sb_x$ alloy across the whole composition range. 61

7.1 (Left) Seebeck coefficient and (right) electrical conductivity of as-grown $GaN_{1-x}Sb_x$ thin films for x = 0.02 to 0.56. 63
7.2 Electrical properties of $GaN_{1-x}Sb_x$ with increasing RTA temeperature: (a) Seebeck coefficient, (b) conductivity, (c) hole concentration, and (d) hole mobility. . 64
7.3 The XRD diffraction patterns for as-grown, RTA 500 °C, and RTA 650 °C for $GaN_{1-x}Sb_x$ samples with Sb = (a) 18% (b) 27% (c) 30% (d) 42% (e) 56%. . . . 65
7.4 Electrical properties comparison of $GaN_{1-x}Sb_x$ with respect to Sb% between as-grown and RTA 650°C series: (a) Seebeck coefficient, (b) conductivity, (c) hole concentration, and (d) hole mobility. 66
7.5 Band structure of $GaN_{1-x}Sb_x$ alloys in (a) Sb-rich, and (b) N-rich composition regimes. 68
7.6 Perturbed Density of states (DOS) for both CB and VB of $GaN_{1-x}Sb_x$ alloys with x = 0, 0.05, and 0.3. 69
7.7 Carrier concentration of $GaN_{1-x}Sb_x$ with Sb = 0%, 5%, 30%, and 50% with respect to E_F position at T = 300 °C (solid line), and 600 °C (dash line). 70
7.8 The electron and hole concentration calculated at $E_F = E_{FS}$ at x = 0, 0.15, 0.3, 0,5, and 0.9 for 300 °C and 600 °C. 71
7.9 The hole concentration measured by Hall effect, and the calculated hole concentration at $E_F = E_V^+$, $E_V^+ + 50$meV, and $E_V^+ + 100$ meV at different Sb composition. 71
7.10 Comparison of Seebeck coefficient between BAC model calculation and experimental data for $GaN_{0.44}Sb_{0.56}$ with respect to hole concentration. 72
7.11 Calculated DOS and Seebeck Coefficient of $GaN_{1-x}Sb_x$ with Sb = 3%. 73
7.12 Band diagram of contact barrier of (a) a typical P-type GaN, (b) using P-type $GaN_{1-x}Sb_x$ as a buffer layer to reduce the potential barrier height and width to provide a better ohmic contact to P-type GaN. 74

8.1 Atomic arrangement of Wurtzite AlN on Si (111) [20]. 78
8.2 History of GaN-on-Si development from 1991 to 2014 for material growth, radio frequency transistors, and power transistors [74] 79
8.3 The electronic band alignment between $ZnO_{0.77}Te_{0.23}$, $GaN_{0.93}Sb_{0.07}$, and Si, with E_F shown as the black dash line. 80
8.4 The electronic band bending between $ZnO_{0.77}Te_{0.23}$ / $GaN_{0.93}Sb_{0.07}$ top cell and Si bottom cell with aligned E_{gap} in equilibrium (top figure), and under solar illumination (bottom figure). 81

8.5 Device architecture of proposed $GaN_{0.93}Sb_{0.07}$-$ZnO_{0.77}Te_{0.23}$ on Si double junction solar cell. 82

A.1 Schematic illustration of the physical processes during a ion beam backscattering process. 87
A.2 The RBS spectra for a $ZnO_{1-x}Te_x$ thin film sample with 12% Te and 239 nm thickness. 87

B.1 The experimental setup, and sample spectra for the nitrogen detection experiment. 89
B.2 The Te and N % in both unoped, and nitrogen doped $ZnO_{1-x}Te_x$ thin films with respect to PLD laser energy. 90
B.3 The NRA spectra of a $ZnO_{1-x}Te_x$ sample with 1.4% Te and with 3% total nitrogen. 90

C.1 The full XPS spectrum of a $ZnO_{1-x}Te_x$ sample with x = 0.006. The shaded regions are the characteristic spectra for the specific electronic state of the elements in the sample: Te 3d, Zn 2p, O 1s, C 1s, and valence band. 91

D.1 Resistivity of $GaN_0.44Sb0.56$ with respect to (a) $\frac{1}{T}$ (b) $\frac{1}{T^4}$. 93

E.1 The temperature variable resistivity of pure ZnO, and $ZnO_{0.92}Te_{0.08}$ thin film samples synthesized in this study. 94
E.2 The temperature variable (left). electron mobility and (right). electron concentration of pure ZnO, and $ZnO_{0.92}Te_{0.08}$ thin film samples synthesized in this study. 95
E.3 The fitting of temperature variable electron mobility of ZnO with grain boundary scattering model [29]. 95
E.4 The fitting of temperature variable electron concentration with the electron activation model. 96

F.1 The atomic force microscopy phase scan images for six $ZnO_{1-x}Te_x$ samples grown on Si substrate, which x = 0.016, 0.06, 0.096, 0.146, 0.236, and 0.316. 98

G.1 The photoluminescence spectroscopy of $ZnO_{1-x}Te_x$ with x = 0.04, 0.086, and 0.134. (Left) Raw spectra; (Right) Normalized spectra. 99

H.1 The schematic of home-built Seebeck coefficient measurement setup in B2 Lawrence Berkeley National Laboratory (LBNL) lab 237. 100
H.2 Photographs taken for the Seebeck coefficient measurement setup. 101
H.3 Sample data for a single Seebeck Coefficient measurement. 101

List of Tables

3.1 The base growth condition for $ZnO_{1-x}Te_x$ alloys. 14
3.2 Summary of general effect of each PLD growth parameter. 15
3.3 List of samples discussed in this chapter. 16

Abbreviations

ADM Amphoteric defect model. 45

ALS Advanced Light Source. 36, 56

ARL U.S. Army Research Laboratory. 53

BAC Band anticrossing. iii, v, vi, 8, 9, 29, 36, 39–44, 57–60, 62, 63, 68, 69, 72, 75, 77

CB Conduction band. v, vi, 8, 9, 30, 36, 39, 50, 57, 58, 67, 69, 70, 74, 77, 78

CBAC Conduction band anticrossing. 8, 43, 57, 58, 68

CBM Energy of conduction band minimum. v, vi, 29, 36, 39, 40, 43, 45, 50, 58, 61, 62

CMOS Complementary metal oxide semiconductor. 5

CPA Coherent potential approximation. 67

CVD Chemical vapor deposition. 11, 83

DOS Density of states. vi, 36, 50, 67–70, 73, 75

EDX Energy-dispersive x-ray spectroscopy. 14, 17

FWHM Full width half maximum. iv, 21, 22, 24, 25, 27, 45

HAADF High-angle annular dark-field. 14, 17

HMA Highly mismatched alloy. iii, 6, 8–10, 20, 23, 29, 36, 57, 67, 68, 75, 83

JDOS Joint-density-of-states. vi, 41, 59

LBNL Lawrence Berkeley National Laboratory. vii, 13, 36, 56, 100

LED Light emitting diode. 5, 52, 73, 75, 77, 83

MBE Molecular beam epitaxy. v, 11, 52, 53, 60, 83, 84

MOCVD Metal organic chemical vapor phase deposition. 52, 74

NRA Nulear Reaction Analysis. 88

OMVPE Organometallic vapor-phase epitaxy. 11

PL Photoluminescence. 5

PLD Pulsed laser deposition. iii, vii, viii, 10–15, 17, 20, 23, 24, 27, 52, 83–85, 88, 90, 97

PV Photovoltaic. 2, 10, 73, 83, 85

PVD Physical vapor deposition. 12

RBS Rutherford backscattering spectroscopy. iii, vii, 13, 15, 17, 18, 21, 60, 86–88

SAD Selected area diffraction. v, 14, 17, 54, 56

SQ Shockley-Quessier. iii, 2, 3

TCO Transparent Conductive Oxide. 4, 5

TEM Transmission electron microscopy. v, 14, 16, 17, 54, 56, 77

VB Valence band. iv–vi, 8–10, 30, 32, 33, 35, 36, 39, 43, 48, 57, 58, 69, 70, 74, 75, 78, 91

VBAC Valence band anticrossing. 8, 36, 41, 43, 58, 68, 69, 84

VBM Energy of valence band maximum. iv–vi, 9, 29, 32, 34–36, 38–40, 43–45, 58, 61, 62, 64

VCA Virtual crystal approximation. iii, 6, 8, 9, 39

XAS *Soft* X-ray absorption spectroscopy. v, 34, 36–38, 43, 44, 56–58, 60

XES *Soft* X-ray emission spectroscopy. v, 34, 36–38, 43, 44, 56–58, 60

XPS X-ray photoelectron spectroscopy. iv, v, vii, 31–36, 43, 44, 91

XRD X-ray diffraction. iii–vi, 14–18, 21–24, 45, 54–56, 60, 63, 65, 76, 77

Nomenclature

E_F Fermi level. iv, vi, 32, 34, 35, 45, 70, 71, 73–75, 77, 79, 80, 84, 91

E_{FS} Fermi stabilization energy. vi, 32, 70, 71, 74

E_{gap} Band gap energy. iii, v, vi, 2–5, 23, 30, 36, 41–44, 52, 57, 58, 60–63, 75–77, 79, 81, 83, 84

Acknowledgments

I am grateful to the many people who contributed to this work. This research was carried out under the supervision of Prof. Samuel S. Mao, and Prof. Ralph Greif, without their guidance, warm encouragement, and continuous support, this work would not be possible.

It has been a great privilege and pleasure for me to work with Dr. Wladek Walukiewicz. His profound knowledge and insightful thoughts in semiconductor physics have been a crucial resource for many of my research discoveries. Also, I am incredibly fortunate to have the chance to work with Prof. Kin Man Yu, his passion in science, rigorous work ethic, and profound knowledge in experimental physics has set-up a role model not only for my career, but also for my personal development.

I would like to thank Prof. Chris Dames, Prof. Oscar Dubon for having served on my Qualifying Examination committee, and for their recent help with this dissertation. Along the way of my study, they have provided me with important advice, and suggestions.

And this dissertation would not be possible without the collaboration with Prof. Sergei Novikov at Nottingham University, Dr. Wendy Sarney, and Dr. Stefan Svensson at the US Army Research Laboratory. And I am grateful to collaborate with Dr. Roberto dos Reis for Transmission Electron Microscopies.

In addition, I wish to thank all the Clean Energy Engineering Laboratory memebers and Solar Energy Material Research Group members and visiting researchers with whom I have worked, including Dr. Matthew Beres, Maribel Jaquez, Christopher Francis, Dr. Alexander Luce, Dr. Douglas Detert, Natalie Sergercrantz, Yannick Jonas Baumgartner, Dr. Monika Welna, Prof. Wei Zhu, Prof. Weiwei Gao, Prof. Guibin Chen, Dr. Yajie Li, Dr. Yifan Ye, Dr. Jinghua Guo, Prof. Shaohua Shen, Dr. Karen Bustillo, Dr. Lothar Reichertz, Dr. Andre Anders, Prof. Joel Ager, Xiaojie Xu, Dr. Eric Garcia, Dr. Tony Ho.

I am thankful to all of my friends and my family. Most importantly, I thank my parents who provided me the opportunity for receiving this advanced education. Their unconditional support and encouragement are priceless.

Chapter 1

Introduction

In order to sustain continuous population and economy growth, it is essential that clean energy plays a dominant role in current and future energy consumption. According to the triple "E" trilemma [38] (Economy, Energy, and Environment), as economies grow, they require more energy. Given today's major energy generation is coming from burning coal, oil, and gas, it inevitably causes damage to the environment, which in turn imposes an economic cost, and slows down economic growth. To break the trilemma, clean energy sources are necessary.

Solar energy is one of the most promising clean energy sources, because it is ubiquitous and abundant. In 2015, the amount of solar energy reaching the earth is larger than three

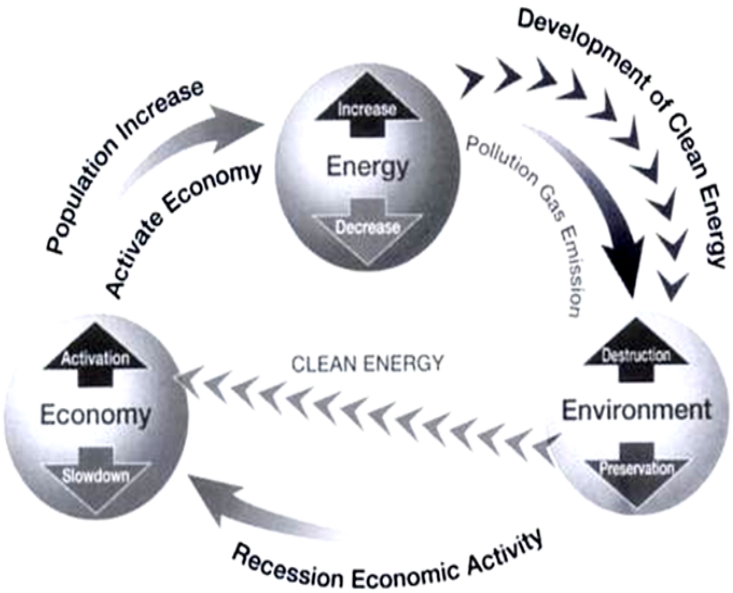

Figure 1.1: 3-E trilemma, the most important task assigned to 21st century civilization. The key way to solve this trilemma is developing clean energy technologies. [38].

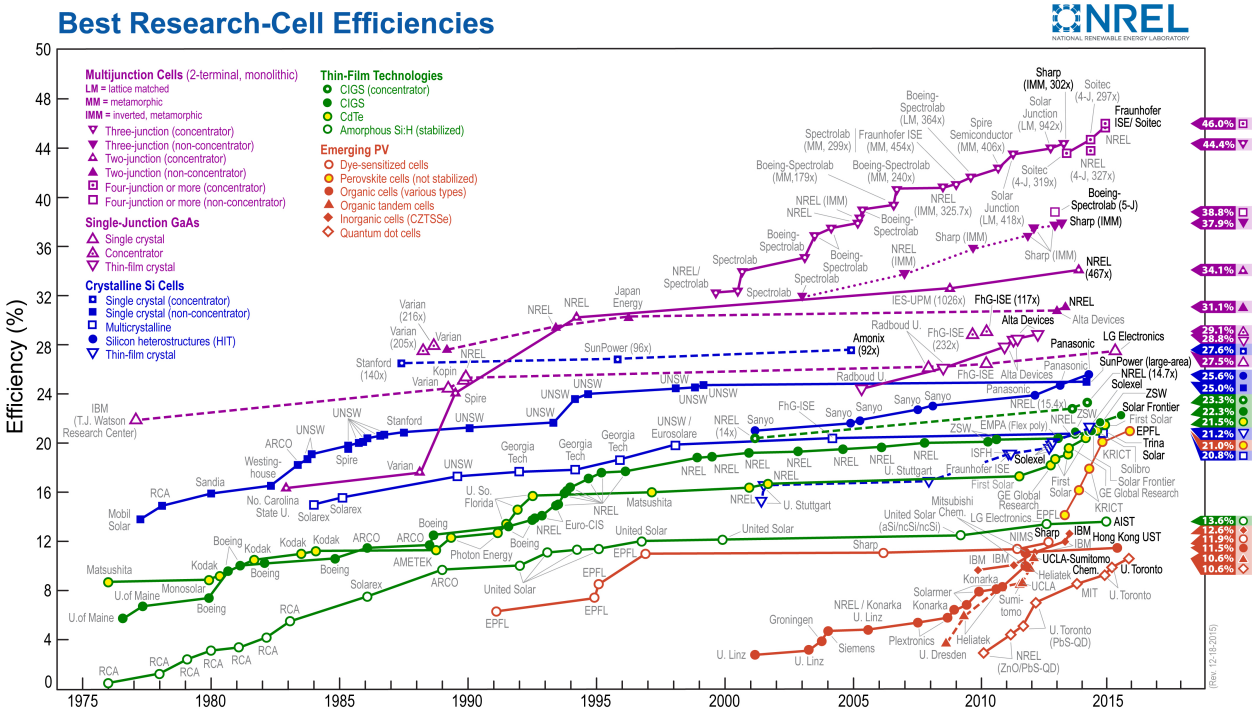

Figure 1.2: The National Renewable Energy Laboratory (NREL) maintains a plot of compiled values of highest confirmed conversion efficiencies for research cells, from 1976 to the present, for a range of photovoltaic technologies.

thousand times the current global energy demand. To put that into perspective, with conventional 20% efficient solar modules, less than 3 % of the U.S. land is needed to power the entire country.

In recent years, increasing efforts have been devoted to the search for new Photovoltaic (PV) materials and designs of new solar cell structures as the Si-based solar cell technology approaches its theoretical efficiency limit [34].

The theoretical maximum efficiency of a single junction solar cell can be calculated using the detailed balance model first introduced by Shockley and Queisser, with the maximum efficiency at a given E_{gap} typically referred to as the SQ limit [93]. Crystalline Si (SQ limit of 33.7%) single junction cells are the leading PV technology dominating the world's market with more than 90% market share [81]. However, energy conversion efficiency improvement has been limited during the past 20 years. SunPower Corp. led the effort of developing highest efficiency Si single junction solar cell, but the energy conversion efficiency has been stagnant over the past 20 years (24% in 1995, and 25.6% in 2015), as shown in Figure 1.2 (solid blue squares).

Single junction GaAs technology led by Alta Device (spun out from UC Berkley, and Caltech) has reported an excitingly 28.8% efficient cell in 2012, but the space of improvement is still limited to the 30% SQ limit of GaAs (E_{gap} 1.39 eV).

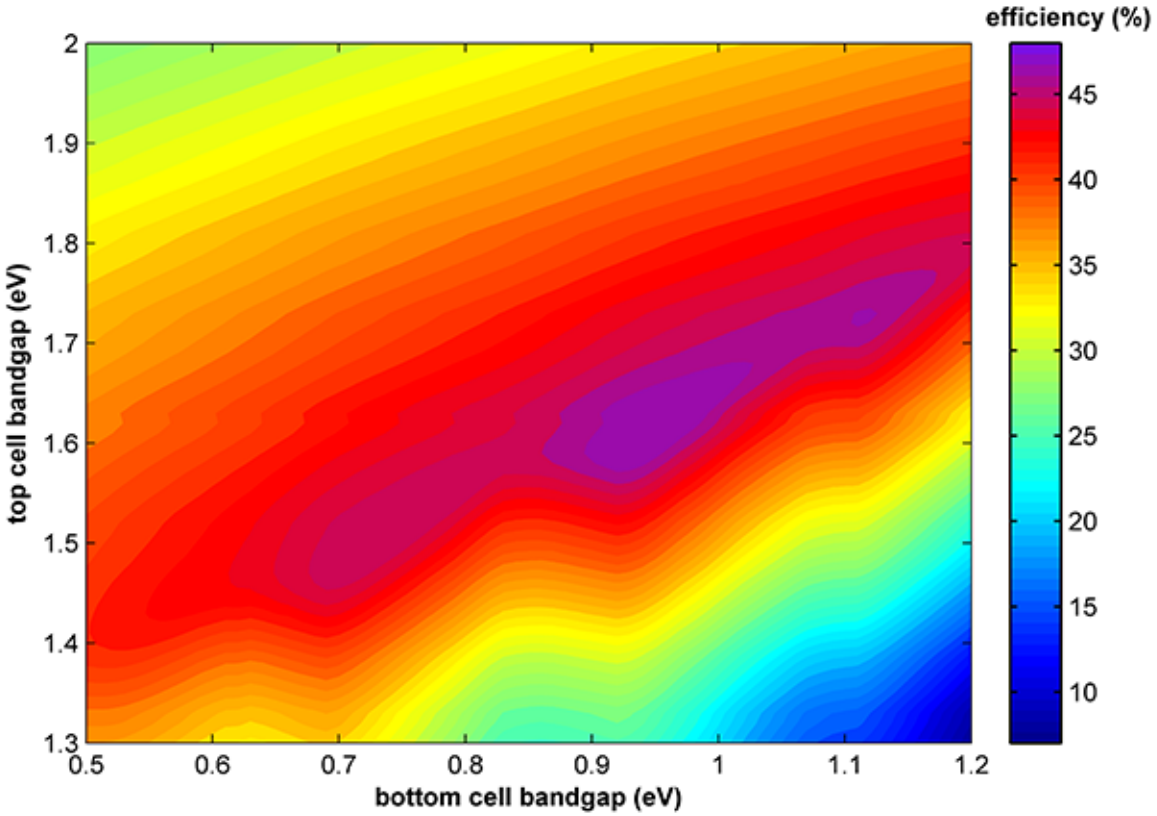

Figure 1.3: The SQ limit efficiency map for a double junction solar cell with respect to the E_{gap} of bottom and upper cells. The black line illustrates the efficiency limit when the bottom cell is Si with E_{gap} of 1.1 eV. [3]

Multi-junction PV technologies has shown higher improvement rate in solar energy conversion efficiency over the same time period from 31% in 2000 to 46% in 2015 (Figure 1.2). Three to four junction cells are today's the most efficient PV technologies. However because of their highly complex fabrication processes, and correspondingly high costs and low yields [124][22], their commercialization is currently only limited to space and military applications [38].

As a result, in recent years, remarkable efforts have been devoted to combine the mature Si PV technologies with new materials to achieve cost effective and highly efficient double junction solar cells.

A double junction solar cell with Si as the bottom cell material, depending on the choice of upper cell materials, can potentially achieve efficiency $> 45\%$. As shown in Figure 1.3, an upper cell material with E_{gap} ranging 1.5 - 1.8 eV can potentially yield solar cells with efficiency of 33 - 45%.

A few attempts have recently been made to combine the Si technology with the other materials to form new PV cell structures. Zhang et al [23] has used two group II-VI (ZnSe

and ZnTe) on both side of Si wafer to form double-heterostructures to replace the top and bottom (Transparent Conductive Oxide (TCO) / doped a-Si:H / undoped a-Si:H) multilayer structures in a heterojunction with intrinsic thin-layer (HIT) solar cell. Both ZnSe and ZnTe have good room temperature illuminescence, good lattice and electronic band alignment with Si. The only drawback is that the E_{gap} of ZnSe and ZnTe are too wide to be a complementary material with Si in absorbing the solar spectrum.

Mcgehee et al has spent the effort on using perovskites (E_{gap} of 1.8 eV) as the upper cell material on Si as a double junction solar cell [8][67], and have achieved promising results of 17% efficiency. Werner et al has fabricated perovskites on Si tandem solar cell with area > 1 cm^2 [117]. Hisashi et al has used a optical splitting system to achieve a 28% efficient perovsite on Si heterojunction solar cell [42]. However, the poor material stability of perovskites is still one of the key obstacle keeping this exciting material away from playing a major role in the PV industry [33].

Therefore, the upper cell material should be a stable material with good lattice match, electronic band alignment with Si, and suitable band gap energy of 1.5 - 1.8 eV. In this work, both ZnO and GaN based materials have been assessed as the potential candidates as the upper cell material.

Chapter 2

Background

2.1 ZnO and GaN material properties

Both ZnO and GaN are attractive semiconductors for optoelectronic applications, due to their earth abundant nature, good environmental stability [125], direct band gap, and strong Photoluminescence (PL). They can both be grown as bulk and have mature industrial synthesis technologies. Al doped ZnO is a commercially used TCO in thin film solar cell technologies such as CdTe and CIGS [98]. Both these materials have strong PL properties, GaN in particular is the dominant material for the white light Light emitting diode (LED) industry, and it has been combined with Si Complementary metal oxide semiconductor (CMOS) technology in many laser diode applications [54].

ZnO and GaN are commonly existing in wurtzite crystalline structure with similar lattice parameter of 3.25 Å[111] and 3.189 Å[52] respectively, and can be grown with high quality on Si (111) substrate [125].

In addition, ZnO in particular has its conduction band well aligned with the valence band of Si as shown in Figure 2.1, which makes a natural tunnel junction between N-type ZnO and P-type Si. However, ZnO has been known to be extremely difficult to achieve P-type conductivity. GaN on the other hand can be doped in both N and P-type in LED, but it does not offer such nice band alignment with Si as ZnO.

Nevertheless, as an upper cell material on Si solar cell, the E_{gap} of both these materials are too wide, at 3.44 eV and 3.51 eV for ZnO and GaN respectively [125].

2.2 Highly mismatched alloys and band anticrossing

Semiconductor alloying is a common method for tailoring material properties such as lattice constants and optical band gaps. The most common semiconductor alloys are composed of elements that are relatively well matched in terms of atom size, ionicity, and electronegativity. The band gap of these well matched semiconductor alloys can be predicted with reasonable accuracy using a linear interpolation of the end point values, known as virtual

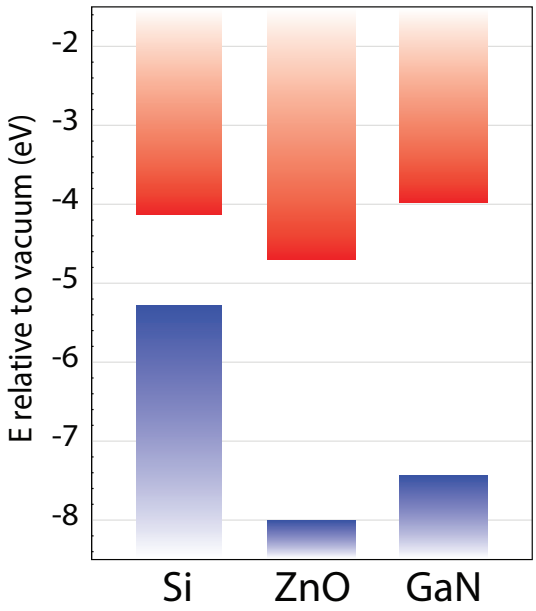

Figure 2.1: An illustration of electronic band alignment between Si, ZnO, and GaN.

crystal approximation (VCA) [79], or modified with a quadratic bowing parameter term [87][99] for less-well matched semiconductor alloys. Another class of semiconductor called highly-mismatched alloy (HMA), contain elements with large difference in atom size and electronegativity, are not well described by the VCA nor bowing parameter modified models.

Over the last decade, it has been well established in semiconductor science the formation of HMAs through isoelectronic substitution of anions with very different ion size and/or electronegativity can result in dramatic restructuring of the electronic bands. Prominent examples include group III-V alloys GaNAs [114], GaInNAs [92][106], and group II-VI alloys ZnTeS [123], ZnTeSe, [123], ZnTeO [130], and ZnOSe [70].

At small alloy composition, a ternary HMA acts as a binary compound semiconductor with a small amount of impurities, similar to the doping mechanism in semiconductors. Traditional dopants in semiconductors are typically shallow or deep level dopants, both of which have wave functions that interact with the periodic potential of the host lattice [72]. Shallow level dopants have single wave functions highly correlated with the host wave functions, thus the energy level of the dopant is determined primarily by the host according to the hydrogenic model [121][72][1].

As a rule of thumb, the ground state shallow levels are within 10s meV from the host band edges. Conversely, the deep level dopants have wave functions highly delocalized in $\mathbf{k}$ space and do not follow the host bands. In small amount, these deep levels remain independent of the host bands and exists as traps within the band gaps of the host semiconductors [121][1].

In large concentrations, impurity resonant energies overlap states in the band, and can interact strongly with the nearby host band. These impurities can be highly mismatched

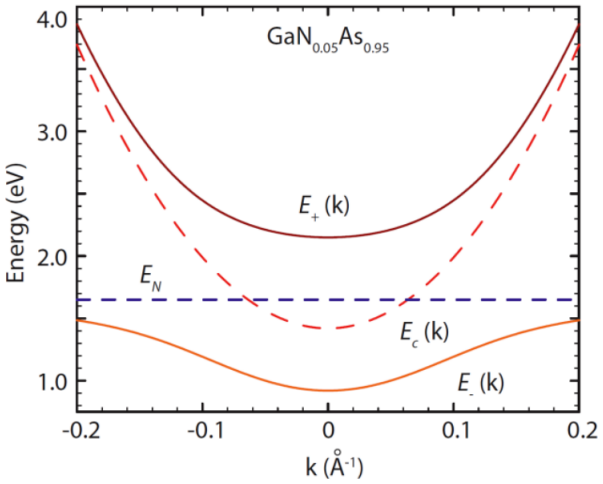

Figure 2.2: Conduction sub-band dispersion relations as predicted by the BAC model [120].

isovalent impurities or deep level dopants [68]. In the simplest case an impurity acts as perturbation to the host material, with the impurity level interacting with the conduction band. This case can be treated as a BAC interaction between the two initial states, the localized impurity state and the highly delocalized host band state[92].

The Hamiltonian for such a system can be expressed as [92]:

$$\begin{vmatrix} E_k^c - E(k) & C\sqrt{x} \\ C\sqrt{x} & E^d + i\Gamma_d - E(k) \end{vmatrix} = 0 \tag{2.1}$$

where C is an empirically determined coupling parameter, and x is the impurity concentration, $C\sqrt{x}$ determines the strength of the perturbation potential brought by the impurities. Γ_d is a broadening parameter, $E(k)$ is the dispersion relation of the band and E^d is the impurity energy level. The result of this mixing is a splitting into two subbands given by:

$$E_{\pm}(k) = \frac{1}{2}\left[(E_N + E(k)) \pm \sqrt{(E(k) - E_N)^2 + 4C^2x}\right] \tag{2.2}$$

where, in this conduction band model, $E_+(k)$ is the mostly delocalized conduction-band-derived state and $E_-(k)$ is the mostly localized impurity-band-derived state. The model has been successfully used to analyze the interaction of the localized isovalent impurity states with the conduction band [114][118]. The bands predicted by the BAC model are shown in Figure 2.2 for a highly mismatched alloy of $GaN_{0.05}As_{0.95}$.

However, the problem becomes more complex when the impurity level lies near the valence band. Here, a complete description of the final states requires that the 3 valence band states (heavy hole, light hole and spin-orbit split off band) mix with the p-like states of the impurity state resulting in a 12×12 Hamiltonian matrix. This system has been theoretically treated in detail for both highly mismatched alloys ZnOSe, and GaMnAs by Marie et al [70][68].

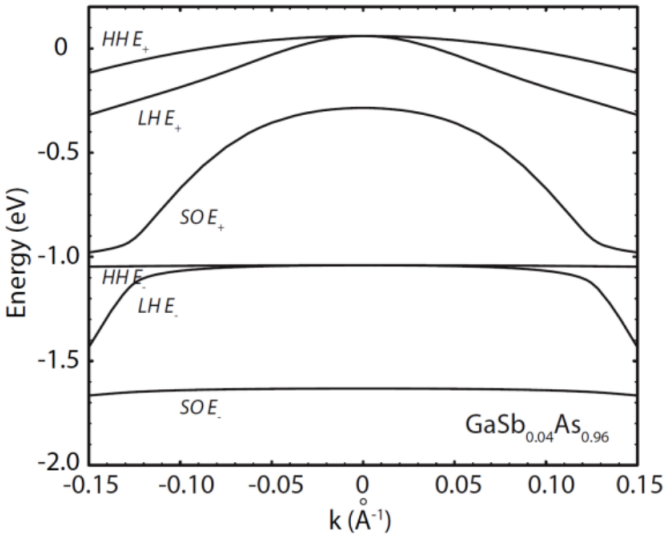

Figure 2.3: Valence sub-band dispersion relations of $GaSb_{0.04}As_{0.96}$ [2].

Valence band anticrossing (VBAC) occurs in systems where the substitutional atom is much less electronegative than the matrix atom. This is the case for GaNAs and GaAsSb [1]. The calculated valence band structure is shown in Figure 2.3 [2]. It has been shown that this structure can also be approximated by using a 2×2 Hamiltonian or a single impurity and a single valence band [68][71].

The BAC model matches well the description of electron restructuring for dilute alloy composition range ($x < 0.1$), but the dilute impurity states (with non-interacting wave functions) do not necessarily apply to midrange alloy compositions. In 2009, a theoretical interpolation of HMA systems across the whole composition range by VCA was used to model the band gap across the entire composition range. Experimentally determined band gaps of GaNAs across the whole composition range shows surprisingly good agreement with the BAC model as shown in Figure 2.4, despite the assumption of the dilute impurities. This system demonstrates that midrange HMA compositions can be achieved, opening up a new range of band gaps in nearly any alloy system.

Finally, it is important to mention that HMA materials can feature tunable band structures. If the impurity deep level exists within the gap, rather than within the band, this results in an effectively narrowing of the band gap since the gap between the highest filled and lowest unoccupied states has decreased.

In a VBAC material, the impurity deep level interacts with the host VB to develop into a new fully occupied band above the host VB, and thus allowing for absorption for lower energy photons.

Also, depending on VBAC or Conduction band anticrossing (CBAC), the HMA allows the flexibility to tune the CB or VB of the host material independently. This feature allows the reduction of the band gap in both ZnO and GaN by moving the valence band upward

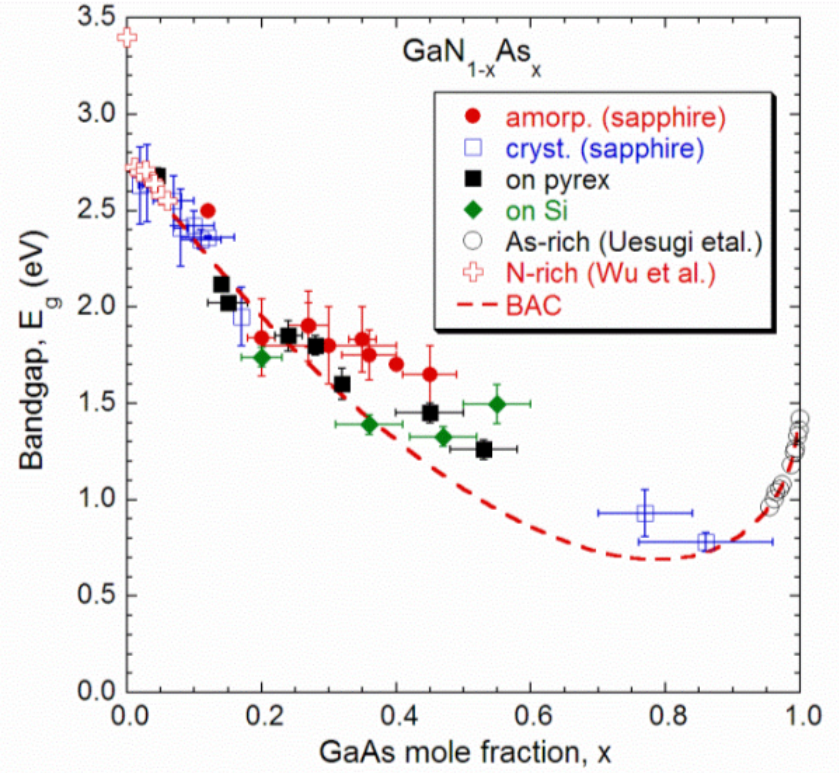

Figure 2.4: Dependence of the optical band gap energy on the value of x for crystalline and amorphous $GaN_{1-x}Asx$. Calculated composition dependence of the band gap of $GaN_{1-x}Asx$ alloys based on the BAC and VCA. [129]

only while maintaining well-aligned CBs with Si.

In well-studied HMA systems, impurity deep levels exist further into the band gap (i.e. further away from the host band edge) with increasing electronegativity difference between the host anion and the introduced isovalence anion [120]. In N-rich GaNAs, As exists at 0.7 eV above the GaN VBM, and Se exists at 0.9 eV above the ZnO VBM in O-rich ZnO. And it is found that Sb exists at 0.9 eV below GaAs VBM [2], and Te deep level exists at 0.9 eV above ZnS VBM [131][75], and 0.2 eV above ZnSe VBM [122][113]. Thus, Sb deep level is expected to be 1.2 eV above GaN VBM, and Te deep level is expected to be 1.5 eV above ZnO VBM as illustrated in Figure 2.5. Therefore alloying Te in ZnO, and Sb in GaN cpi;d potentially reduce the band gap of these two materials to 1.5 - 1.8 eV range by modifying the host VB only.

2.3 This dissertation

There are eight chapters in this dissertation. The first is an introduction, in which, I discussed the importance of clean energy generation in a historical scope, the direction of next

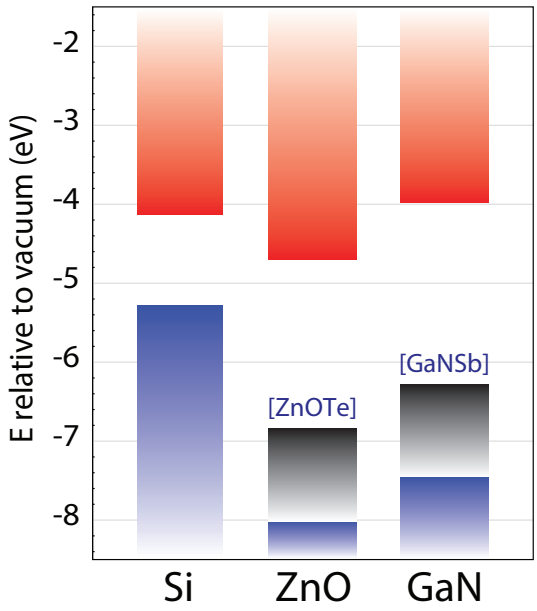

Figure 2.5: An illustration of expected electronic band structure of HMA ZnOTe, and GaNSb.

generation of solar PV technology development. Chapter 2 is a background discussion of the semiconductor electronic band structure engineering through alloying. Also, this chapter introduces a special family of alloy systems namely HMA and its theory. The HMA is the intended material design approach used in this work.

Chapter 3 - 5 are discussions specifically on $ZnO_{1-x}Te_x$. Chapter 3 describes the growth method (PLD), and the effect of growth parameters on the structural and optical properties. Chapter 4 discusses the electronic band structure characterization. Chapter 5 discusses about the electrical properties and P-type doping effect.

Chapter 6 - 7 are discussions on $GaN_{1-x}Sb_x$. Chapter 6 describes its synthesis process (LT-MBE), and its thin film structural, optical, and electronic properties. Chapter 7 discusses about the electrical properties, and the hole transport modeling in the Sb-derived VB.

Chapter 8 serves as a detailed assessment of the top cell architecture with both of the $ZnO_{1-x}Te_x$ and $GaN_{1-x}Sb_x$ layers. Lastly in chapter 9, the challenges and future work of these material systems are discussed.

Chapter 3

$ZnO_{1-x}Te_x$ highly mismatched alloy synthesis and structural properties

ZnO has been synthesized by a variety of methods, including PLD [110], MBE [30][16], magnetron sputtering [37][31], Chemical vapor deposition (CVD) [100][53], Organometallic vapor-phase epitaxy (OMVPE) [62]; and ZnO can be synthesized in different form factors: bulk, thin films, and different nanostructures. Among different synthesis techniques, PLD is one of the techniques that yields the highest-quality thin film ZnO [110], and it is the synthesis tool used in this study. There are very limited reports on the synthesis of ZnOTe in literature, and this is the first systematic study of the synthesis and material properties of this alloy system [101].

This chapter presents the growth of $ZnO_{1-x}Te_x$ thin film by PLD on glass substrate. section 3.1 provides an overview of the experimental technique and outlines the basic physical mechanisms of laser material interaction, and provides the specific growth parameters and details of the experimental setup applied in this study. Section 3.2 introduces the characterization techniques used in this chapter, and Section 3.3 discusses the growth effects on the structural and chemical properties of the $ZnO_{1-x}Te_x$ alloys with x ranging between 0 and 0.23.

3.1 Pulsed laser deposition of $ZnO_{1-x}Te_x$

ZnO is a Wurtzite crystal, where the ionic radius of Zn is 131 pm [65], and O is 66 pm. The Wurtzite crystal structure describes a two element compound isomorphous to a hexagonal close packed structure where half of the tetrahedral holes are occupied. The space for an interstitial atom is 0.225 times ionic radius of the larger species [39]. The ionic radius for Te is 136 pm, which is twice as large as oxygen's ionic radius, and more than four times the interstitial space, therefore thermodynamically it is unfavorable for Te atom to be incorporated in the thin film. However, as shown in the following sections, ZnOTe thin film can be experimentally grown under low temperature, with non-equilibrium growth conditions.

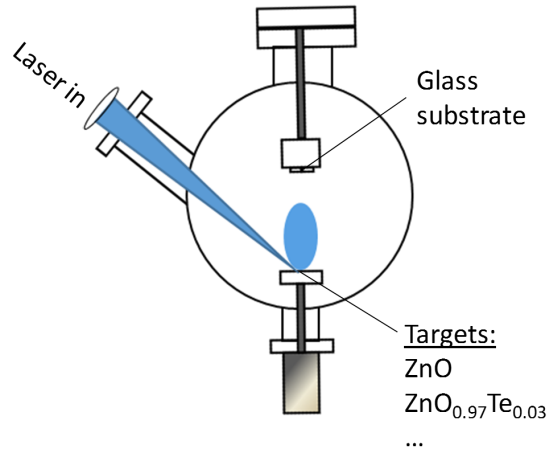

(a) A schematic illustration of a PLD system.

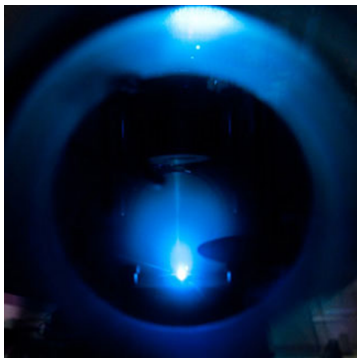

(b) A picture showing the laser ablation plume during the deposition of ZnO.

Figure 3.1: Schematic of a PLD and ZnO laser ablation plume.

The pulsed laser deposition is one of many thin film Physical vapor deposition (PVD) techniques. The detailed mechanisms of PLD include three major processes: 1). the ablation process of the target material by the laser irradiation; 2). the development of a plasma plume with high energetic ions and electrons; 3). and the nucleation and growth of the film on the heated substrate surface.

In a typical PLD system there is a high-power pulsed laser beam which is focused inside a vacuum chamber to strike a target of the material that is to be deposited (Figure 3.1a). This material is vaporized from the target in the form of a plasma "plume" (Figure 3.1b) which is then deposited as a thin film on a substrate. This process can occur in ultra high vacuum or in the presence of a background gas, such as oxygen which is commonly used when depositing oxides. Although the PLD setup is relatively simple compared to other deposition techniques, the physical phenomena of laser-solid interaction is complex.

The laser ablation process is non-equilibrium for nanosecond to femtosecond pulsed laser as the photon absorption is a much faster process than the heat diffusion in a semiconductor. When a laser photon interacts with matter, the photon energy is coupled to the lattice through electronic processes. In semiconductors the photon is absorbed via electron excitation from valence band to conduction band. The excited electrons then relax by scattering with the lattice, and generates phonons. Electronic relaxation processes are very fast with a typical lifetime of 10^{-14} to 10^{-13} s [89], however, the phonon relaxation time in semiconductors is usually much longer, i.e. energy absorption is much faster than, energy dissipation via heat diffusion. Hence, the electrons and phonons will never reach energy equilibrium states during the laser pulse. Therefore, inevitably, this process gives rise to vaporization and plasma formation during the time scale of the pulse duration. Such process leads to stoichiometry transfer of target material composition in the laser induced plume.

As discussed above PLD is an obvious choice for a HMA material due to the potential for both stoichiometric transfer of target materials to the substrate and non-equilibrium growth condition [89].

The samples studied in this thesis were grown with the PLD chamber operated by the Electronic Materials Program of the LBNL. The PLD system is assembed by SVT Assocaites, Inc. [cite]. The laser used in the system is a KrF excimer laser (λ = 248 nm) with a 20 ns laser pulse duration. Before the synthesis, the substrate is put in a load lock chamber, which will then pumped down to 10^{-7} torr. After that, the substrate is transferred to the growth chamber which has a base pressure of 10^{-8} torr. The load lock design helps maintain the growth chamber pressure by avoiding frequent opening of the growth chamber. The substrate is heated in the growth temperature to a desired growth temperature, followed by flowing the desired background gas and pressure. During the deposition, the laser is directed by two 45° high quality UV mirrors, then aligned through the focusing lens, a port window, a sacrificial window, and finally strikes the target at a 45° angle. Figure 3.2[A] shows a detailed look of the inside of the chamber. Due to the energy losses at the mirrors, lens, and windows, the laser energy reaching the target is around 73% to 77% of the original setting's energy. The laser intensity is measured with a Molectron Energy Max 400 laser energy meter. The laser fluence values reported in this dissertation are values reported at the laser setting. The reader needs to multiply the reported values by 0.73 to convert to the real fluence reaching the target.

This PLD system offers a wide range of controllable growth parameters. The laser energy can be adjusted in the range of 60 to 700 mJ with 0.06 cm^2 laser spot on the target (as shown in Figure 3.2[B]). The substrate temperature is adjustable to 800 °C. The background gas type can be selected from a range Ar, O_2, N_2, or Ar/O_2 mix or Ar/N_2 mix. The background pressure is adjustable from base pressure 10^{-8} torr to 50 mtorr. The substrate to laser distance is adjustable from 5 to 9 cm. The laser repetition rate is adjustable from 0.25 to 50 Hz.

For the growth of $ZnO_{1-x}Te_x$ alloy, rotated cold-pressed power targets with varying compositions of ZnO and ZnTe were used [101]. The samples discussed in this chapter are grown with seven different targets composed of 0% ZnTe (pure ZnO) upto 27.5% ZnTe (72.5% ZnO). It is worth noting that the surface of the target affects the final composition of the films. Ablation during growth leaves the target surface Te-rich (the surface appears metallic after ablation Figure 3.2), such that the composition of the ablated surface of the target was found to be a few percent Te higher than that of the bulk target material. To keep the film composition controllable, the PLD targets were sanded to remove the surface damage after each growth.

3.2 Characterization techniques used in this chapter

The thickness and Te content of these samples were measured by RBS using a 3 MeV He^{2+} ion beam. RBS only measures the total Te content in the film, not necessarily the

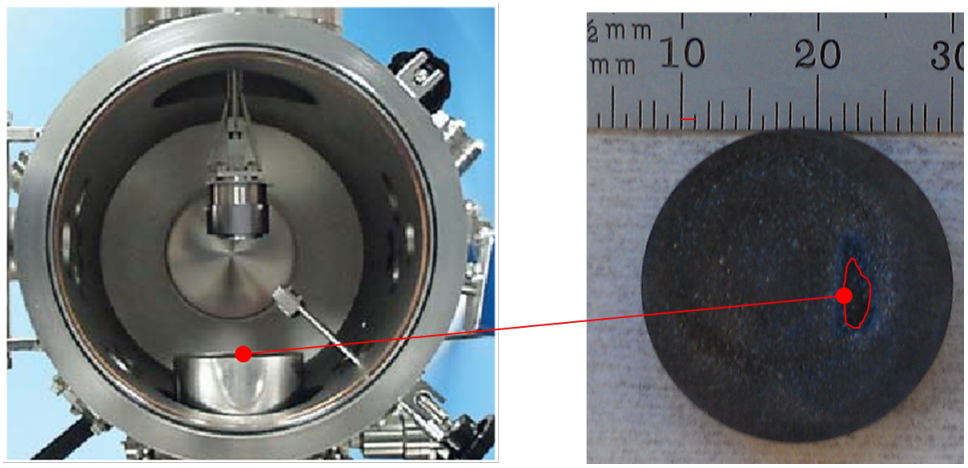

Figure 3.2: PLD growth chamber used in this study. The laser channel is positioned at 45° towards the target. The dimension of the PLD target is shown with the marked laser ablation spot.

Subst. Type	Target, ZnTe [%]	Subst. temp. [°C]	Laser fluence [J/cm²]	Gas type	Pressure [torr]	Distance [cm]
Glass	5.1%	200	3.3	-	base	9

Table 3.1: The base growth condition for $ZnO_{1-x}Te_x$ alloys.

substitutional Te incorporated in the O sublattice. The amount of substitutional Te in the film was deduced from the lattice parameter of the $ZnO_{1-x}Te_x$ films measured by the XRD The measured $ZnO_{1-x}Te_x$ lattice parameter is then linearly interpolated between the lattice parameter of the pure ZnO and the pure ZnTe. The optical absorption coefficient of the $ZnO_{1-x}Te_x$ is deduced from the transmission and reflection measurements performed by a Perkin Elmer Lambda 950 photospectrometer in the wavelength ranging from 250 nm to 2500 nm.

TEM of cross-sectioned samples was used to determine the microstructure and chemical distribution of the atomic species within the grown layer. Electron transparent samples were prepared by mechanical polishing followed by Ar ion milling at liquid nitrogen (LN) temperature. Samples were gently plasma cleaned before being analyzed by a FEI Titan microscope equipped with a Bruker EDS windowless Silicon drift detector (SDD) and High-Angle Annular Dark-Field detectors. Elemental maps using Energy-dispersive x-ray spectroscopy (EDX) were acquired concurrently with High-angle annular dark-field (HAADF) images. SAD patterns were taken with JEOL 3010 microscope using a diffraction aperture with a 200 nm diameter.

Parameter	Variation	Effect on film
Substrate temperature	Increase	Film nucleation and atom motion on the surface. In general as the growth temperature increase, it increases the adatom surface diffusion and film annealing, and increases the crystallinity of the resulting films.
Laser fluence	< Ablation threshold	Thermal evaporation processes dominate. Heat diffusion rate is fast compare to evaporation rate. In general it results in poor film smoothness, and low deposition rates.
	> Ablation threshold	Electronic processes dominate. Direct bond breaking by radiation, high KE plume with high ionic content. Heat diffusion rate is slow compared to evaporation rate. In general it results In high crystallinity, high deposition rates, and high film smoothness
	>> Ablation Threshold	Increases thermal penetration depth, and causes splashing. In general it reduces film smoothness, and negligible for film crystallinity.
Chamber background pressure	Ar/O2/N2 increase	Increases collisions of plume species --> decreases KE of deposition specifies. Introduces flux of background gas particles to the deposition species --> to maintain film stoichiometry. In general it decreases film crystallinity, modifies film stoichiometry, and reduces film smoothness.
Laser pulse rate	Increase	Negligible effect, in general, the time between each laser pulse >> pulse duration (usually in ns to fs).
Distance between target and substrate	Increase	Increases diffuseness of incident plume. Decreases KE of deposition species. In general it increaes film uniformity, and increases film crystallinity
Target composition	Increase	Controls the stoichiometry of the resulting films. In general PLD under base pressure gives stoichiometry transfer of target composition to the substrate.
Substrate material	Increase lattice matching	The crystallography of the substrate will affect whether film is epitaxial. In the case of low lattice mismatch (<2%) between the film and substrate, an epitaxial film can be obtained and the strain can be controlled. Large mismatch can lead to high defect concentrates in epitaxial films.

Table 3.2: Summary of general effect of each PLD growth parameter.

3.3 Effects of growth on the structural and chemical properties

Growth conditions govern the structure and stoichiometry of the final films. The effects of target composition, substrate temperature, laser fluence, background gas type and pressure, and target-substrate distance are examined. The parameter space examined is summarized in Table 3.3, the film characteristics can be further optimized towards specific applications.

Target composition

The ZnTe powder ratio in the PLD target controls the Te alloy composition in the resulting films (S46, S74, S67, S83, S84, S85 in Table 3.3). This set of samples are grown under the base conditions set (Table3.1) with targets of different ZnTe % (atomic %). The Te content in the thin films follow the ZnTe ratio in the targets. Under base pressure ambient, the Te content in the film is always 3% less than that in the PLD targets as illustrated in Figure 3.3. Figure 3.4a shows the (0002) XRD diffraction peaks of $ZnO_{1-x}Te_x$ films with RBS measured Te content ranging from 0 to 6%. The inset presenting the full range of the XRD pattern from a 1.2% Te film shows only a strong (0002) diffraction peak of $ZnO_{1-x}Te_x$. It suggests that the films have a single phase with c-axis preferred orientation. We note that for samples

Name	Target, ZnTe [%]	Subst. temp. [°C]	Laser fluence [J/cm²]	Gas type	Pressure [torr]	Distance [cm]	Te content [%]
S46	0.0%	200	1.9	O2	$15x10^{-3}$	9	0.00%
S74	2.6%	200	1.9	-	base	9	0.34%
S60	5.1%	200	1.9	-	base	9	2.40%
S83	8.6%	200	1.9	-	base	9	4.40%
S84	14.1%	200	1.9	-	base	9	12.00%
S85	27.5%	200	1.9	-	base	9	23.00%
S70	5.1%	120	1.9	-	base	9	4.90%
S67	5.1%	275	1.9	-	base	9	1.80%
S66	5.1%	350	1.9	-	base	9	1.00%
S68	5.1%	425	1.9	-	base	9	0.50%
S86	2.6%	200	1.4	-	base	9	1.60%
S90	2.6%	200	1.9	-	base	9	1.12%
S87	2.6%	200	2.8	-	base	9	1.36%
S88	2.6%	200	4.1	-	base	9	1.20%
S101	5.1%	200	1.9	Ar	$1x10^{-3}$	9	2.80%
S150	5.1%	200	1.9	Ar	$5x10^{-3}$	9	4.40%
S104	5.1%	200	1.9	Ar	$8x10^{-3}$	9	8.00%
S103	5.1%	200	1.9	Ar	$50x10^{-3}$	9	11.00%
S105	5.1%	200	1.9	O_2	$1x10^{-3}$	9	1.60%
S104	5.1%	200	1.9	O_2	$10x10^{-3}$	9	9.40%
S103	5.1%	200	1.9	O_2	$50x10^{-3}$	9	13.00%
S129	5.1%	200	1.9	N_2	$1x10^{-3}$	9	2.90%
S113	5.1%	200	1.9	N_2	$5x10^{-3}$	9	3.40%
S112	5.1%	200	1.9	N_2	$10x10^{-3}$	9	8.00%
S108	2.6%	200	1.9	-	base	8	1.50%
S107	2.6%	200	1.9	-	base	6.5	1.80%

Table 3.3: List of samples discussed in this chapter.

with 12% and 23% of Te the films become polycrystalline with random grain orientation so that the (0002) peak is absent. The monotonic shift of the (0002) peak to lower diffraction angle with increasing Te content suggests that the lattice parameter of the alloy increases with Te content. This increase in lattice parameter is consistent with increasing amount of Te substituting the O sublattice in ZnO. Figure 3.4b shows the dependence of substitutional Te in $ZnO_{1-x}Te_x$ films as estimated by the shift in the XRD peak with the total Te content measured by RBS for samples with less than 6% Te. The linear relationship shown in Figure 3.4b indicates the majority of the Te atoms in the film substitute O in the ZnO lattice. We also point out that such comparison becomes difficult for samples with higher Te content where the (0002) peak is absent due to much smaller grain size and more random grain orientation.

Results of TEM studies on the microstructures of a $ZnO_{1-x}Te_x$ sample with 4.5% of Te are presented in Figures 3.5(a)-(c). Cross-sectional TEM micrograph on Figure 3.5 (a) shows a 80 nm thick film with a columnar-like structure (columns of about 7 nm, see Figure

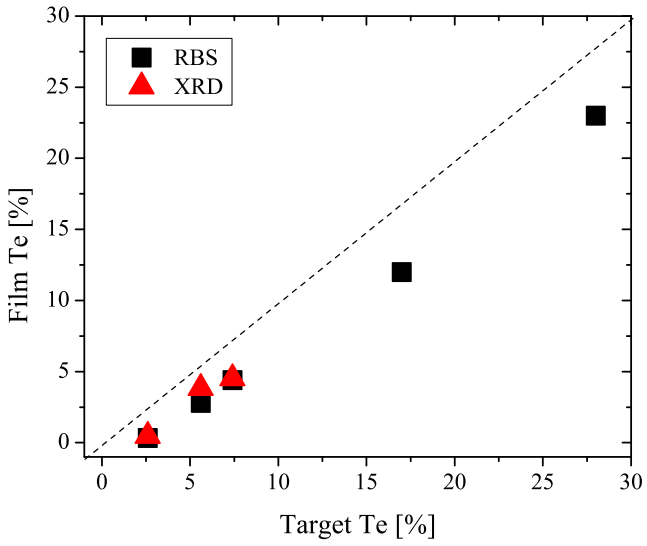

Figure 3.3: The correlation of Te content between the PLD target and the resulting film. Te content measured by RBS and XRD are shown as black squares and red triangles respectively. The dotted diagonal shows 1:1 ratio.

3.5 (b)). A columnar grain growth agrees with the preferred c-axis preferred orientation observed in the XRD. A SAD pattern (Figure 3.5 (c)), taken from the whole layer shows a dotted ring pattern, corroborating a random distribution of these columns. Calculations of lattice parameters using the SAD patterns show agreement with ZnO hexagonal structure. The arrowhead #1 indicates a set of planes (100),(002) and (101) with lattice parameters of 2.821, 2.582 and 2.49 (± 5 %)Å, respectively. A HAADF image of the same sample (4.5% of Te) along with the chemical maps of Zn and Te within the film are presented in Figures 3.5 (d)-(f). The homogeneous distribution of the chemical species shown in Figure 3.5 (c) suggests that the sample is a random alloy of $ZnO_{1-x}Te_x$ with no observable Te clustering. The overall Te content measured by EDX agrees with that obtained by RBS.

Similar structural and compositional analyses were performed on the sample with Te concentration of 12%. Cross-sectional TEM micrograph on Figure 3.6 (a) shows a 40 nm thick film with a polycrystalline-like structure shown in detailed in Figure 3.6 (b). A SAD ring pattern with decreasing number of dots within the rings shown in Figure 3.6 (c) confirms the disordered structure of the film. Measurements of lattice parameters agree with ZnO polycrystalline structure. Experimental values for the set of planes (100), (002) and (101) indicated by the arrowhead #2 are 2.791Å, 2.6075Åand 2.490Å($\pm 5\%$), respectively. Figures 3.6 (d)-(f) present a HAADF image along with the chemical maps of Zn and Te within the 12%Te film. It is important to notice here that, even with this considerably larger amount of Te content, the elemental maps still show a homogeneous distribution of the chemical

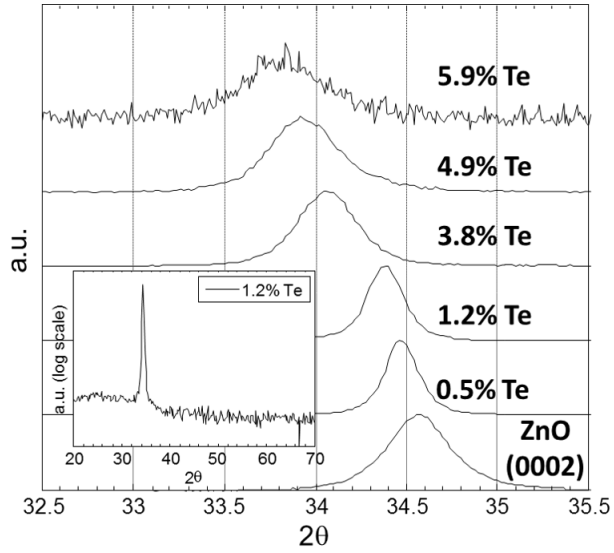

(a) XRD patterns of $ZnO_{1-x}Te_x$ alloys with x ranging from 0 to 0.059. The addition of Te into the ZnO lattice causes a shift of the (0002) diffraction peak to smaller angles, indicating that the Te atom enlarges the d spacing in the ZnO lattice. The lower inset shows a broader range 2 ranging from 20° to 70° , showing that the (0002) peak is the only observable diffraction peak of this alloy.

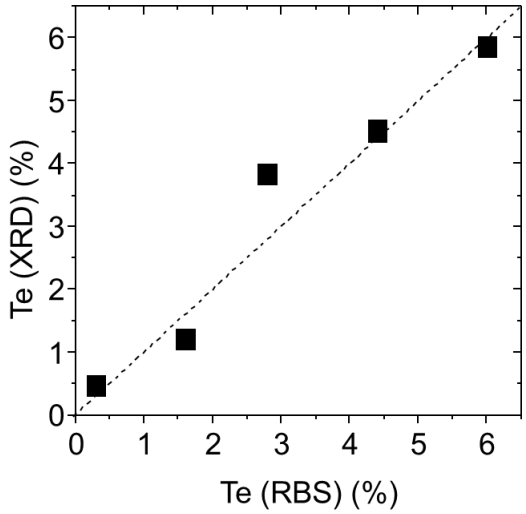

(b) A comparison between the substitutional Te % deduced from XRD and the total Te % measured by RBS for Te < 6%. The proximity of the data points to the diagonal line (100% substitutional Te in ZnO lattice) indicating that the substitutional rate of Te in ZnO lattice is reasonable high.

Figure 3.4: Te content comparison between XRD and RBS measurement of vacuum grown $ZnO_{1-x}Te_x$ alloy thin films.

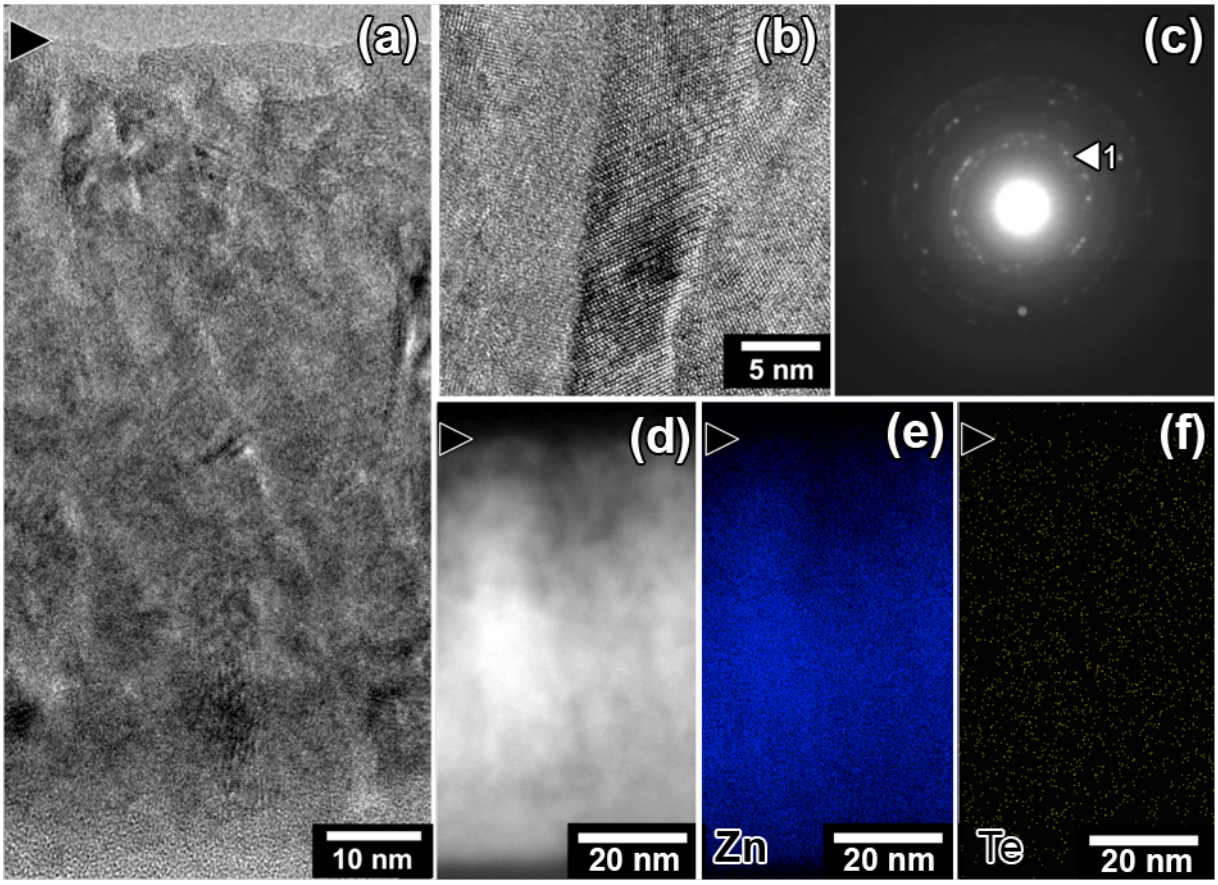

Figure 3.5: (a)-(c) Structural characterization of the sample with 4.5% of Te . (a) X-section micrograph showing a columnar-like film with 80 nm of thickness. (b) shows in detail a columnar grain (7 nm) taken from an area in the middle of the layer. The diffraction pattern (c) presents a dotted-ring pattern (arrowhead 1 points at the strong (100), (002) and (101) set of planes). (d) HAADF image of the same sample along with the chemical maps of (e) Zn and (f) Te.

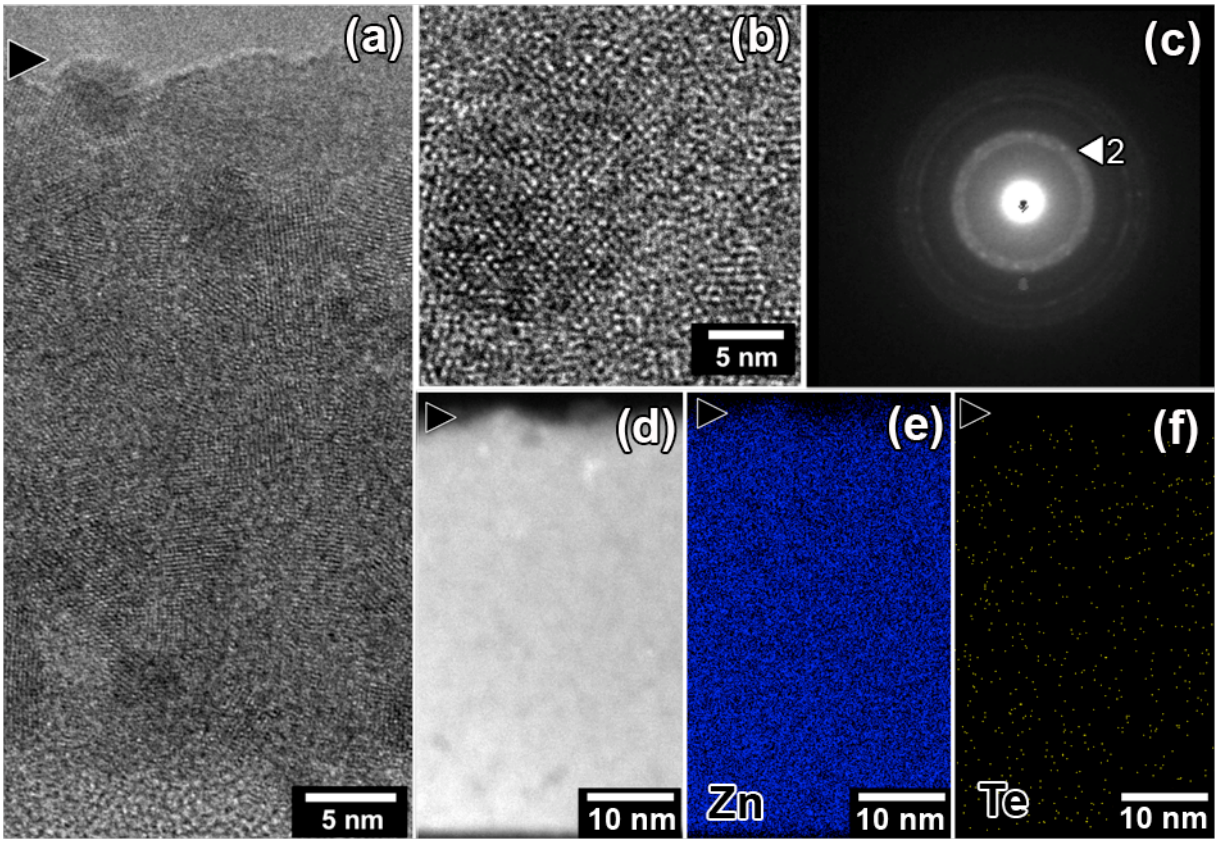

Figure 3.6: (a)-(c) Structural characterization of the sample with 12% of Te. (a) X-section TEM micrograph showing a growth of 40 nm thick film with a polycrystalline-like structure, detailed on (b). Diffraction pattern on (c) confirms the disordered film by showing a ring pattern with faint dots within the rings (arrowhead 2 points at the strong (100), (002) and (101) set of planes). (d) HAADF image along with the chemical maps of (e) Zn and (f) Te within the 12%Te film.

species as observed in the 4.5% Te film.

Substrate temperature

Growth substrate temperature controls majorly the crystallinity, chemistry of the alloy thin films (S70, S67, S66, S68 in Table 3.3). This set of samples are grown with a 5.1% PLD target with temperature varying from 120° to 425° . In HMA due to the mismatch nature, HMAs are immiscible under standard growth conditions, low temperature is usually used to inhibit the atom motion on the surface during the film growth process. For the As-rich GaNAs, the temperature must be lower than 300 ° to incorporate $>$ 17% As in the alloy [129]. Similar behavior is reported in the O-rich ZnOSe [71], Se content increases with decreasing growth temperature.

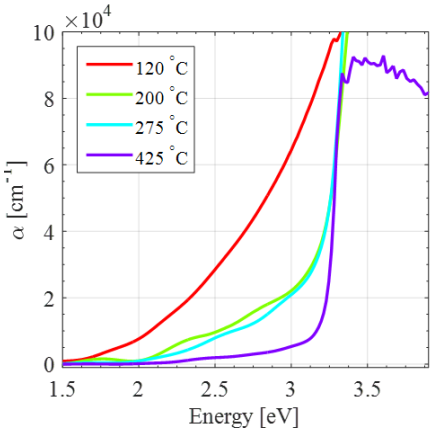

(a) Substrate temperature effect on absorption coefficient

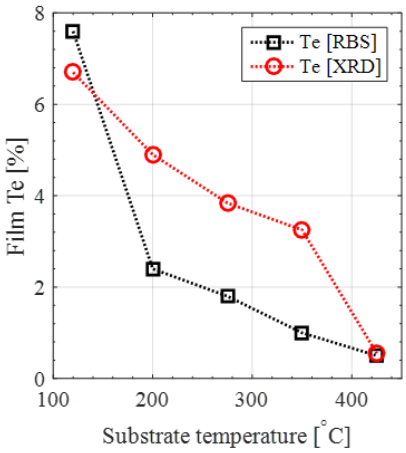

(b) Film Te % (measured by both RBS and XRD).

Figure 3.7: Impact of substrate temperature effect on absorption coefficient and film Te %.

For $ZnO_{1-x}Te_x$, under increasing growth temperature, the $ZnO_{1-x}Te_x$ (0002) XRD diffraction peaks shifts monotonically to larger angles, as shown in Figure 3.8. This implies that the ZnOTe lattice space shrinks, and the incorporation of Te in ZnO lattice decreases under higher growth temperature. The calculated monotonic decrease of Te substitutional rate with increasing growth temperature (Figure 3.7) shows a consistent trend with the RBS measured Te content in the film.

In addition, the FWHM of the samples decreases with increasing growth temperature. The mean ordered crystal grain sizes are calculated with the Scherrer equation [25]. As shown in Figure 3.8, the crystal gain sizes increases with increasing growth temperature, and with decreasing Te content. In general good quality ZnO is grown at a substrate temperature > 500 ° [49][46][51][41][132], higher growth temperature promotes nucleation of the crystal grains. Also, as shown in the previous subsection 3.3 that increasing Te content increases the disorder in the film, and eventually the grains are too small to be measured by XRD.

Background gas type and pressure

Increasing gas pressure increases Te content in the film no matter which type of gas used. Figure 3.9 shows the film Te content with respect to the background pressure of N_2, O_2 or Ar. The film Te content first increased from ∼2% to ∼10% with pressure increase from chamber base pressure to 10 mtorr. However the increase rate slowed down beyond 10 mtorr, and film Te content reached only ∼15% when background pressure reached 50 mtorr.

The effect of Ar background gas can be understood in respect to the gas molecule scattering effect of the depositing species. As an inert gas, Ar is not expected to be involved in the chemistry during the deposition, but only contributes to the scattering effect. There are

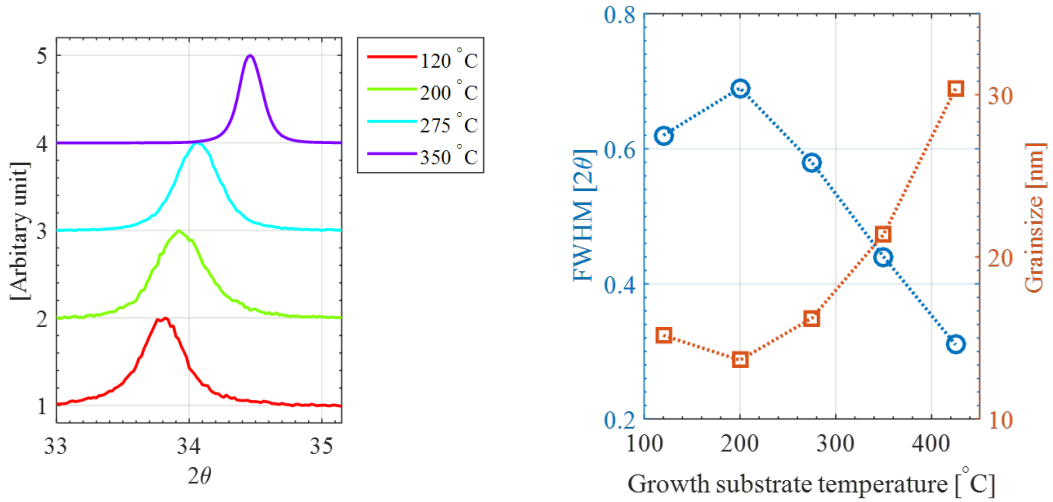

(a) Substrate temperature effects on XRD. (b) Fitted FWHM and grain sizes.

Figure 3.8: The impact of substrate temperature effects on $ZnO_{1-x}Te_x$ XRD patterns.

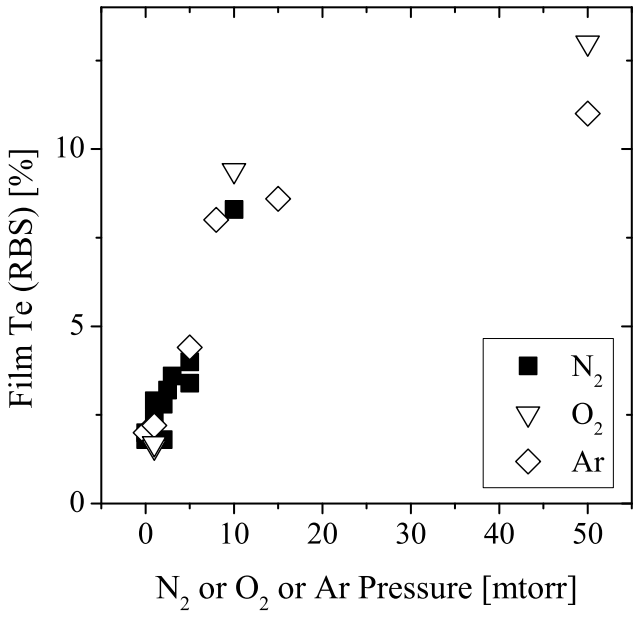

Figure 3.9: Film Te content with respect to N_2, O_2 or Ar background gas pressure.

three elements Zn, O, and Te in the laser induced plasma plume in the form of atom, ions, and molecules. The atomic mass of Te (127.6 **u**) $\gg$ Zn (65.41 **u**) $\gg$ O (15.99 **u**). During the deposition, as the different elements evolving from the target towards the substrate, all the species in the plume are scattered by the gas molecules. The heavier elements trend to be scattered less significantly relative to the lighter elements. Therefore, Te, which is much heavier than Zn, and O, has a higher deposition rate under higher background pressure. Since the Te source is limited by that in the PLD target, therefore it must saturate as the background pressure increases further.

This scattering effect is observed in ZnO growth under the O_2 background pressure [55]. A few mtorr of O2 background pressure is usually used for ZnO PLD growth to maintain stoichiometric ratio between Zn and O. Although increasing O_2 pressure increases the Zn deposition rate due to the scattering effect, the O_2 gas also gives another source of O, and every O_2 molecule supplies two O atoms (or ions). Eventually a balance between O-deficient scattering effect and extra O supply in the O_2 gas can be achieved by adjusting O_2 background pressure . There are a few reports on the synthesis ZnO nanostructure by adjusting PLD Ar background pressure [18], which is beyond the scope of the discussion of this dissertation.

For O_2 pressure growth effect, intuitively both O and Te will compete for anion sites in the ZnOTe lattice, which should lower the Te incorporation rate under O_2 growth ambient, such effect is observed for PLD growth of ZnOSe [71]. However, a counter effect is observed for ZnOTe that increasing O_2 pressure increases the amount of Te in the resulting film. Besides the scattering effect, the O also has a tendency to bond with Te to form TeO_2 [115]. Evidence of TeO_2 formation can be observed from optical absorption shown in Figure 3.10b.

In Figure 3.10b, a blue shift of the absorption edge is observed with increasing O_2 pressure (also increasing film Te %). This can be attributed to the formation of TeO_2 phase, as TeO_2 has a wider E_{gap} of 3.7 eV [82]. Under the framework of HMA, alloying with more electronegative anion should narrow the band bap of the host material by developing a fully occupied subband above the host valence band [71][129][60]. E_{gap} reduction with increasing Te% is observed for the growth under Ar and N_2 pressure shown in Figures 3.10a and 3.10c. Therefore widening the optical E_{gap} with increasing film Te content indicates the formation of another wider band gap phase under O_2 pressure. Unfortunately, no direct evidence of TeO_2 can be observed from XRD due to small grains.

For N_2 pressure growth, increasing N_2 pressure increases the film Te content and narrows optical E_{gap} with increasing Te content as shown in Figure 3.9 and 3.10a. This indicates Te exists as an anion in the film by forming $ZnO_{1-x}Te_x$. N as group V element has been used as a P-type dopant for ZnO in multiple reports [83][36][104][64]. Structurally and optically N_2 ambient has similar effect as Ar. Its effect on electrical properties will be discussed in detail in Chapter 5 for electrical properties and doping of $ZnO_{1-x}Te_x$.

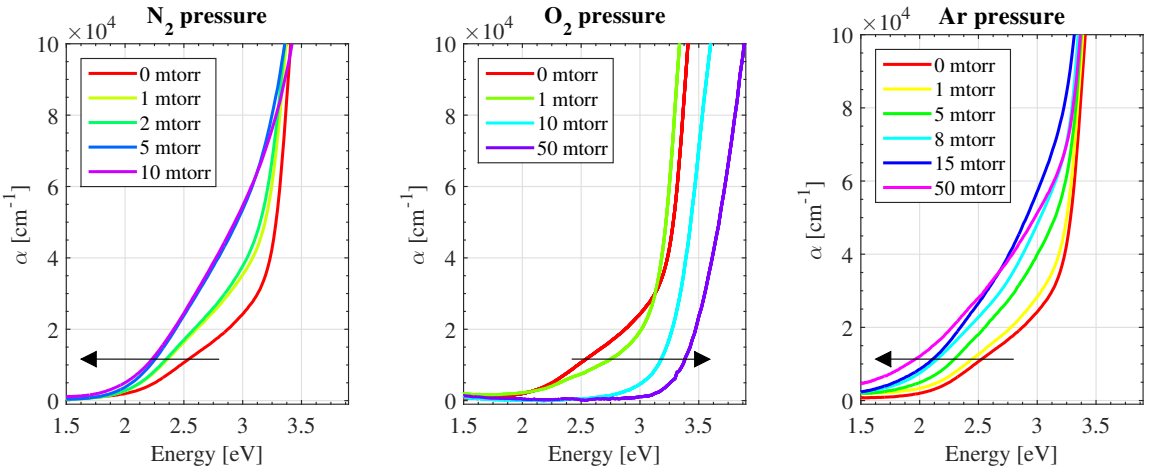

(a) α under N_2 pressure. (b) α under O_2 pressure. (c) α under Ar pressure.

Figure 3.10: Optical absorption α of $ZnO_{1-x}Te_x$ under N_2 , O_2 , and Ar pressure.

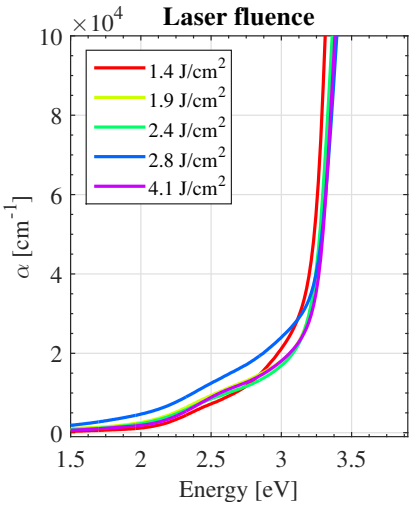

Figure 3.11: Optical absorption with respect to laser fluence.

Laser fluence

Laser fluence is a key factor for controlling $ZnO_{1-x}Te_x$ film crystallinity, film spatial uniformity, and electrical properties. It has negligible effect on the film Te content (shown in Table 3.2), and limited effect on the film optical absorption (Figure 3.11).

Higher laser fluence enlarges the crystal lattice parameter and grain size. Figure 3.12a shows a general left shift of $ZnO_{1-x}Te_x$ XRD (0002) diffraction peak. The FWHM of the diffraction peak (Figure 3.12b) decreases and grain size increases with increasing laser fluence. These effects are consistent with general PLD growth effect shown in Table 3.2. Higher laser fluence results in a plume with high kinetic energy and high ionic content, which

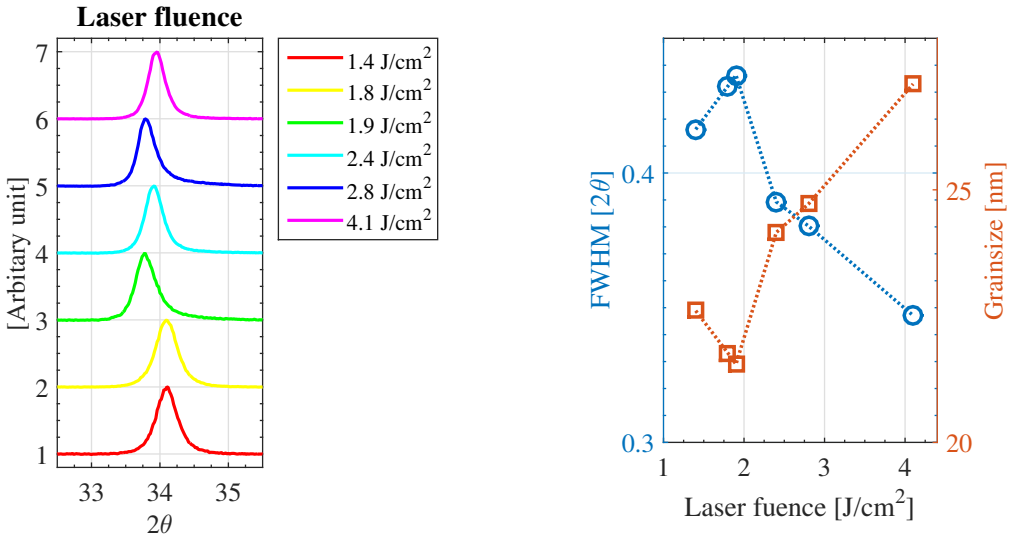

(a) $ZnO_{1-x}Te_x$ (0002) phase. (b) Fitted FWHM and grain size.

Figure 3.12: The impact of laser fluence effects on $ZnO_{1-x}Te_x$ crystallinity.

promotes atom motion and film nucleation on the surface. Hence, it increases the overall film crystallinity. However, if the laser fluence is too high, it causes splashing onto the film, which reduces the overall film smoothness.

Figure 3.13 shows that the film thickness increases with increasing laser fluence. With laser fluence increases from 1.4 J/cm^2 to 4.1 J/cm^2 the film center thickness increases from 120 nm to 372 nm, and the thickness spatial variation increases from 11% to 27% for 30 min growth duration. As discussed in Table 3.2, the growth rate increases with laser fluence. And the plume shape is narrower and more forward directed under higher laser fluence [48][7][19][116].

In addition, the electrical properties of $ZnO_{1-x}Te_x$ also depend strongly on the laser fluence. Figure 3.14 shows the resistivity of the film decreases from 2×10^{-1} to 2×10^{-3} Ω-cm with an increase of both electron concentraion and mobility (fluence increasing from 1.4 to 4.1 J/cm^2). The resistivity saturates when the laser fluence reaches 2.8 J/cm^2. This behavior can be attributed to an increase in both film crystallinity and O vacancy defects under high energy plume. The plasma plume has a highly forward scattered flux distribution. Upon arriving at the substrate surface the high-speed particles of the plume tend to sputter atoms from the surface of the film on the substrate and produce defects [48]. Under base chamber pressure (10^{-8} torr), the plume is O deficient [19] due to higher velocity of Zn^{2+} ions and ZnO neutrals in the plume. O vacancy has been regarded as a source of N-type conductivity in ZnO [49], thus higher fluence increases the film electron concentration. Also the increase in grain sizes improves electron mobility by reducing the grain boundary scattering effect [29]. However further increase in laser fluence will cause splashing effect on the film surface, which damages the film surface by producing microholes [48].

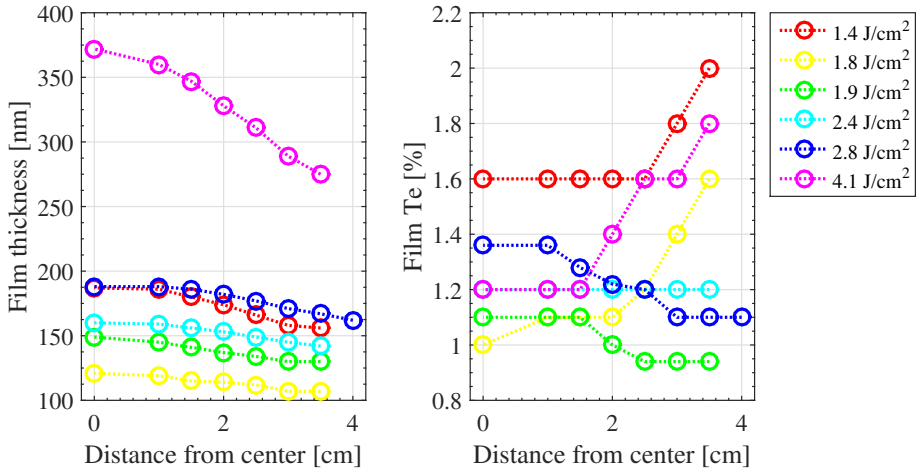

Figure 3.13: The impact of laser fluence on film thickness and Te% uniformity.

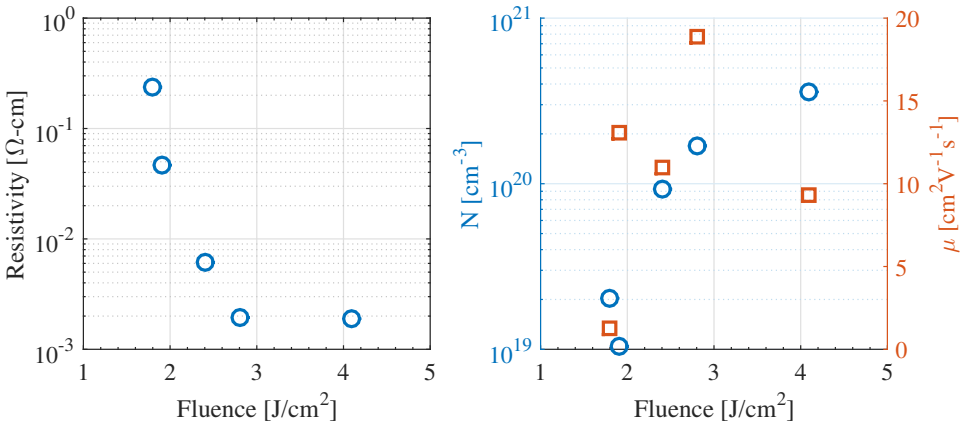

Figure 3.14: Laser fluence effect on $ZnO_{1-x}Te_x$ electrical properties.

Target substrate distance

Reducing the substrate-target distance has "similar" effects as increasing laser fluence on $ZnO_{1-x}Te_x$ film synthesis. It enhances $ZnO_{1-x}Te_x$ film crystallinity at center but lowers the spatial uniformity of the film. As the substrate moves closer to the ablation spot, the substrate is subjected to a less expanded plume, which is narrow and more forward oriented. Figure 3.15 shows that the film spatial thickness variation increases as the distance shortens (resembles the case of increasing fluence Figure 3.13). The grain size also increases as substrate moves closer to the target (Figure 3.16). Electrically, both the electron concentration and mobility increase as shown in Figure 3.17.

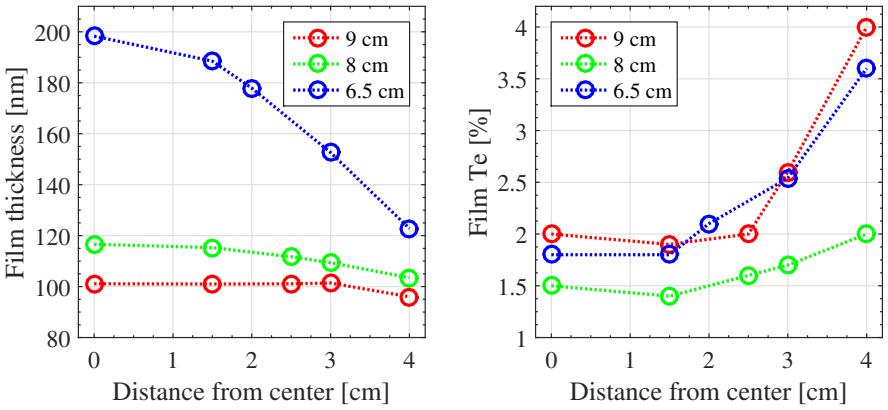

Figure 3.15: Film thickness of $ZnO_{1-x}Te_x$ with different substrate-target distances.

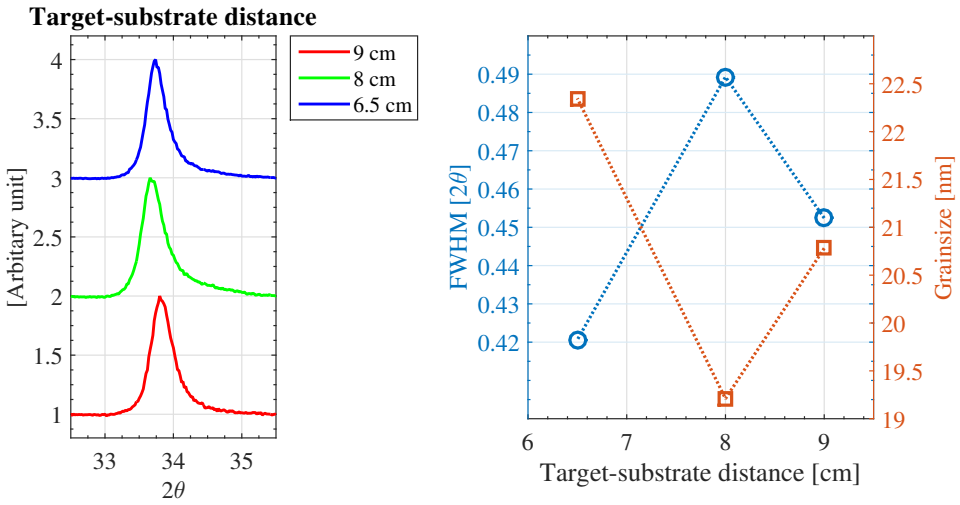

Figure 3.16: FWHM and grain size of $ZnO_{1-x}Te_x$ with different substrate-target distances.

3.4 Summary

Monophase, high crystallinity and high carrier mobility are desired criteria to achieve useful optoelectronic materials. The material growth conditions must be tuned precisely to achieve the intended properties. PLD growth parameter space for $ZnO_{1-x}Te_x$ has been explored and discussed in this chapter. Film crystallinity is strongly dependent on the alloy composition, substrate temperature, and the laser fluence. Film Te % is controllable through both the target ZnO:ZnTe powder ratio, and also the background gas pressure. The alloy synthesis chemistry is dependent on the type of background gas (reactive or inert) [32], and thus can be used as a doping strategy to control the material electrical properties, which will be further discussed in Chapter 5.

To achieve $ZnO_{1-x}Te_x$ alloy with moderate Te content (10%), high crystallinity and high

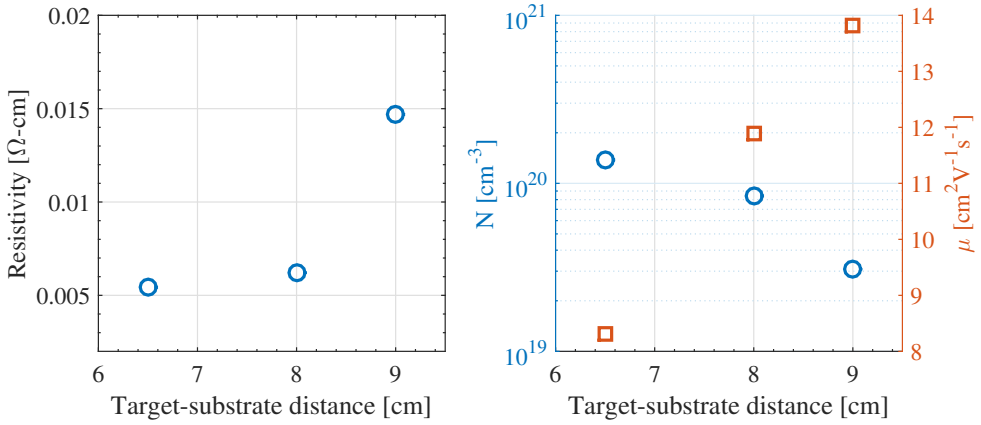

Figure 3.17: Electrical properties of $ZnO_{1-x}Te_x$ with different substrate-target distances.

carrier mobility, relatively high substrate temperature and high laser fluence (or shorter inter target-substrate distance) should be used. The desired film alloy composition can then be achieved with suitable target composition. To avoid the formation of TeO_2 phase, O_2 background gas should not be used. To achieve good N-type conducting material, Ar pressure from 1 to 5 mtorr yields the highest carrier mobility. To achieve P-type conductivity, N_2 gas can be used as a source of group V P-type dopant [125][64].

Chapter 4

$ZnO_{1-x}Te_x$ electronic band structure

To find an optoelectronic material that can serve as a top cell material in a double junction solar cell with Si bottom cell, as discussed in Chapter 1, the material should have these three major properties: 1). an optical band gap of 1.5 - 1.8 eV; 2). a good band alignment with Si; and 3). good electrical transport properties.

In the previous chapter, we have explored the technicalities of the synthesizing $ZnO_{1-x}Te_x$ alloys and how to control its material properties by tuning the growth conditions. In this chapter, we assessed whether the HMA framework can be applied on modeling the electronic band structure of the $ZnO_{1-x}Te_x$ alloy. Also we seek to determine if $ZnO_{1-x}Te_x$ can satisfy the first two criteria for the proposed double junction device. Section 4.1 discusses the determination of optical band gap of $ZnO_{1-x}Te_x$ at different Te content. Section 4.2, and 4.3 are in depth discussions on probing the CBM and VBM positions of $ZnO_{1-x}Te_x$ alloys by different X-ray spectroscopies. Section 4.4 discusses the BAC modeling of the optical absorption of $ZnO_{1-x}Te_x$, and proposes a band structure for this alloy across the whole composition range.

4.1 Optical band gap measurement by optical absorption

Optical absorption measurement is perhaps one of the most intuitive method for measuring optical band gap of a thin film semiconductor. As a photon impinges a thin film surface, one of four processes is happening: 1). the photon is reflected at the film surface; 2). the photon is scattered while transmitting across the film; 3). the photon is absorbed by the material; 4). the photon is transmitted through the film.

Experimentally, the normal direction transmission and refection are measured with a Perkin Ellmer 950 UV/Vis/NIR Spectrophotometer in wavelength range of 250 nm - 2500 nm. The spectral absorption coefficient is calculated by the Beer-Lambert Law, which states

the intensity of incident light beam decays exponentially inside an absorbing medium:

$$\begin{aligned} I &= (1-R)I_0 \exp(-\alpha t), \\ \frac{I}{I_0} &= T \end{aligned} \tag{4.1}$$

where I_0 and I are the light intensity reaching the film, and passed the film respectively. R, T, and α are reflection, transmission, and absorption coefficients respectively, and t is the film thickness. The underlying assumptions for this equation are: 1). the medium is uniform, i.e. α is not spatially dependent within the film; 2). the scattering and emission inside the film is negligible [43].

The absorption coefficient is also described as the reciprocal of skin depth under the electromagnetic theory framework with the Maxwell's equations [14]. For a plane electromagnetic field propagates in a medium, the energy decays exponentially with propagation depth, which leads to the relation:

$$\alpha = \frac{4\pi k}{\lambda_0}[m^{-1}] \tag{4.2}$$

where λ_0 is the wavelength in vacuum, k is the imaginary part of the refractive index of the medium.

In semiconductor physics, a semiconductor absorbs a photon by exciting a VB electron to CB. Thus, only photons with energy larger than the E_{gap} can be absorbed. Therefore, in many cases the onset of the absorption coefficient is representative to E_{gap} of the semiconductor. The carrier filling induced redshift of the optical E_{gap}, known as the Burstein Moss shift [88], is not considered here due to the relatively low carrier concentration in the materials studied in this work.

For a direct band gap semiconductor with parabolic bands, its absorption coefficient alpha is directly proportional to its optical joint-density of states [69] thus the square of alpha is directly proportional to the energy difference between incident photon energy and its E_{gap}, i.e. $\alpha^2 = \frac{2m^*_{e,h}}{\hbar}(\hbar\nu - E_{gap})$ [5]. A linear extrapolation of the onset of α^2 is a common method to determine E_{gap} in direct semiconductor [5].

Figure 4.1 shows the alpha spectrum for a polycrystalline ZnO sample synthesized in this study. An alpha square fitting yields an E_{gap} of 3.25 eV, which is consistent with the generally agreed value in literatures [95].

For $ZnO_{1-x}Te_x$, however, with the non-parabolic nature of the Te deep-level developed band, the α^2 fitting is no longer applicable. Figure 4.1 shows alpha spectra for six selected samples from pure ZnO to alloy with 23% Te. As Te content in the film increases, the absorption spectra shows a monotonic redshift, indicating E_{gap} of O-rich $ZnO_{1-x}Te_x$ decreases with x. The detailed analysis of the E_{gap} with respect to alloy composition is discussed in Section 4.4 of this chapter.

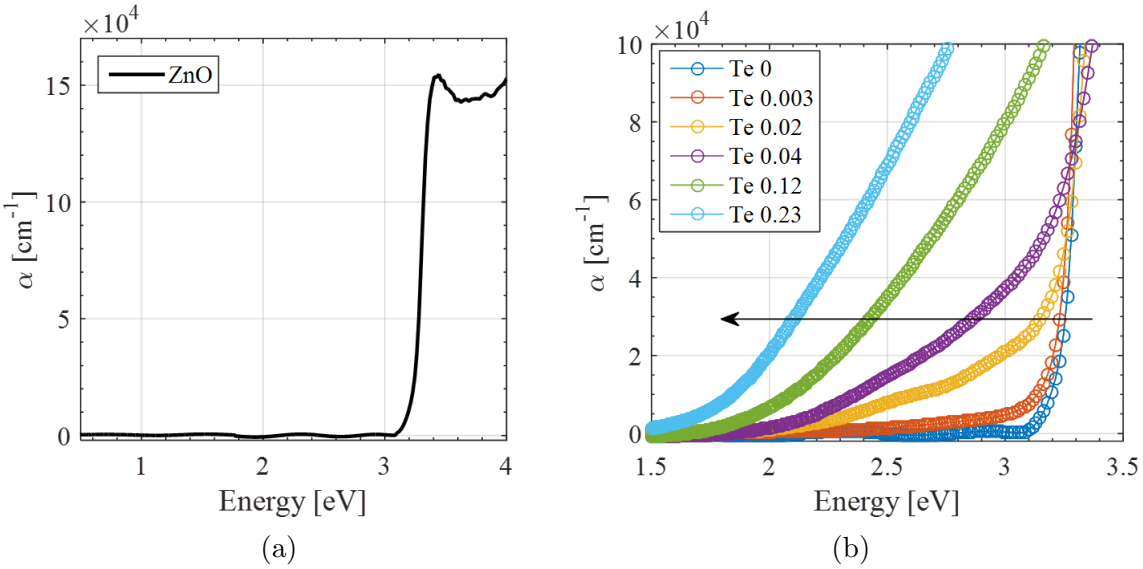

Figure 4.1: (a) Optical absorption coefficient α of a polycrystalline ZnO synthesized in this study. (b) α of polycrystalline $ZnO_{1-x}Te_x$, with x = 0 to 0.23.

4.2 Valence band edge measurement by X-ray photoelectron spectroscopy

XPS is a quantitative surface chemical analysis technique that measures the elemental composition, empirical formula, chemical state and electronic state of the elements that exist within a material [77]. During the experiment, a high energy X-ray photon eject an electron from the material according to photoelectric effect [28].

XPS experiments usually use either a monochromatic Al k-alpha X-rays or Mg K alpha X-rays or a synchrotron-based light source combined with a custom designed electron energy analyzer, which measures the kinetic energy of the photoelectrons.

The measurement is extremely surface sensitive. During the measurement, a photoemitted electron can undergo inelastic collisions, recombination, trapping in various excited states within the material, all of which can reduce the number of escaping photoelectrons. These effects appear as an exponential attenuation function as the depth increases. As a result, even though photoelectric effect happens deeper in the sample, only electrons with a few nanometer near the surface will escape the material without causing secondary electrons (which contributes to a nonlinear background in the signal, known as Shirely background [13][86]).

The measured kinetic energy of the ionized photoelectron equals the initial X-ray energy substract the binding energy of the electron and the work function of the material. The binding energy reflects the initial chemical environment of the element from which the electron was released. The relation is described by the equation based on the work of Ernest

Rutherford (1914):

$$E_{binding} = E_{photon} - (E_{kinetic} - \phi_{detector}) \tag{4.3}$$

where $E_{binding}$ is the binding energy of the electron, E_{photon} is the energy of the X-ray photon, $E_{kinetic}$ is the instrument measured kinetic energy of the photoelectron, and $\phi_{detector}$ is the work function dependent on both the spectrometer and the material. Figure 4.2a provides a schematic illustrating the physical process. First, the sample is put in contact with the detector (Au is used in our detector as a reference), so that the sample's E_F is aligned with the Au reference workfunction of the detector. With the measured $E_{kinetic}$, Au $\phi_{detector}$, and the incident photon energy, the $E_{binding}$ can be calculated.

A typical XPS spectrum is a plot of the number of electrons detected (y-axis) versus the binding energy of the electrons detected (x-axis). Each element produces a characteristic set of XPS peaks at characteristic binding energy values that directly identify each element that exists on the material surface. These characteristic spectral peaks correspond to the electron configuration of the elections with the atoms, e.g., 1s, 2s, 2p, 3s, etc. Figure 4.2b shows the XPS spectrum for a Au sample. The spectrum is usually analyzed in three regions: VB region, core-level region, and the secondary electron cut-off region. For $ZnO_{1-x}Te_x$, We focus our analysis on the VB region of the spectra to determine the relative shift of the VBM position with respect to Te content. The full XPS spectrum of $ZnO_{1-x}Te_x$ is shown in appendix C

The XPS instrument for this study uses a monochromated Al Kalpha X-ray source (hv = 1486.6 eV) with a hemispherical electron analyzer. The measured spectra were charge corrected to the adventitious carbon 1s spectral component binding energy [50][96].

In addition, a 3.5 mW laser with $\lambda = 405$ nm (3.06 eV) is used to determine the surface band bending, in order to correct the surface E_F pinning at E_{FS}, due to the surface dangling bonds. The band bending is determined by the shifting of the carbon 1s peak under dark and laser excitation conditions. Figure 4.3(left) shows carbon 1s spectra the sample of 14.6% Te, for dark and laser excitation conditions. Gaussian functions are fitted for each individual peaks in the graph, the carbon 1s peak position is determined as the mean of the Gaussian function for the higher intensity peak. For the 14.6% Te sample, the carbon 1s peak shifts to a higher energy under illumination, which indicates a downward band bending. While in dark, the surface E_F is assumed to be pinned at the universal E_{FS} level of -4.9 eV w.r.t. vacuum level [61][105]. Under the laser illumination, carriers are excited to saturate the surface dangling bonds. Figure 4.3(right) shows the band bending energy determined by the shifts of the carbon 1s peaks for 6 samples ranging from x = 0.006 to 0.32.

As shown in Figure 4.4, the VB energy regime of the XPS spectrum shifts monotonically to the lower energy with increasing Te content. To quantitatively determine the VBM shift, cumulative Gaussian function is used to fit the Te included feature in the XPS VB regime:

$$A(E) = \frac{K}{2}\left[1 - \text{erf}\left(\frac{E - E_S}{\sqrt{2}\sigma}\right)\right] \tag{4.4}$$

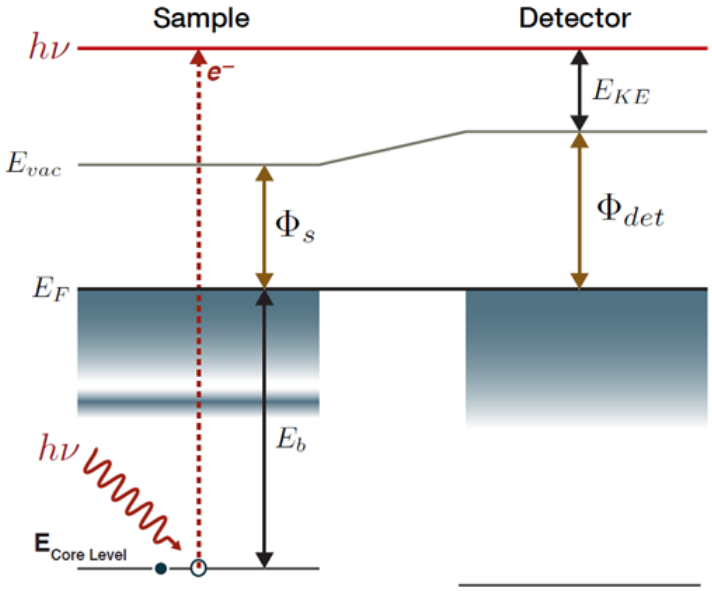

(a) XPS schematic. [13]

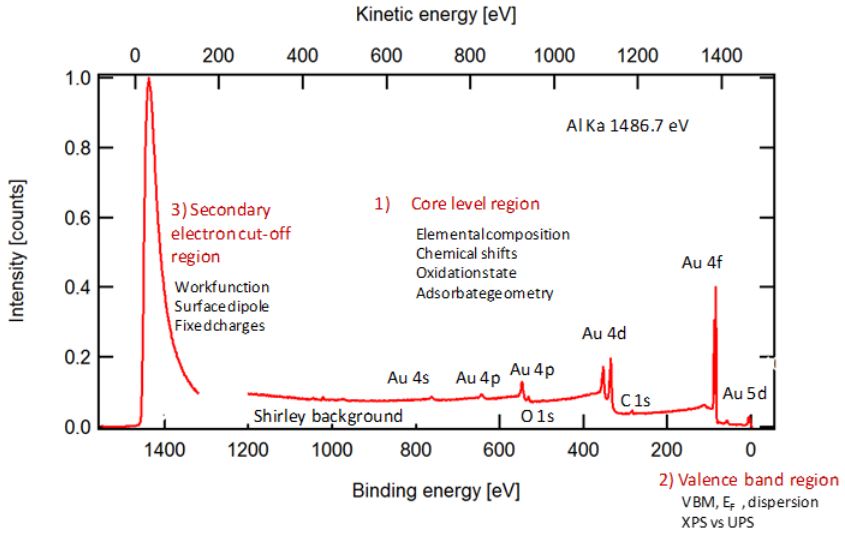

(b) Example XPS spectrum of a Au sample. [77]

Figure 4.2: (a) Illustration of the physical process of XPS experiment with the electronic band alignment of sample and XPS detector. (b) Example XPS spectrum of a Au sample, showing three energy regimes in the spectrum: 1) VB regime, 2) core-level regime, and 3) secondary electron cut-off regime.

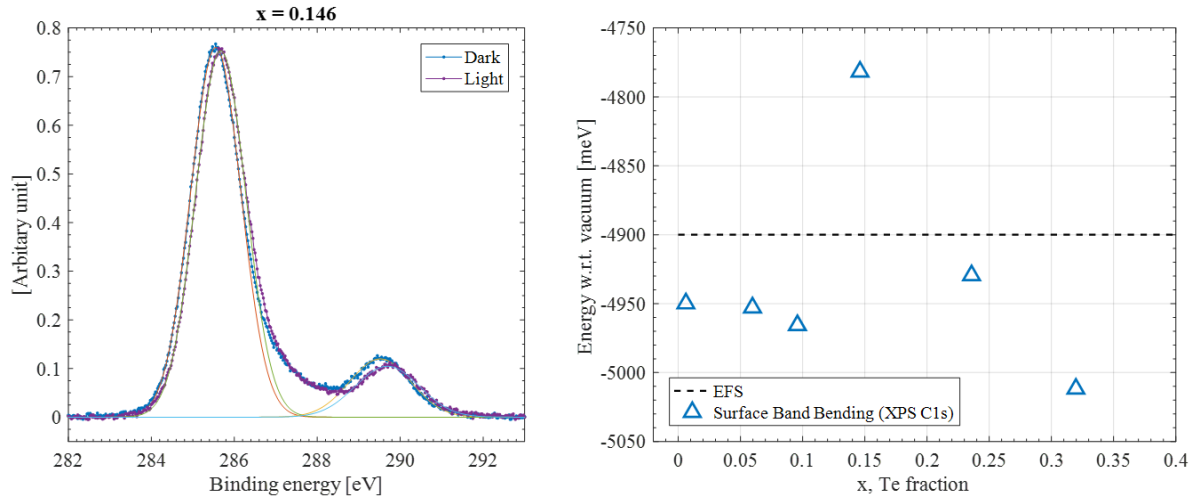

Figure 4.3: (Left) The XPS spectra near the carbon 1s peak for both dark, and laser illumination conditions for $ZnO_{0.854}Te_{0.146}$. (Right) The band bending energy determined by the shifts of the carbon 1s peaks for 6 $ZnO_{1-x}Te_x$ samples ranging from x = 0.006 to 0.32.

where, K is the step function amplitude, E_S is the step function transition energy, and σ is the Gaussian function broadening. The transition energy of the step function is determined as the position of the VBM.

The relative VBM position with respect to E_F is determined from the fitting in Figure 4.4. Both the determined VBM and E_F positions are plotted in Figure 4.5. The trend of $ZnO_{1-x}Te_x$ VBM position determined from the XPS experiment agrees with our expectation: VBM drastic upward shift (> 1.5 eV) is observed upon the addition of Te in ZnO, and the VBM energy shift increases monotonically with increasing Te content in the alloy.

4.3 Band edge measurements using synchrontron X-ray absorption / emission spectroscopies

The XES and XAS are common X-ray spectroscopies used to study semiconductor electronic band structures. These two X-ray techniques are directly related to each other and provide common as well as complimentary information on the electronic structure of a material.

XES is a consequence of the absorption of a photon and is therefore often referred to as a secondary process. In XAS, an inner-shell electron is excited into an empty electronic state by absorption of the incident X-ray phton, e.g. an 1s electron is excited into the 4p level. In XES, the electron hole that was created in the X-ray absorption process is filled by an electron from a higher orbital, e.g. a 2p electron fills the 1s hole.

An xas spectrum reflects the unoccupied density of electronic states while an emission spectrum is related to the density of occupied states. When plotted together the XES and

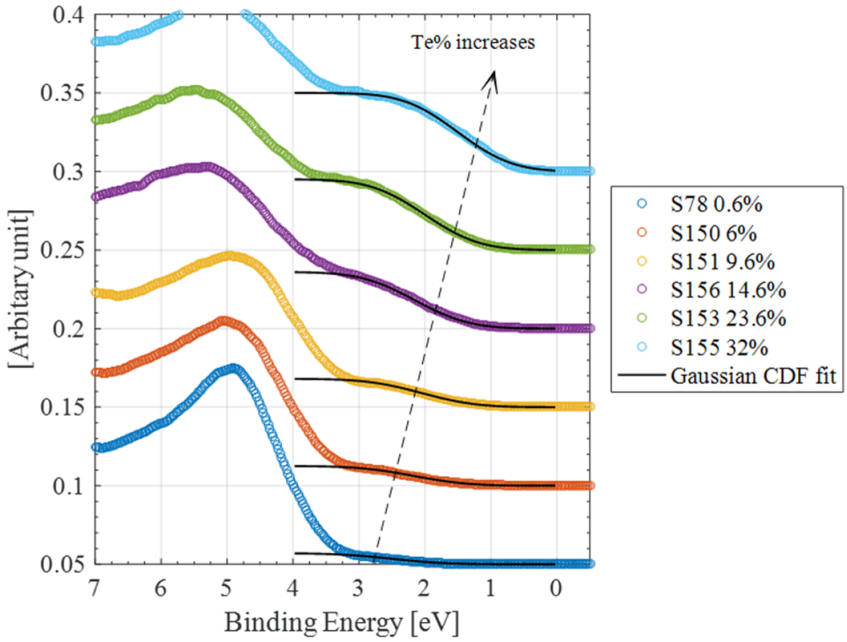

Figure 4.4: Cumulative distributed Gaussian function fitting of XPS spectrum in VB energy regime for six selected samples for Te = 0.6% to 32%.

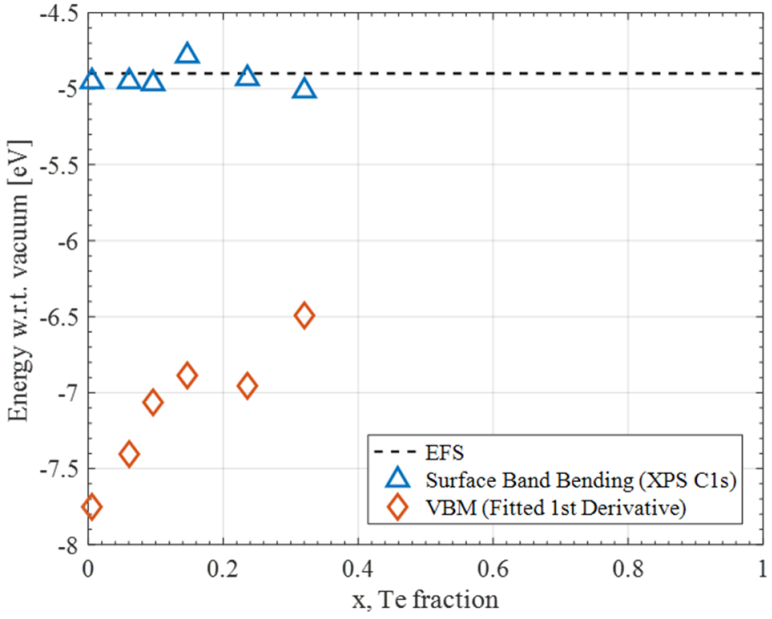

Figure 4.5: The VBM positions determined from the Gaussian fit and the E_F with respect to vacuum level.

XAS spectra (shown in Figure 4.6b), the spectra only overlap in the spectra tails because the XES shown probes the highest energy occupied states, whereas the XAS spectrum starts at the lowest energy unoccupied states [9].

The XAS/XES experiments in this study are performed at the Advanced Light Source (ALS) of the LBNL on Beamline 8.0.1, with X-ray energy ranging around oxygen K-edge (530 eV) under room temperature. For XAS experiment, a tunable energy source X-ray with energy less than 1 keV (lower than the Al K-α energy used in XPS), therefore it does not have enough energy to eject electron out of the material. In a semiconductor material, XAS photon excites a core-electron to the CB as shown in Figure 4.6a. The total excited electron yield (TEY) and the total fluorescence yield (TFY) are measured at each x-ray energy, thus it probes the CB partial DOS.

The XES uses a fixed energy X-ray source to excite core electrons into the CB. The excited electron then relaxes back to the core-level by emitting an X-ray photon. The emitted X-ray photons detected and counted, which represents the VB DOS.

Figure 4.7 a shows the XES and XAS (TFY) spectra obtained for seven samples ranging from pure ZnO to ZnOTe with 32 % Te.

The VBM and CBM positions are determined by using a linear extrapolation near the onset of the XES and XAS spectra respectively. Given the non-linear curvature of the XES near the spectra tail, the extrapolated VBM position depends strongly on the choice of extrapolation data range. The potential errors are determined by extrapolating the spectrum at different energy range, which are shown as the error bar in Figure 4.8. Both the VBM, and CBM for $ZnO_{1-x}Te_x$ with x $>$ 0 are determined relative the positions for pure ZnO. Despite the uncertainty in the exact value of the XES band edges, the measurement shows monotonic upward shift of VBM with increasing Te content.

The band edge positions for $ZnO_{1-x}Te_x$ found by the XPS, XES, and XAS experiments are plotted together in Figure **??** in Section 4.4 to illustrate the electronic band structure of $ZnO_{1-x}Te_x$ across the entire composition range.

4.4 Theoretical determination of the $ZnO_{1-x}Te_x$ dispersion relation

In Section 4.1, it is evidenced that the optical E_{gap} of $ZnO_{1-x}Te_x$ decreases monotonically with Te content, which reaches 1.5 - 1.8 eV range when x $>$ 20 %. Through X-ray spectroscopies, it is evidenced that there is an abrupt upward shift upon introducing Te in ZnO. To seek for quantitative understanding of the electronic band structure of $ZnO_{1-x}Te_x$, a simplified version VBAC is adopted to explain the experimental results.

The BAC theory has been widely accepted model for describing the electronic band structure in many HMA systems [71][129][113]. It works particularly well in the dilute composition limits in these alloys by treating the abrupt change at CBM and VBM as new

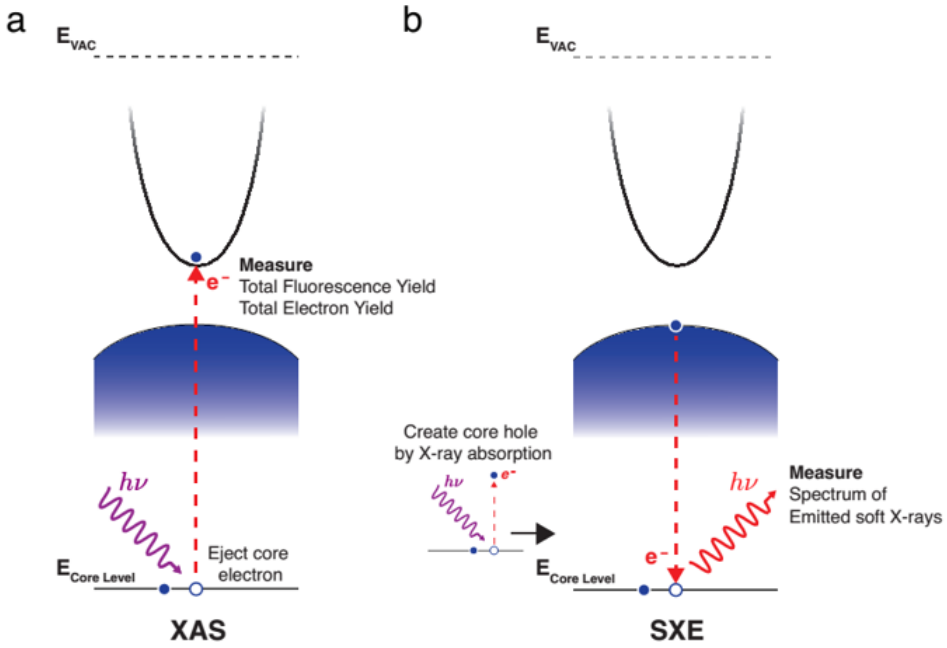

(a) Example schematic. [21]

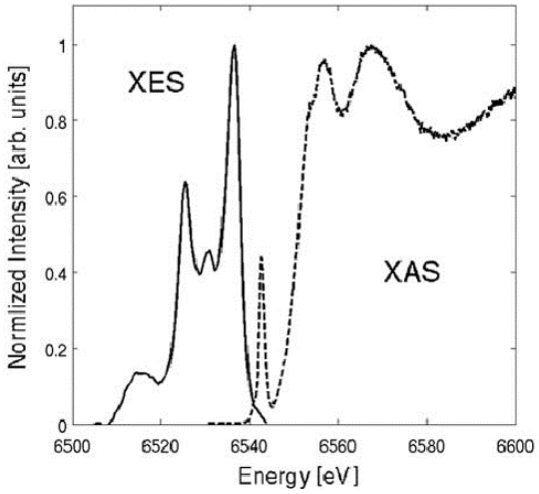

(b) Example Mn Nitrido spectrum [9].

Figure 4.6: (a) Illustration of physical process during an X-ray absorption and emission experiment within the electronic band structure of a material. (b) An example XAS / XES spectrum of Mn Nitrido [9] plotted on the same energy scale.

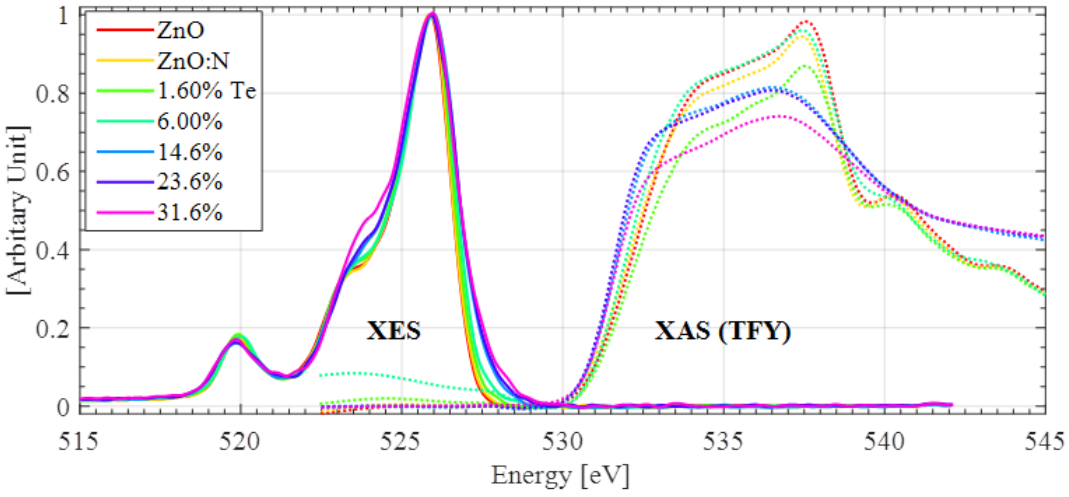

Figure 4.7: XES and XAS spectra for $ZnO_{1-x}Te_x$ samples with x = 0 to 32 %.

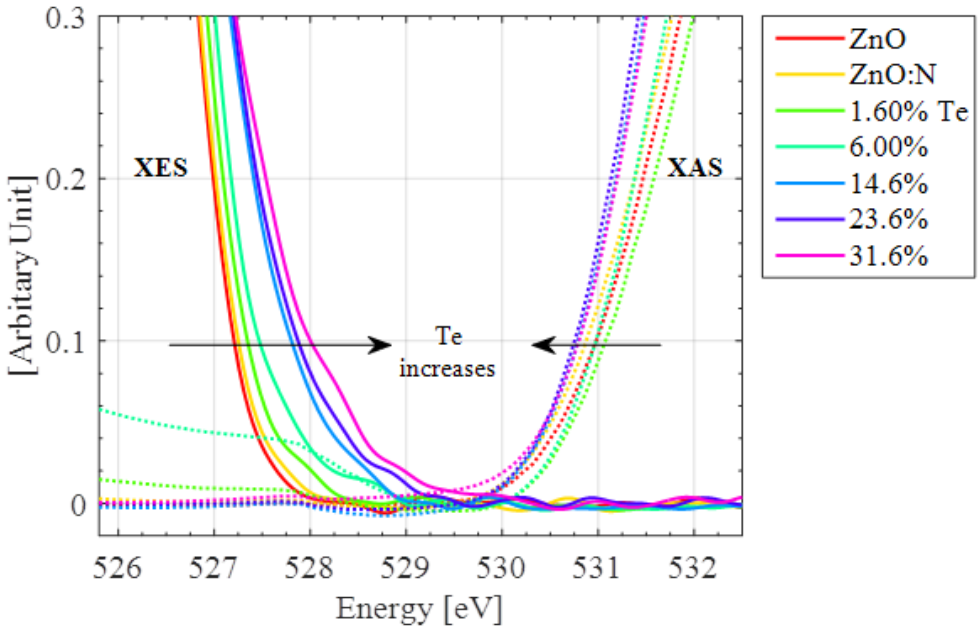

Figure 4.8: A zoomed view of XES/XAS spectra showing a monotonic right shift of VBM with respect to film Te content.

bands formed under the interaction of the mismatched minority anion deep levels and the host matrix bands. The band edge energies for the dilute ternary compounds are given by:

$$E_V^{\pm}(k) = \frac{1}{2}\left\{ \left[E_{V,ZnO}(k) + E_{Te}\right] \pm \sqrt{\left[E_{V,ZnO}(k) + E_{Te}\right]^2 + 4C_{Te}^2 x} \right\} \tag{4.5}$$

$$E_C^{\pm}(k) = \frac{1}{2}\left\{ \left[E_{C,ZnTe}(k) + E_O\right] \pm \sqrt{\left[E_{C,ZnTe}(k) + E_O\right]^2 + 4C_O^2 (1-x)} \right\} \tag{4.6}$$

where E_{Te} is the Te deep level above the ZnO valence band, E(k) is the dispersion of the ZnO valence band, C_{Te} is the coupling parameter describing the interaction strength between the extended valence band states and the localized Te states. It is important to note that x is the fraction of substitutional Te on O sites rather than total Te content.

The BAC results obtained in the dilute limits were compositionally weighted to extend the model for the whole composition range. This approach significantly overestimated the band gap reductions for the alloys in the mid-range composition [129]. The main deficiencies of the model were that it ignored the composition dependence of the coupling parameter and assumed that the BAC interactions fully determine the shifts of the CB and VB edges [91].

To address the deficiencies, the $ZnO_{1-x}Te_x$ band structure is approximated by VCA. Then the BAC is can be applied at every composition to treat the interaction between Te localized states and host VB extended states as perturbations. Mathematically, the VB and VB matrix band edges (i.e. wavevector k = 0), and effective masses are given by the linear interpolation between the end point compounds:

$$\begin{aligned} E_V &= (1-x)E_{V,ZnO} - xE_{V,ZnTe} \\ E_C &= (1-x)E_{C,ZnO} - xE_{C,ZnTe} \end{aligned} \tag{4.7}$$

where $E_{V,ZnO}$ and $E_{V,ZnTe}$ denote the VBMs, and $E_{C,ZnO}$ and $E_{C,ZnTe}$ denote the CBM of ZnO and ZnTe, respectively. Similar approximation is performed on the effective masses:

$$\begin{aligned} m_h^* &= (1-x)m_{h,ZnO}^* - xm_{h,ZnTe}^* \\ m_e^* &= (1-x)m_{e,ZnO}^* - xm_{e,ZnTe}^* \end{aligned} \tag{4.8}$$

where m_h^* and m_e^* are the effective mass of holes and electrons respectively. Also in the VCA approximation, the composition dependencies of the coupling parameters for $ZnO_{1-x}Te_x$ are given by:

$$\begin{aligned} C_O(x) &= xC_{O0} \\ C_{Te}(x) &= (1-x)C_{Te0} \end{aligned} \tag{4.9}$$

where C_{Te0} and C_{O0} are the coupling constants determined in the dilute O and Te composition limits [126][101].

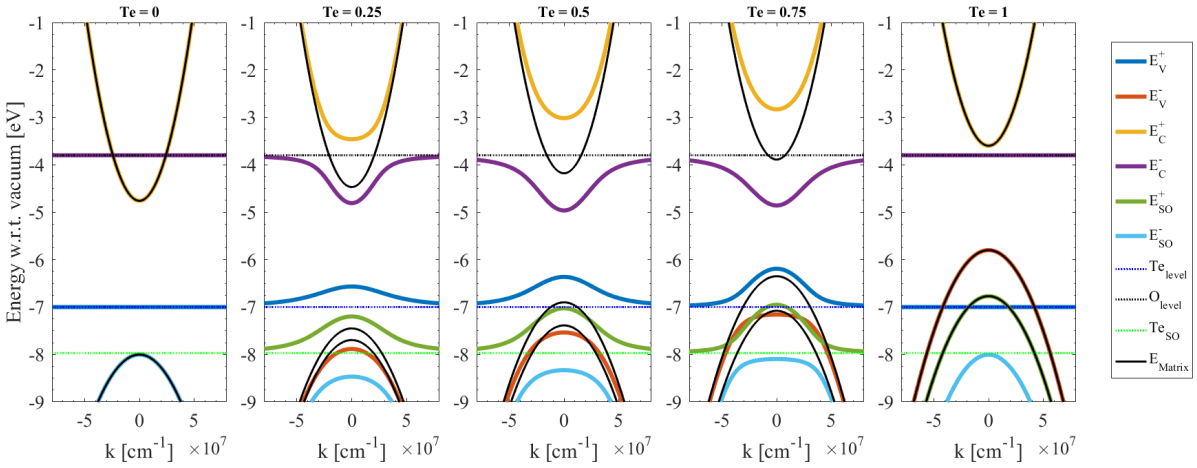

Figure 4.9: Calculated electronic band structure of $ZnO_{1-x}Te_x$ with the BAC model at x = 0, 0.25, 0.5, 0.75, 1.

Figure 4.9 illustrates the band structure of $ZnO_{1-x}Te_x$ at x = 0, 0.25, 0.5, 1, calculated using the BAC model. For all the calculations presented, E_{Te} at 0.95 eV above the VBM of ZnO and E_O at 0.2 eV below the CBM of ZnTe. The values $C_{O0} = 2.7$ eV and $C_{Te0} = 1.65$ eV as the coupling parameters [126].

In addition, because the p-like states of the heavy element Te have a relatively large spin-orbit splitting energy of 0.9 eV [80], we therefore included optical transitions from the spin-orbit split Te band to the conduction band. By assuming a weak interaction between the fully occupied valence bands, we decoupled the full 10×10 Hamiltonian from the $k \cdot p$ formalism [1] into five non-coupled 2×2 problems. A similar approach has been adopted previously in describing the VBAC interaction in the $ZnO_{1-x}Se_x$ alloy [71].

Consequently, the absorption spectrum for a $ZnO_{1-x}Te_x$ alloy film consists of eight optical transitions:

1. From Te derived band (E_V^+) to ZnTe matrix-like conduction band (E_C^+).
2. From Te derived band (E_V^+)to O derived band (E_C^-).
3. From Te spin orbital band (E_{SO}^+) to ZnTe matrix-like conduction band (E_C^+).
4. From Te spin orbital band (E_{SO}^+) to O derived band (E_C^-).
5. From Te spin orbital band (E_{SO}^-) to ZnTe matrix-like conduction band (E_C^+).
6. From Te spin orbital band (E_{SO}^-) to O derived band (E_C^-).
7. From ZnO matrix-like valence band (E_V^-) to ZnTe matrix-like conduction band (E_C^+).
8. From ZnO matrix-like valence band (E_V^-) to O derived band (E_C^-).

Also, to account for the band broadening inherent to the BAC model [119], we convolve the optical JDOS with a Gaussian function at each wave vector k. As a result, the optical absorption coefficient for a single transition can be written as an integral of the JDOS with respect to k:

$$g_+^-(\hbar\omega) = \frac{1}{4\pi\sqrt{\pi}(\Delta_C^- + \Delta_V^+)} \int \sin\left(\frac{\theta_V}{2}\right)^2 \sin\left(\frac{\theta_C}{2}\right)^2 \times \exp -\left\{ \frac{\hbar\omega - [E_-^C(k) - E_+^V(k)]}{(\Delta_C^- + \Delta_V^+)} \right\}^2 k^2 dk \tag{4.10}$$

Equation 4.10 calculates the optical coupling of the Te derived band ($E_+^V(k)$) and ZnTe matrix-like conduction band ($E_+^C(k)$). Δ_V^+ and Δ_C^- are the broadening parameters of ($E_+^V(k)$) and ($E_+^C(k)$) respectively. In addition, we have assumed that there is no optical coupling between extended and localized states, therefore the optical absorption is proportional to the delocalized part of the wavefunction of a given subband. This is effect is accounted by the first two factors under the integral, which represent the fraction of the delocalized states contribution to the optical transition [71], where:

$$\theta_V(k) = \arctan\left(\frac{2C_{Te}\sqrt{x}}{E_{V,ZnO}(k) - E_{Te}}\right) \tag{4.11}$$

The expression for the total absorption coefficient includes the all eight transitions discussed above, with each transition weighted by their degeneracy factor:

$$\alpha(\hbar\omega) = \alpha_0 \Big\{ \frac{2}{3}\big[g_+^+(\hbar\omega) + g_+^-(\hbar\omega)\big] + \frac{1}{3}\big[g_{SO_+}^+(\hbar\omega) + g_{SO_+}^-(\hbar\omega)\big] + \frac{2}{3}\big[g_-^+(\hbar\omega) + g_-^-(\hbar\omega)\big] + \frac{1}{3}\big[g_{SO_-}^+(\hbar\omega) + g_{SO_-}^-(\hbar\omega)\big] \Big\} \tag{4.12}$$

where α_0 is an overall scaling constant, which we obtained by fitting the optical absorption spectrum of ZnO. All eight weighted optical transitions are shown in Figure 4.10 ($ZnO_{0.77}Te_{0.23}$), the total calculated absorption coefficient is shown as the dash line.

Figure 4.11 shows the absorption coefficient fitting for eight selected $ZnO_{1-x}Te_x$ samples with x = 0 to 0.23. By fitting the experimentally measured absorption coefficient for $ZnO_{1-x}Te_x$ samples with BAC calculations, the VBAC parameters are obtained as: C_{Te0} = 1.65 eV, E_{Te} = 0.99 eV, and the band broadening ranges from: $\Delta_V^+ = 0.01 - 0.3$, $\Delta_V^- = 0.01 - 0.3$, $\Delta_{SO}^+ = 0.01 - 0.2$, $\Delta_{SO}^- = 0.01 - 0.2$, $\Delta_C^+ = 0.05 - 0.5$, and $\Delta_C^- = 0.1 - 0.4$.

Comparing the VBAC parameters obtained for $ZnO_{1-x}Te_x$ with those previously reported for $ZnO_{1-x}Se_x$, and $ZnO_{1-x}S_x$, we observed that C_{Te0} (1.65 eV) > C_{Se0} (1.2 eV) [71] > C_{S0} (0.6 eV) [50]. Since the mismatch in electronegativity and size in Te-O > Se-O > S-O, Te is expected to induce a stronger disruption in the potential energy in the ZnO lattice. With the BAC model, the E_{gap} of these $ZnO_{1-x}Te_x$ samples are determined, which shows drastic downward shifting at very low Te %.

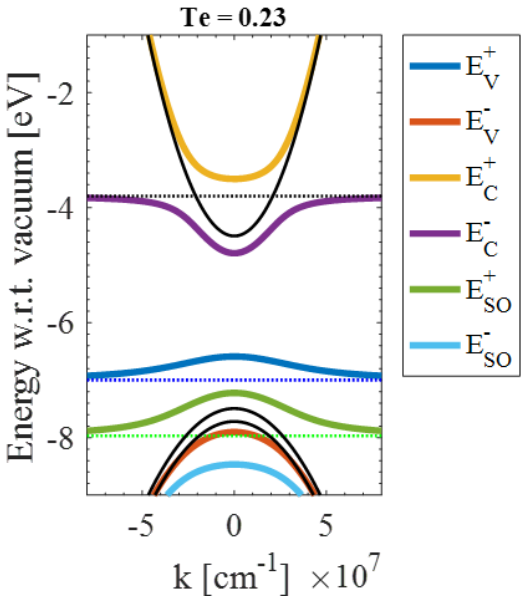

(a) $ZnO_{0.77}Te_{0.23}$ electronic dispersion.

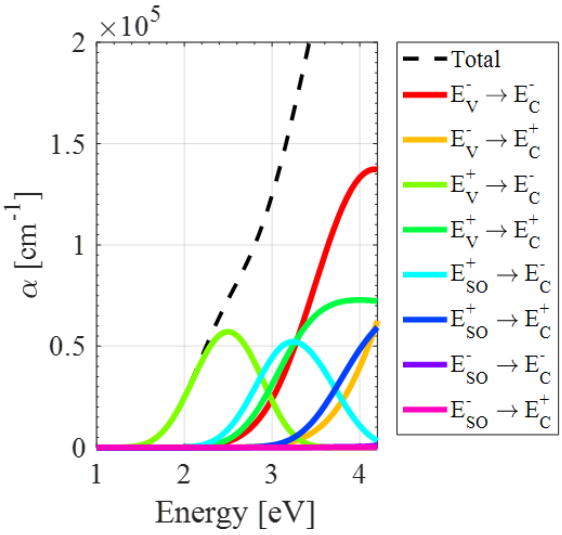

(b) Absorption coefficient for all possible energy transitions.

Figure 4.10: BAC calculated electronic band structure of ($ZnO_{0.77}Te_{0.23}$), and calculated optical absorption for each of the eight transitions discussed in 4.4.

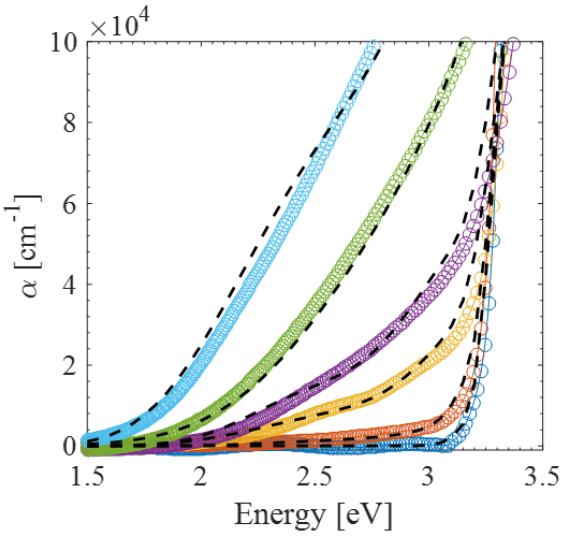

(a)

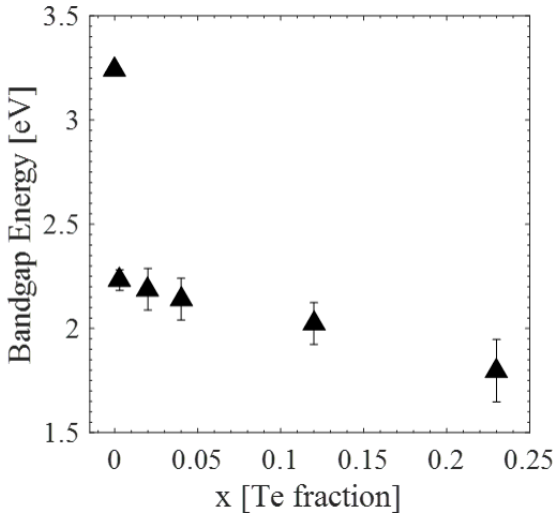

(b)

Figure 4.11: (a) Fitting α calculated from BAC to measured optical absorption spectra. (b) E_{gap} values determined from α fitting.

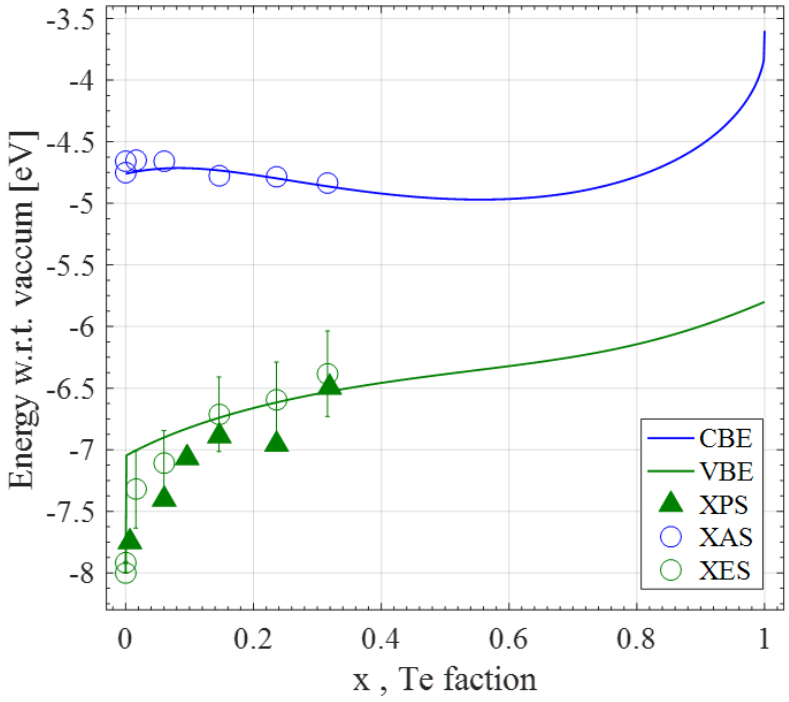

Figure 4.12: Comparison of VBM and CBM predicted by BAC model and experimentally determined values from XPS, and XES\XAS.

4.5 Summary

Combining the VBAC parameters obtained in this work with the CBAC parameters reported in literature [126], we have calculated the compositional dependent valence band and conduction band edges of the $ZnO_{1-x}Te_x$ alloy across the whole composition range (shown in Figure 4.12). The BAC calculation reveals that the drastic band gap reduction on the O-rich side is primarily due to the upward shift of the valence band, which is attributed to the anticrossing interaction between the ZnO delocalized VB states and Te localized states. The upward shift of the valence band is confirmed with the XPS, and XES\XAS measurement results. The experimental results show a good agreement with the electronic band structure described by the BAC model.

The results in Figure 4.13 show that $ZnO_{1-x}Te_x$ with x = 0.23 has the direct E_{gap} of 1.8 eV and the CBM energy at about 4.9 eV below the vacuum level. This configuration provides a good candidate for the top cell material in a Si-based double junction tandem solar cell. $ZnO_{0.77}Te_{0.23}$ together with Si have divided the solar spectrum in two equal parts and $ZnO_{0.77}Te_{0.23}$ provides a good band alignment with the VBM of Si located at 5.1 eV below the vacuum level.

In addition, the abrupt Te-induced VB upward shift can potentially alleviate the P-type

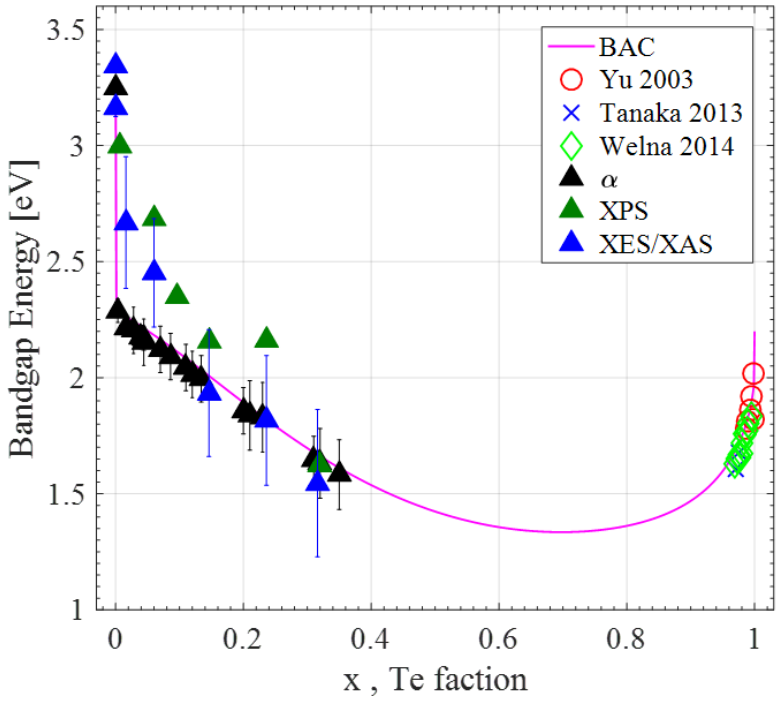

Figure 4.13: Comparison of E_{gap} predicted by BAC model and experimentally determined E_{gap} from optical absorption α, XPS, and XES\XAS.

doping difficulty in ZnO, which originates from the low VBM at 8.1 eV below the vacuum level. The electrical properties and the doping effects of $ZnO_{1-x}Te_x$ will be discussed in Chapter 5.

Chapter 5

$ZnO_{1-x}Te_x$ doping and electrical properties

It has been shown that the undoped ZnO thin film preferred to be highly N-type conductive [48], which pins its E_F close to its CBM. As discussed in Chapter 4, adding Te in ZnO leads to a > 1 eV upward shift in the host VBM. According to the Amphoteric defect model (ADM) [112], such band structure modification leads to significant change in the charge balance among different types of defects. It encourages the formation of acceptor-like defects, which compensates the native donors in sample, and makes the material less N-type.

Intrinsic $ZnO_{1-x}Te_x$ thin films synthesized in this study are N-type conductive. The compositional dependence of electrical properties of $ZnO_{1-x}Te_x$ is discussed in Section 5.1. Section 5.2 discusses the P-type doping effects by using group V nitrogen.

5.1 Undoped $ZnO_{1-x}Te_x$

In order to isolate the Te effect on the electrical properties and eliminate the contribution from grain boundary scattering, a series of $ZnO_{1-x}Te_x$ samples with similar grain size but varying Te% from 0.6 % to 13.4 % are selected for the study.

The grain size of the selected samples (calculated from FWHM of XRD spectra) are around 20 nm as shown in Figure 5.1(a). In Figure 5.1(b), both mobility and electron concentration of the $ZnO_{1-x}Te_x$ samples decrease with increase Te content, and hence increasing resistivity as shown in Figure 5.1(d). The resistivity has increased over three orders of magnitude with increasing Te content from 0.6 % to 13.4 %.

In conventional semiconductor systems, such as Si, a decrease in electron concentration usually yields an increase in electron mobility, due to the reduction of ionized impurity scattering centers. The counter intuitive behavior in our samples indicates an increase in carrier compensation ratio [21] in the material upon Te incorporation. In all semiconductors, there exists both donor-like defects and acceptor-like defects, and the ratio of the two types of defects governs the net electrical conductivity type. We speculate that adding Te have

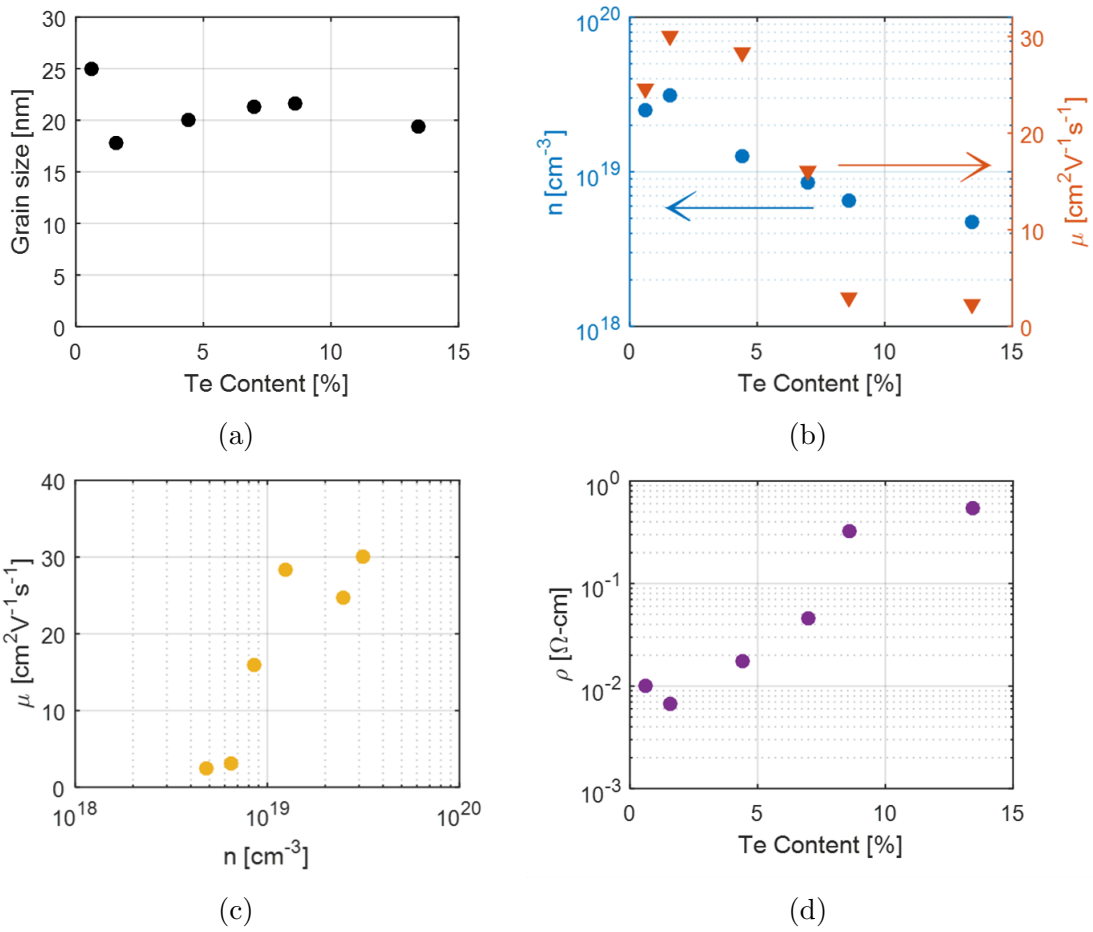

Figure 5.1: (a) The grain size of the selected samples are around 20 nm. (b) Both of the electron concentration and mobility decrease with increasing Te content. (c) The variation of the electron mobility with respect to electron concentration. (d) Resistivity has increased over three orders of magnitude with increasing Te content from 0.6 % to 13.4 %.

enhanced the formation of donor-like defects, which lowered the overall measured electron concentration. At the same time, the total amount of ionized impurity scattering centers is increased. Hence, it lowered the carrier mobility.

To quantify the carrier compensation ratio in $ZnO_{1-x}Te_x$, the theoretical carrier mobility dependence on carrier concentration is calculated with respect to different carrier compensation ratio. The total electron mobility of $ZnO_{1-x}Te_x$ involves the contributions from acoustic phonons, polar optical phonons, ionized impurities (Coulombic) scattering, and Te introduced alloy scattering. Matthiessen's rule is employed to include all the mobility-limiting

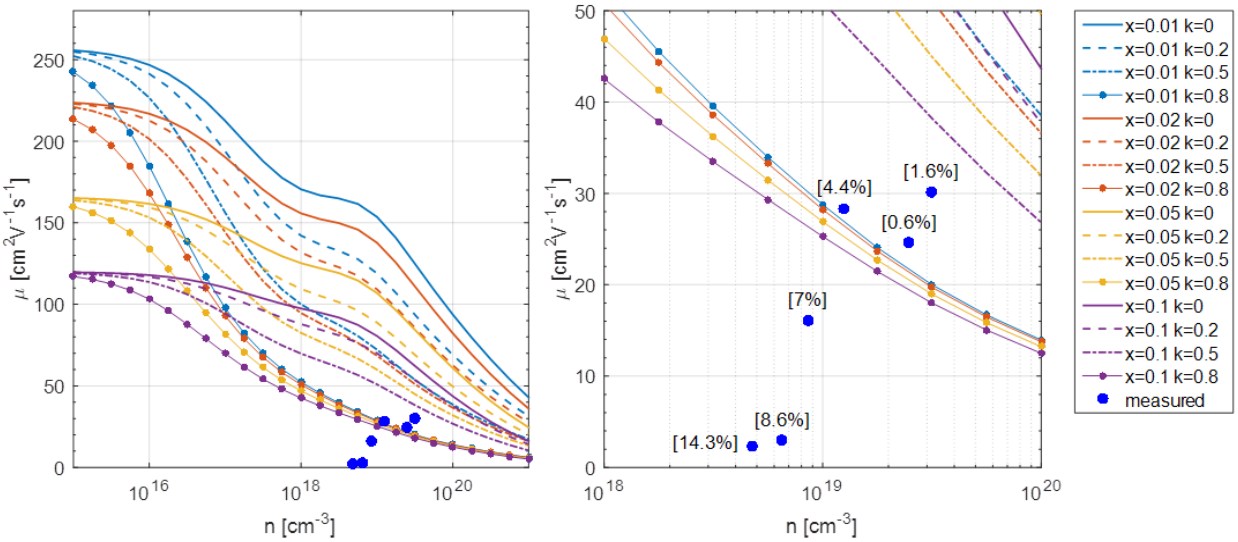

Figure 5.2: Calculated dependence between electron concentration and mobility at different carrier compensation ratios, and different Te %.

effects:

$$\frac{1}{\mu_e} = \frac{1}{\mu_{acoustic\ phonon}} + \frac{1}{\mu_{optical\ phonon}} + \frac{1}{\mu_{ionized\ impurity}} + \frac{1}{\mu_{alloy\ scattering}} \tag{5.1}$$

By following the procedures laid out in Reference: [44], the electron mobility is calculated for four compensation ratios (k = 0, 0.2, 0.5, and 0.8) and for four Te alloy compositions (Te = 1 %, 2 %, 5 %, and 10 %). Figure 5.2 shows the calculated mobility at 300 K. The mechanisms considered by are piezoelectric scattering from acoustic phonons, deformation potential mode scattering from acoustic phonon, scattering from optical phonons, ionized impurity scattering, and alloy scattering.

At high electron concentration regime ($n > 10^{20}$ cm^{-3}), the ionized impurity scattering is the limiting factor to the total mobility. As shown in Figure 5.2(left), at high electron concentration, the mobility of samples with similar compensation ratio k converges regardless the Te%. At low electron concentration regime ($n < 10^{16}$ cm^{-3}), the Te introduced alloy scattering is the limiting factor to the total mobility. As shown in Figure 5.2(left), at low electron concentration, the mobility of samples with similar Te% converges regardless the compensation ratio k. At Te = 0%, the calculated room temperature mobility agrees with the ZnO mobility calculation in literature [48].

It is evidenced that the $ZnO_{1-x}Te_x$ thin films synthesized in this study have relatively high compensation level (k > 70%). The sample with Te > 5 %, has a compensation below 80 %, and for samples with Te > 5 %, the compensation ratio is much beyond 80 %. The calculation agrees with our speculation that increasing Te% increases the compensation ratio in $ZnO_{1-x}Te_x$ alloy.

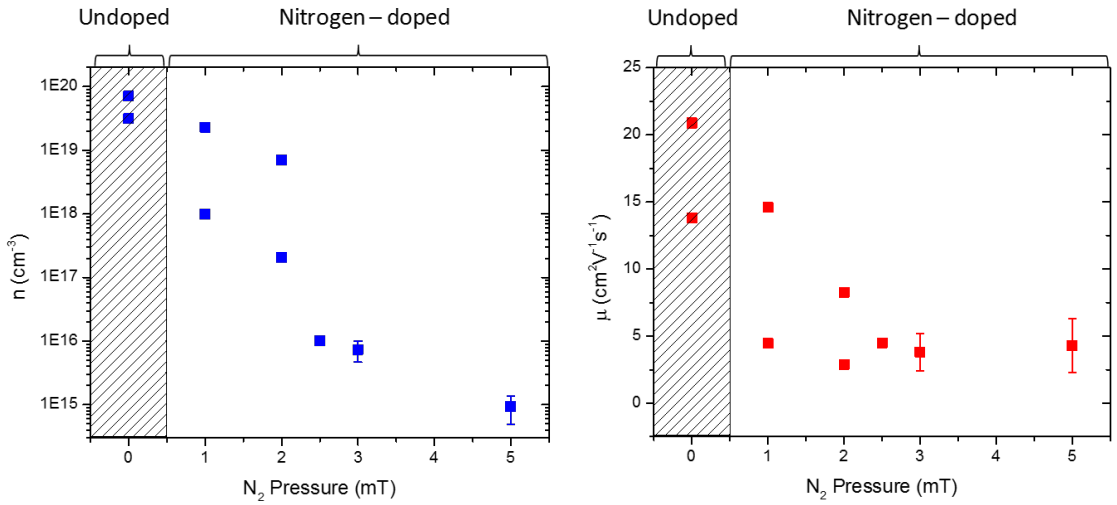

(a) (b)

Figure 5.3: (a) $ZnO_{1-x}Te_x$ electron concentration and (b) mobility variation with respect to N_2 background pressure applied.

5.2 P-type doping of $ZnO_{1-x}Te_x$ with nitrogen

In this work, we attempted to dope $ZnO_{1-x}Te_x$ P-type with nitrogen, which is regarded as one of the most promising P-type dopant for ZnO [49]. Despite nitrogen being the 'industry leader', it is still ineffective because it is a deep acceptor in ZnO with an ionization energy of 1.3 eV above the VB of ZnO [97][49]. In Chapter 4, it has been shown that replacing several percent of oxygen atoms with Te atoms raises the valence band by > 1 eV. In this case, the nitrogen may become a shallow acceptor in $ZnO_{1-x}Te_x$.

During the deposition, nitrogen is introduced by film growth under N_2 gas ambient. As shown in Figure 5.3, all the nitrogen doped films still show N-type conductivity, but the electron concentration has decreased over five orders of magnitude with N_2 pressure increased from 0 torr to 5×10^{-3} torr. At the same time, the electron mobility also decreased from 22 to 3 $cm^2V^{-1}s^{-1}$.

In order to isolate the Te, and N effects on the electrical property, control experiments are performed with ZnO and under Ar background pressure. Figure 5.4 shows the electron concentration of both ZnO, and $ZnO_{1-x}Te_x$ under Ar (hollow symbols) and N_2 (solid symbols) background pressure.

For ZnO, under Ar background pressure, the film electron concentration remains high (10^{19} to 10^{20} cm^{-3}). The electron concentration dropped to 3×10^{17} under 15 mtorr N_2 pressure. $ZnO_{1-x}Te_x$ has shown more drastic changes as electron concentration dropped from 10^{19} to 10^{15} cm^{-3} by using 5 mtorr of N_2 pressure instead of 5 mtorr of Ar pressure.

For growing under N_2 gas ambient, increasing carrier compensation is observed with increasing N_2 gas pressure for both ZnO and $ZnO_{1-x}Te_x$. Therefore, we speculate that,

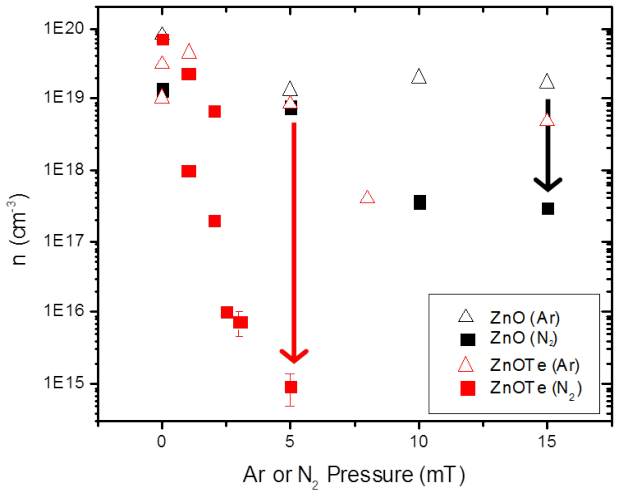

Figure 5.4: Electron concentration of $ZnO_{1-x}Te_x$ and ZnO under Ar and N_2 background pressure.

some nitrogen has been activated as acceptors which compensates the native donors and causes a drop in electron concentration. Also the activated nitrogen acceptors increased the ionized impurity scattering, and hence lowered carrier mobility.

It is worth noticing that adding Te has enhanced the activation of nitrogen acceptors, as more drastic decrease in electron concentration was observed. Nevertheless, the acceptor activation rate for $ZnO_{1-x}Te_x$ is still not high enough to achieve a P-type conductive material yet.

In addition, under 5 mtorr of N_2 gas pressure, the total nitrogen content in the film is 3%, measured by nuclear reaction with α particles (experimental detail is discussed in appendix B). If all of the 3% nitrogen were activated as acceptors, it should have compensated all the native donors and resulted in a P-type conductivity with 10^{21} hole concentration. Given the resulting films still show N-type conductivity, we think only a small fraction of N in the film are activated as acceptors. One possible reason is the strong triple bond in an N_2 molecule makes it difficult to sparate into individual nitrogen atoms upon incorporation into the film.

Room temperature Seebeck coefficient of the $ZnO_{1-x}Te_x$, and ZnO are measured to further verify the electrical conductivity type. (The detailed Seebeck coefficient measurement setup is discussed in Appendix H.) As shown in Figure 5.5, the negative Seebeck coefficient verified electrons are the dominate electrical carriers for all the samples. The theoretical Seebeck coefficient is calculated as a function of electron concentration following the formulation given in [15][103]:

$$S = -\frac{1}{qT}\frac{\int \tau\nu^2(E-E_f)\frac{\partial f_0}{\partial E}D(E)dE}{\int \tau\nu^2\frac{\partial f_0}{\partial E}D(E)dE} \tag{5.2}$$

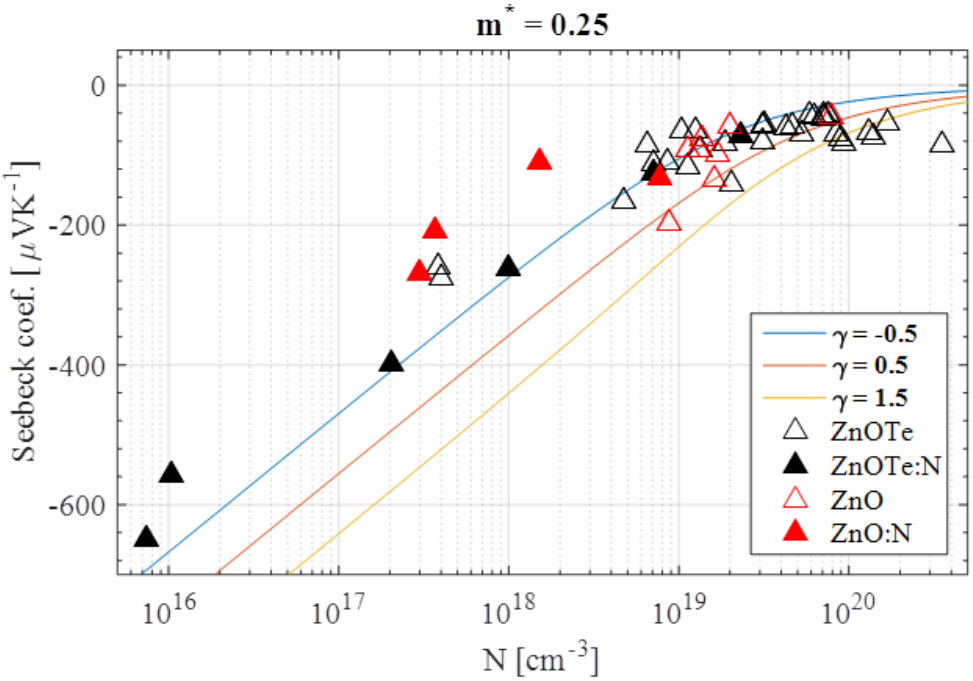

Figure 5.5: Seebeck coefficient for nitrogen doped and undoped $ZnO_{1-x}Te_x$, ZnO with respect to electron concentration.

where τ is the electronic relaxation time, which is usually dependent on electron energy a $\tau \sim E^{\gamma}$. The value of γ depends on the scattering mechanism: $-\frac{1}{2}$ for acoustic phonon scattering, $\frac{1}{2}$ for optical phonon scattering, and $\frac{3}{2}$ for impurity scattering. $D(E)$ is the DOS of electrons, here the CB DOS of ZnO is used, with electron effective mass m_e^*=0.28 [49].

Expanding Equation 5.2 with $\tau \sim E^{\gamma}$ and DOS, we have:

$$S = -\frac{1}{qT}\frac{\int (E-E_0)^{\gamma+1}(E-E_f)\frac{\partial f_0}{\partial E}D(E)dE}{\int (E-E_0)^{\gamma+1}\frac{\partial f_0}{\partial E}D(E)dE} \tag{5.3}$$

where E_0 is the CBM (for N-type semiconductor). As shown in Figure 5.5, it is counter-intuitive that the measured data fits the best with the acoustic phonon as the dominate electron scattering mechanism. In most cases, acoustic phonon scattering is more pronounced under low temperature [85], and given the $ZnO_{1-x}Te_x$, the impurity scattering is expected to be the dominate scattering mechanism.

We speculate this is due to the high electron compensation ratio ($>$ 80 %) in the $ZnO_{1-x}Te_x$ and ZnO discussed in Section 5.1, that the real electron concentration should be higher than the measured values. Also, the nitrogen doping should further increased the electron compensation. To correct for the carrier compensation effect, the measured data point should be shifted to the higher electron concentration level.

5.3 Summary

In this chapter, we have discussed the contribution of Te to the electrical properties of undoped $ZnO_{1-x}Te_x$. Also, we studied the doping effect of group V nitrogen in both ZnO, and $ZnO_{1-x}Te_x$ to prove the improvement in P-type doping effectiveness in ZnOTe over pure ZnO.

Alloying Te in ZnO has increased the overall carrier compensation in the material by increasing the tendency of acceptor-like defect formation. Polycrystalline O-rich $ZnO_{1-x}Te_x$ (i.e. $x < 0.15$) in this study are N-type conductive natively, both the electron mobility and concentration have dropped simultaneous upon increasing Te content. Doping with group V nitrogen has reduced the electron concentration of the ZnOTe over five orders of magnitudes. Comparing to pure ZnO, ZnOTe offers a higher nitrogen acceptor activation efficiency, as shown in Figure 5.4. However, the nitrogen acceptor activation rate is still not high enough to achieve P-type conductivity in $ZnO_{1-x}Te_x$ yet.

As shown in Figure 5.2, the carrier compensation ratio of undoped ZnOTe is very high ($\geq$80%). To achieve P-type ZnOTe, efforts are needed to further reduce the carrier compensation ratio of the starting material, by fine tuning the growth temperature, ambient gas type, pressure, and etc. In addition, other group V (P, As, and Sb) may also be tried as P-type dopant candidates.

Chapter 6

$GaN_{1-x}Sb_x$ Synthesis and Electronic Band Structure

GaN is a direct E_{gap} semiconductor commonly used in the LED industry since 1990s. Also because of its high resistance to ionizing irradiation, it has been used in solar cell arrays and various electronics in satellites [102][47]. Similar to ZnO, GaN has a Wurtzite crystal structure, with a wide band gap of 3.4 eV. High quality GaN thin films have been synthesized by a wide variety of methods, including PLD, MBE, Metal organic chemical vapor phase deposition (MOCVD), and etc. Given the highly-mismatched nature of $GaN_{1-x}Sb_x$ (similar to the case of $ZnO_{1-x}Te_x$ discussed in Section 3.1), GaNSb thin films studied in this work are synthesized by a non-equilibrium growth method low temperature molecular beam epitaxy (LT-MBE). The GaNSb film growth is discussed in Section 6.1 and 6.2. The electronic band structure determination of $GaN_{1-x}Sb_x$ is discussed in 6.3.

6.1 Molecular beam epitaxy growth of $GaN_{1-x}Sb_x$

MBE technique was invented in 1968 - 1973 in the IBM Watson Lab and the Bell Labs, it is regarded as the tool that enabled nanotechnologies. MBE has rich history of growing III-V semiconductors, starting with GaAs in 1968 for its wide E_{gap} and high electron mobility, which makes GaAs a good candidate for high-speed electro-optical devices. By the late 1970s, researchers had been able to implant dopants at precise locations in the semiconductor nanostructure. Such design and fabrication of new semiconductor materials by MBE has been described as "bandgap engineering" [73].

MBE allows researchers to make new materials and nanostructures by, in other words of the The New York Times, "spray printing a surface slowly with atoms or molecules" [11]. Pure sources of material are vaporized in separate ovens, and the atoms or molecules released by the sources are transported as a 'beam' to a substrate, where they are deposited [17].

$GaN_{1-x}Sb_x$ MBE growth is a non-equilibrium process where a Ga, and Sb vapor beam from an effusion cell and an activated nitrogen beam from a plasma source are directed toward

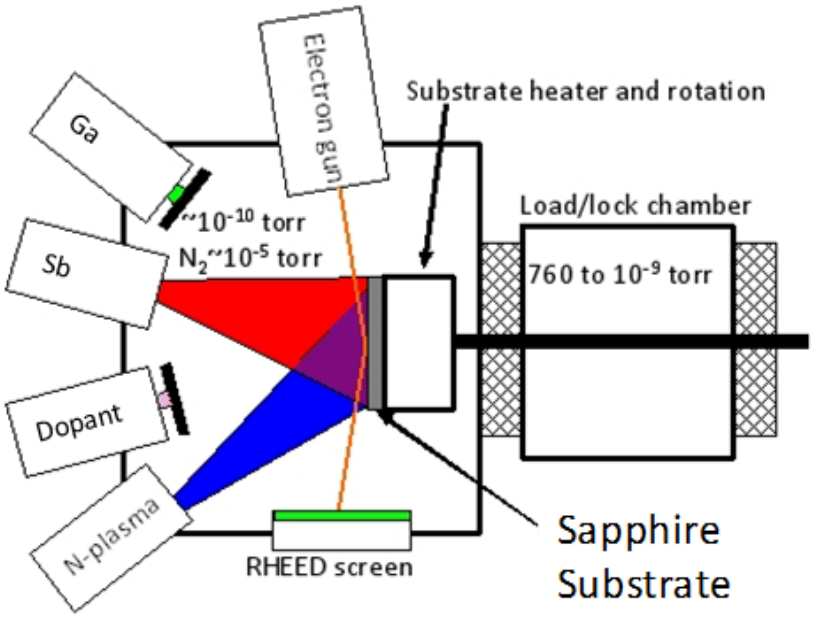

Figure 6.1: MBE system schematic with Ga, Sb, N-plasma source.

a heated substrate in an ultra-high vacuum chamber, as shown in Figure 6.1. The activated nitrogen beam is supplied by a DC plasma source, which excites neutral nitrogen molecules in an electric field-free region. The nitrogen neutrals are accelerated toward the substrate by the pressure gradient within the vacuum chamber. Because the activated nitrogen is not accelerated by electric fields, it arrives at the substrate with lower kinetic energy on the order of 1 eV. This approach allows reaction to form GaN, but prevents film damage associated with high kinetic energy species such as those produced by RF plasma sources [128].

6.2 Growth conditions and structural properties

All the samples discussed in this chapter are supplied from two groups: Professor Sergei Novikov in University of Nottingham, and Dr Stefan P. Svensson, Dr Wendy L. Sarney in the U.S. Army Research Laboratory (ARL).

As described in the previous section, the film stoichiometry is strongly controlled by the elemental vapor beam flux (measured in beam equivalent pressure, BEP). High quality MBE growth GaN is usually grown at 700 - 800 °C. As discussed in Section 3.2, low substrate temperature favors the incorporation of mismatched elements (e.g. Sb in GaN). Shown in Figure 6.2, the Sb content in the resulting thin films decreased with increasing substrate temperature. Both "N-rich" and "Ga-rich" growth regimes are controlled by the Ga flux used. "N-rich" means low Ga flux (BEP at 2.2×10^{-7} torr), and "Ga-rich" means high Ga flux (BEP at 1.6×10^{-7} torr).

Three sets of samples are discussed in this chapter: low temperature high Ga flux, low

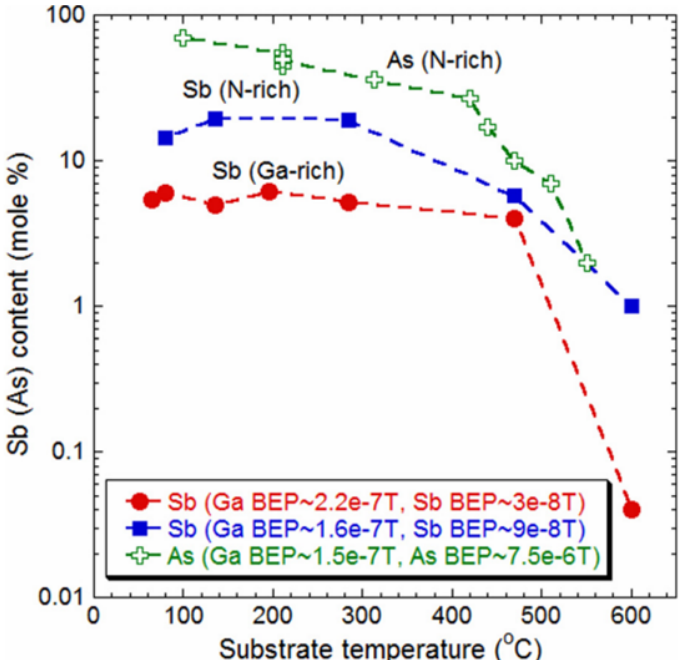

Figure 6.2: Film Sb content with respect to substrate temperature.

temperature low Ga flux, and high temperature medium Ga flux. These three series are chosen because they have distinctive optical, and electrical properties.

Combined effects of Ga flux and Sb flux

Sb incorporation and the overall III-V ([Ga]/[N]+[Sb]) ratio depends strongly on the Ga flux at low growth temperature. The growth temperature for these two sets of samples is 80 °C(lower temperature is chosen based on high Sb incorporation rate. Figure 6.3, shows the film Sb content increases linearly with increasing Sb flux under both N-rich (a) and Ga-rich (b) conditions. The overall III-V ([Ga]/[N]+[Sb]) ratio depends strongly on the Ga flux. Under N-rich growth condition, the III-V ratio decreases monotonically with increasing Sb flux. In order to maintain III-V ratio at 1, the Sb flux needs to be adjusted to compensate the effect. Under Ga-rich growth condition, the III-V ratio stays at 1 until Sb flux reaches above 10^{-7}torr, then the III-V ratio drops below 1 drastically when Sb flux is increased beyond 10^{-7} torr.

Figure 6.4 shows XRD patterns of $GaN_{1-x}Sb_x$ sample grown at different Sb flux under both N-rich (a) and Ga-rich (b) conditions. Films with Sb $>$ 6.2% are entirely amorphous with no observable diffraction peaks. Films with lower Sb content becomes partially crystalline as evidenced by the weak and broad (002) diffraction peak. This diffraction peak is most likely coming from small crystalline grains within the amorphous matrix.

In Figure 6.5(a), both the TEM image and the SAD pattern indicate a polycrystalline film for pure GaN. Both the bright spots and diffused rings co-existed in the SAD of $GaN_{1-x}Sb_x$

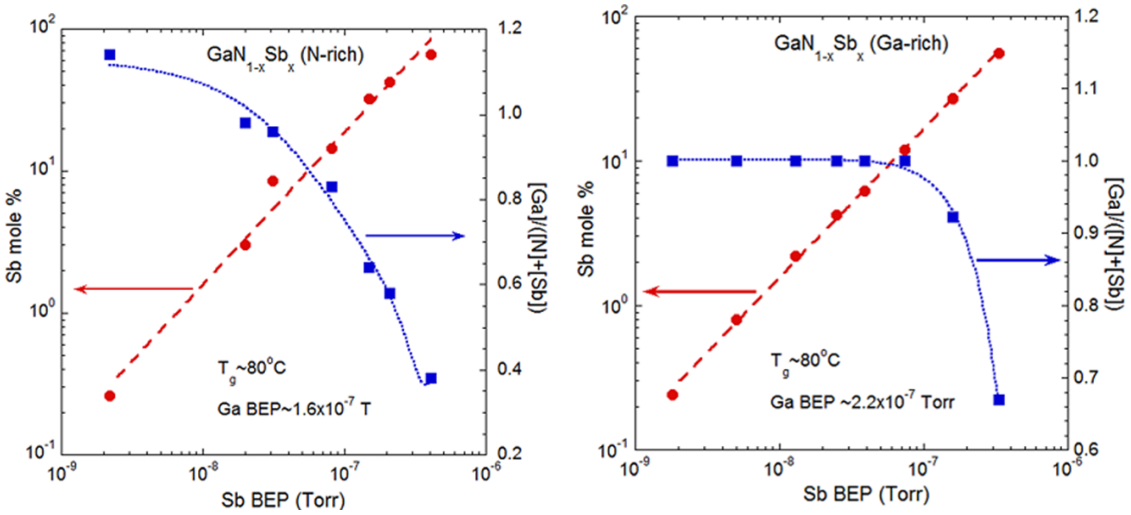

(a) N-rich growth. (b) Ga-rich growth.

Figure 6.3: Film Sb % and III-V ratio under different Ga flux growth regime [128].

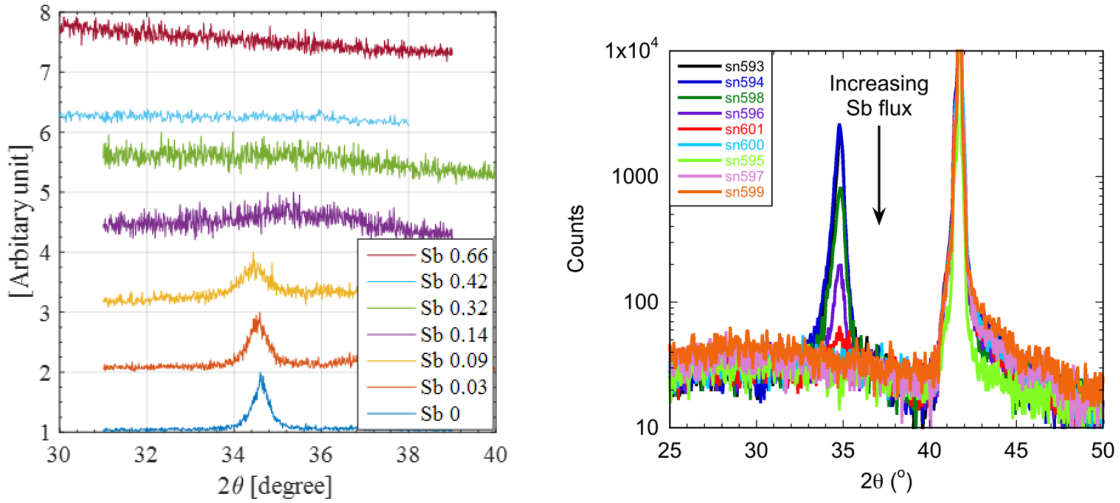

(a) N-rich growth. (b) Ga-rich growth.

Figure 6.4: XRD patterns for $GaN_{1-x}Sb_x$ films under different Ga flux growth regime [128].

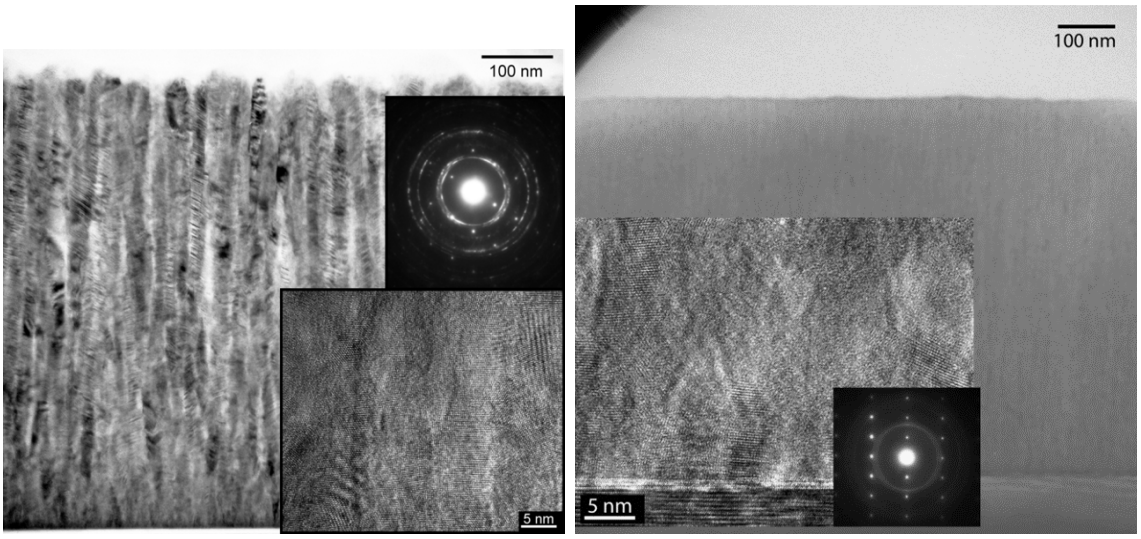

(a) Pure GaN. (b) $GaN_{0.906}Sb_{0.094}$.

Figure 6.5: TEM and SAD patterns for pure GaN, and film with 9.4% Sb.

with x = 0.094 (Figure 6.5, which confirmed that the film is composed of polycrystalline grains as well as an amorphous ring. These results are consistent with the XRD pattern that only a weak (002) GaNSb diffraction peak is observed for samples with x > 0.09.

Both the XRD and TEM characterization showed the crystallinity of the $GaN_{1-x}Sb_x$ thin film decreased with increasing Sb content. However, the film crystallinity does not show strong dependence on N-rich or Ga-rich growth conditions.

6.3 Electronic band structure

X-ray absorption & emission spectroscopies

The XAS and XES experiments are applied to examine the energy positions of the valence and conduction band edges of $GaN_{1-x}Sb_x$. The nitrogen K-edge (400 eV) was investigated under room temperature at beam line 8.0.1 in the ALS of the LBNL. The total fluorescence yield (TFY) detection mode was used for the XAS measurement with the energy resolution of at 0.2 eV. The XES was measured by using the Tennessee/Tulane grating spectrometer with a total energy resolution of 0.6 eV.

Figure 6.6(left) shows the overall XES and XAS spectra for $GaN_{1-x}Sb_x$ samples grown at 80°C, and a reference GaN thin film grown at 800 °C. The XAS threshold energy corresponds to the onset of unoccupied states relative to the nitrogen 1s core-level, whereas the XES threshold energy corresponds to the occupied states. The experimental details and theory are discussed in Section 4.1. In the zoomed-in view of the spectra in 6.6(left), both of the XES and XAS moved inward with increasing Sb%. The onset of the XES edge moved to

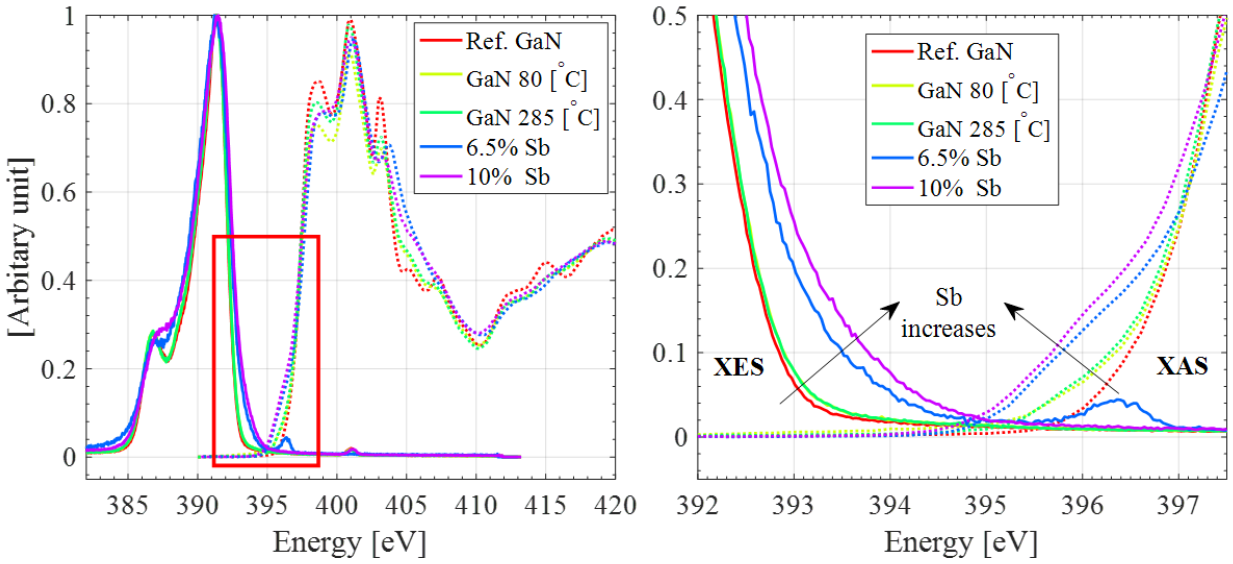

Figure 6.6: (Left) XES and XAS spectra of $GaN_{1-x}Sb_x$, for Sb = 0 to 10%. (Right) Zoomed-in spectra illustrating the CB , VB position change with respect to Sb content.

higher energy (> 1 eV) is consistent under the framework of the HMA that the incorporation of Sb in GaN moves the VB upwards, by forming a fully occupied sub-band above VB of the host matrix band. The onset of the XAS edge moved to a lower energy, due to CBAC interaction between nitrogen localized states and host CB states.

Optical absorption and band-anticrossing theory

The optical E_{gap} of $GaN_{1-x}Sb_x$ in this work is determined by measuring the optical absorption coefficient. Figure 6.7 illustrates the measured absorption spectra of seven $GaN_{1-x}Sb_x$ thin films samples with compositions ranging from Sb = 0 to 42 %. A monotonic red-shift is observed with increasing Sb%. Similar to the analysis of $ZnO_{1-x}Te_x$, the BAC theory is applied to systematically study the band structure $GaN_{1-x}Sb_x$ alloy across the whole composition range. The detailed mathematical formulation can be found in Section 4.4. In the case of $GaN_{1-x}Sb_x$, the E_{Sb}, E_N, the band edges, effective masses for both GaN, and GaSb are used.

Figure 6.8(a) shows the calculated dispersion relation of the electronic band structure of $GaN_{1-x}Sb_x$ at Sb = 18%. The development of the Sb-derived E_V^+ band above the host VB is responsible for the drastic E_{gap} reduction at the N-rich composition range.

Figure 6.8(b) shows the calculated absorption coefficient for all the possible optical couplings within the perturbed electronic band structure of $GaN_{1-x}Sb_x$, with the dashed line shown as the total absorption coefficient. Figure 6.9 shows the fitting of absorption spectra for a series of samples ranging from Sb = 0 to 42%.

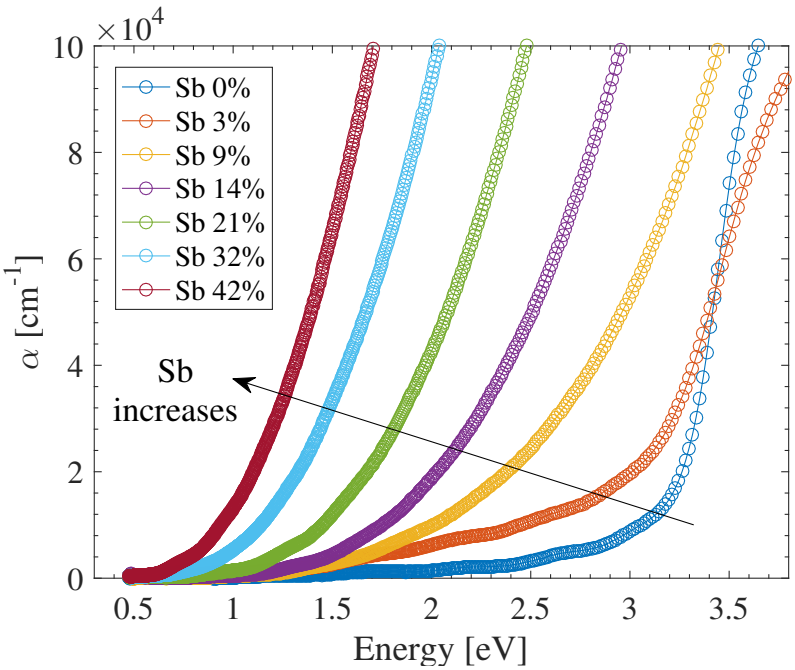

Figure 6.7: Optical absorption of $GaN_{1-x}Sb_x$ with Sb = 0 to 42 %.

It is worth noticing that, the absorption spectra of the pure GaN film lacks a sharp onset. Instead, a weak absorption tail beginning at roughly 1 eV is observed.

We speculate that the weak absorption tail is associated with the Ga-antisite defects, which are observed in the GaN thin films grown by low temperature MBE under Ga-rich growth regime [127]. Similar absorption tail is observed in the low temperature grown Ga-rich GaN.

By fitting the absorption coefficient with the BAC model, the VBAC parameters for $GaN_{1-x}Sb_x$ are determined as: E_{Sb} at 1.2 eV above VBM of GaN, $C_{Sb0} = 2.5$ eV, and the band broadening ranging from 0.01 - 0.5 eV. Combing the VBAC parameters obtained in this work with the CBAC parameters [128]: E_N at 0.45 eV above CBM of GaSb, $C_{N0} = 2.7$ eV, the CB and VB edges for the $GaN_{1-x}Sb_x$ alloy are determined across the whole composition range (shown in Figure 6.10(a)). The green and blue solid curves represent the calculated VBM and CBM respectively. The drastic upward shift of VB caused by the Sb-derived band at the N-rich composition is evidenced by the XES experiments discussed in Section 6.3, which are shown as the green hollow circle in Figure 6.10(a). The E_{gap} energy of $GaN_{1-x}Sb_x$ across the whole composition range is shown in Figure 6.10(b). The blue solid square, and orange hollow diamond are data points obtained from BAC fitting of the optical absorption coefficient in this work. The red solid circles are the data points obtained from the XES / XAS experiments.

The experimentally determined E_{gap} is larger than the BAC prediction among the middle composition range $0.2 < x < 0.8$. It should be noted that the reported Sb% is the total

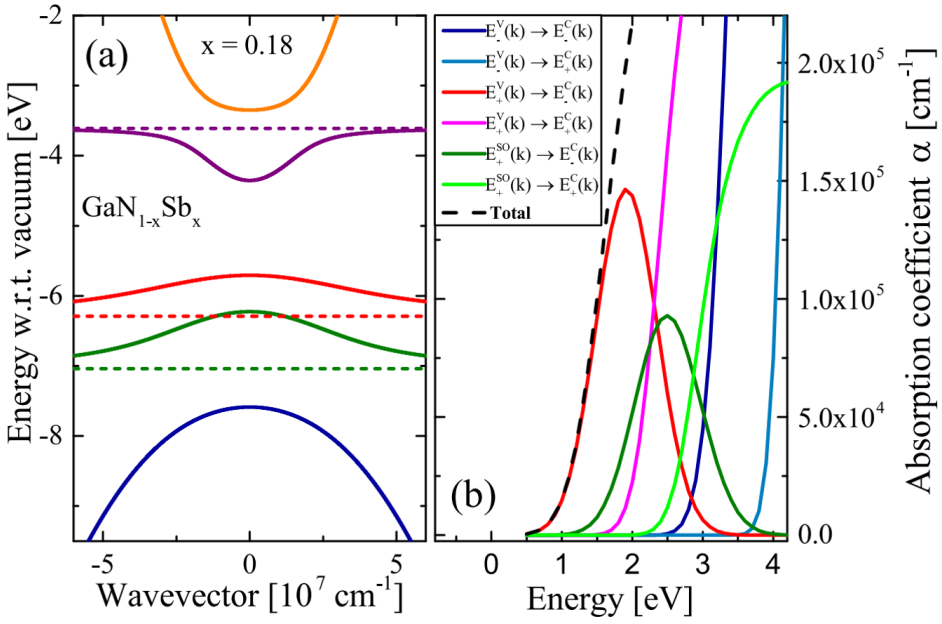

Figure 6.8: (a). Calculated dispersion relation of $GaN_{1-x}Sb_x$ at Sb = 18%. (b). Calculated JDOS of all possible optical couplings for Sb = 18%, and the total absorption coefficient is shown as the black dashed-line.

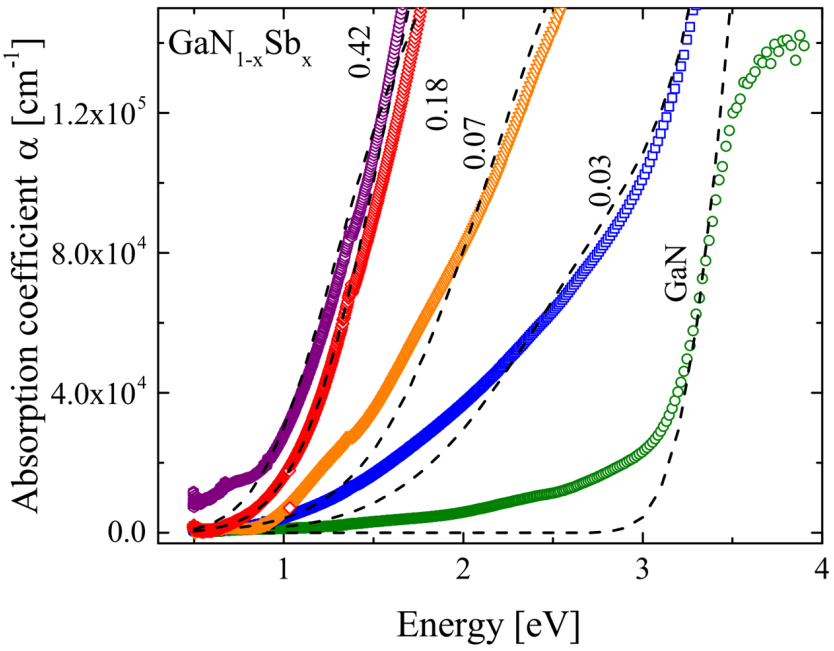

Figure 6.9: The fitting of the measured optical absorption spectra α of $GaN_{1-x}Sb_x$ with respect to the BAC calculation (black dashed-line).

Sb content in the sample determined by RBS. On the other hand, the BAC calculated E_{gap} assumed 100% subsitutional Sb in the alloy. In reality, due the mismatched nature of Sb in GaN, the substitutional fraction is unlikely to be 100%. Unfortunately as shown in section 6.2, the substitutional fraction of Sb could not be determined from XRD due to the amorphous nature the thin film at Sb > 9%. Since the experimentally determined E_{gap} is larger than the BAC prediction at Sb > 20%, we speculate that there is a gradual decrease in the solubility of Sb in GaN.

6.4 Summary

Polycrystalline $GaN_{1-x}Sb_x$ thin films are synthesized by low temperature MBE in the alloy composition range of x = 0 to 0.56. The band structure of $GaN_{1-x}Sb_x$ alloy is determined by the modeling of the optical absorption coefficient across the entire composition range, which shows good agreement with the band edge positions determined by the XAS, XES x-ray spectroscopies. Adding Sb in GaN causes a more drastic E_{gap} reduction comparing that in $ZnO_{1-x}Te_x$. As shown in Figure 6.10(b), an 1.8 eV E_{gap} can be achieved with $GaN_{0.93}Sb_{0.07}$, whereas 23% Te is needed in $ZnO_{1-x}Te_x$ to achieve the 1.8 eV E_{gap}.

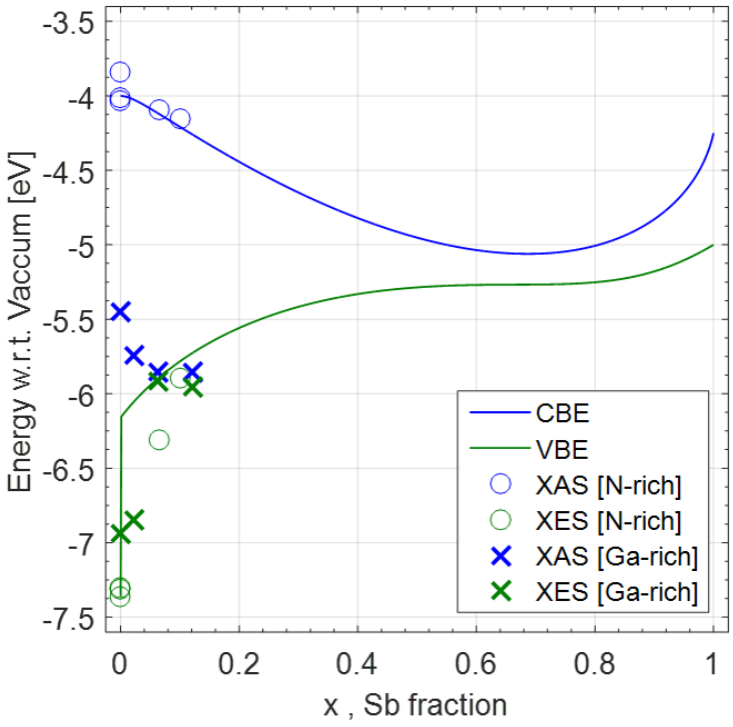

(a)

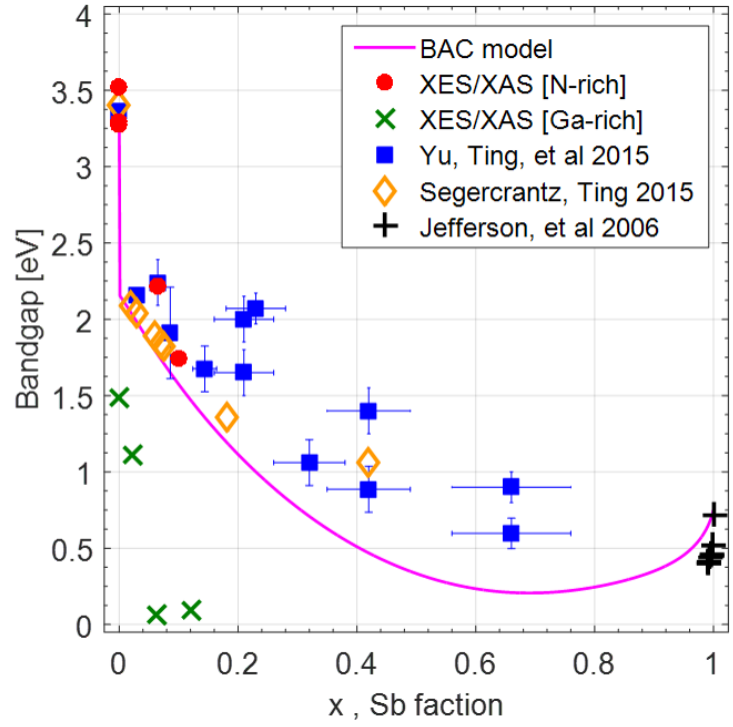

(b)

Figure 6.10: (a) CBM, VBM and (b) E_{gap} of the $GaN_{1-x}Sb_x$ alloy across the whole composition range.

Chapter 7

$GaN_{1-x}Sb_x$ electrical properties

As shown in Chapter 4, $ZnO_{1-x}Te_x$ suffered from a low CBM position, that P-type conductivity still challenging to obtain in this material. GaN has a similar E_{gap} to ZnO, but its CBM and VBM are 0.6 eV higher. Undoped GaN also prefers to be N-type conductive [26], because its CBM is still relative low in with respect to vacuum energy level. $GaN_{1-x}Sb_x$ (x = 0 to 0.56) studied in this work is N-type conductive for $x < 0.06$, and is P-type conductive for $0.06 \leq x \leq 0.56$. The P-type conductivity increases with increasing Sb%. Section 7.1 discusses the Sb% dependent electrical properties of the as-grown $GaN_{1-x}Sb_x$ and the annealing effects on its electrical properties. Section 7.2 describes the modeling of the hole concentration with the BAC model. Section 7.3 discusses the Seebeck coefficient and its potential advantage in the thermoelectric application. Lastly, Section 7.4 discusses the application of $GaN_{1-x}Sb_x$ as an enhancement material for the P-type ohmic contact in GaN device.

7.1 Electrical properties of as-grown and annealed $GaN_{1-x}Sb_x$

As-grown samples

In the samples studied in this work, $GaN_{1-x}Sb_x$ with Sb < 6% is N-type conductive. As shown in Figure 7.1(left), negative Seebeck coefficient is only observed for sample with 2% Sb, and positive Seebeck coefficient is observed for samples with larger Sb content. As shown in Figure 7.1(right), the P-type conductivity increases with increasing Sb content.

Annealed samples

After annealing, the electrical conductivity of $GaN_{1-x}Sb_x$ shows significant improvement over two orders of magnitudes. As shown in Figure 7.2(b), the conductivity of all the P-type samples has increased with annealing temperature with a significant increase in hole

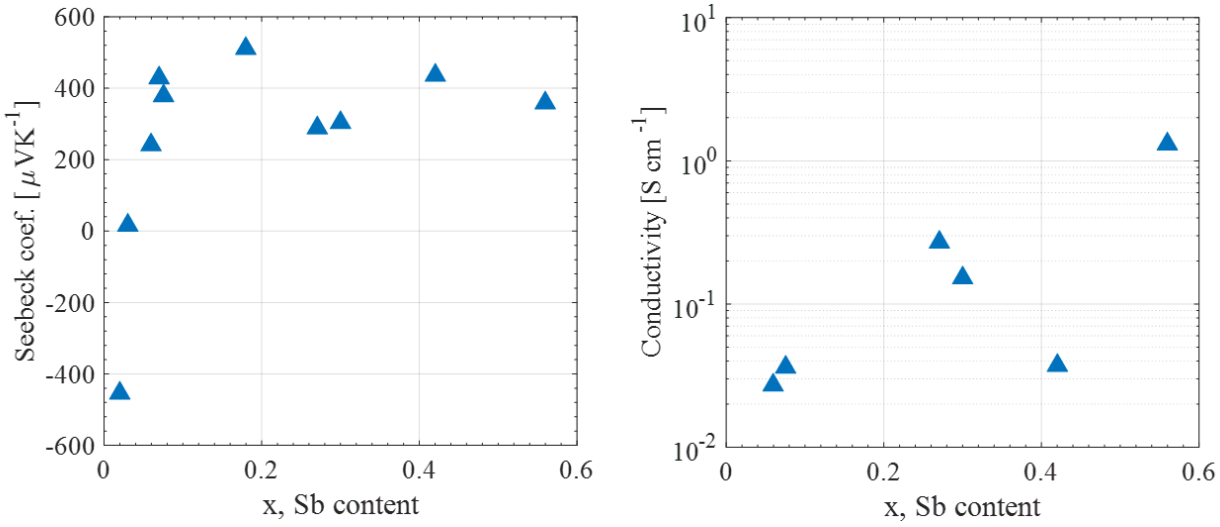

Figure 7.1: (Left) Seebeck coefficient and (right) electrical conductivity of as-grown $GaN_{1-x}Sb_x$ thin films for x = 0.02 to 0.56.

concentration (Figure 7.2(c)). The change of hole mobility upon annealing is not clear (Figure 7.2(d)).

The change in crystal structure upon annealing are shown in the XRD patterns in Figure 7.3(a)-(e). The formation of GaSb [210] phase is observed upon annealing. And the GaSb [210] peak intensity increases with annealing temperature. GaSb is a strongly P-type semiconductor with a small E_{gap} of 0.7 eV [91]. Since the sample with 6% Sb (without GaSb phase in XRD pattern) already show strong P-type conductivity, the dominate contribution of the P-type conductivity should be within the amorphous $GaN_{1-x}Sb_x$ network. However in samples with high Sb content, the contribution from the highly P-type GaSb crystalites embedded in the amorphous network cannot be ruled out.

Figure 7.4(a)-(d) shows the electrical properties of $GaN_{1-x}Sb_x$ with respect to Sb content for both as-grown and RTA 650°C samples. The hole concentration of the alloy decreases monotonically over one order of magnitude with Sb content increases from 6 % to 56 %. In the same alloy range, the hole mobility increases monotonically over two orders of magnitude resulting in an increase in overall P-type conductivity for one order of magnitude.

As predicted by the BAC model, as Sb % increases, the hole effectivemass of the Sb-derived valence band decreases (Figure 6.8), which contributes to the increase in hole mobility in this alloy.

Defect contribution to the P-type conductivity

The V_{Ga} acceptor-like defect has been regarded as the origin of native P-type conductivity in different undoped Ga-V binary semiconductors [90][12]. Relatively low growth temperature and nitrogen-rich growth would favor the formation of V_{Ga} [10]. Thus, V_{Ga} are also likely

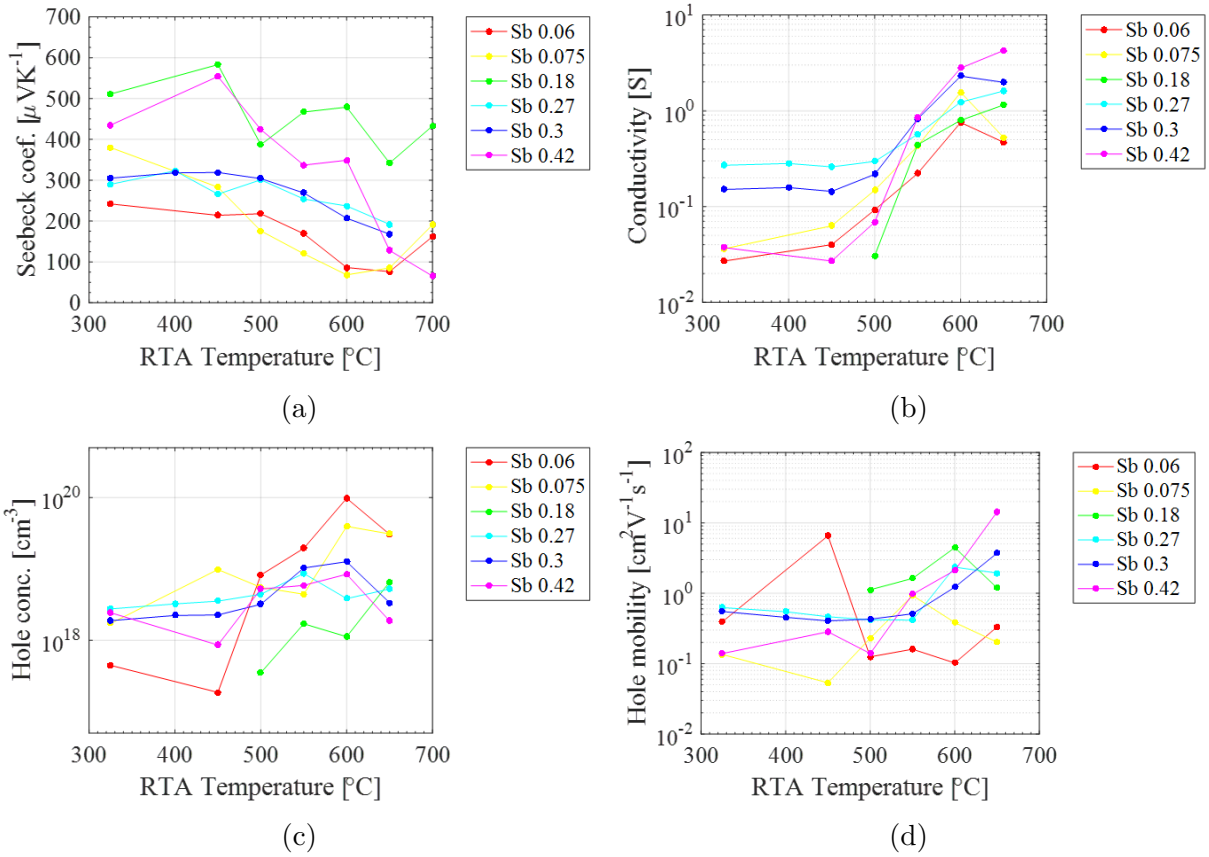

Figure 7.2: Electrical properties of $GaN_{1-x}Sb_x$ with increasing RTA temeperature: (a) Seebeck coefficient, (b) conductivity, (c) hole concentration, and (d) hole mobility.

to be the dominate source of the native P-type conductivity in $GaN_{1-x}Sb_x$ in this work. In GaN, V_{Ga} has a defect energy level much higher than its VBM [12]. The V_{Ga} acceptor-level is located very deep within the band gap of GaN, at 1 eV above GaN VBM. As shown in Chapter 6, alloying with heavier elements Sb in GaN pushes the VBM of the host upward. The Sb derived E_V^+ band is expected to be located at > 1.2 eV above GaN VBM, it would be energetically favorable to activate the V_{Ga} defects to increase the overall P-type conductivity.

Annealing effect

The N_{Ga} antisites donor-like defects are expected to be dominate source of the N-type conductivity in the low Sb% samples. Upon annealing, the N_{Ga} antisites are removed accompanied with the formation of acceptor-like defects V_{Ga} [10].

$$2N_{Ga} \rightarrow 2V_{Ga} + N_2 \tag{7.1}$$

Therefore, both mechanisms contributed to the overall increase in P-type conductivity:

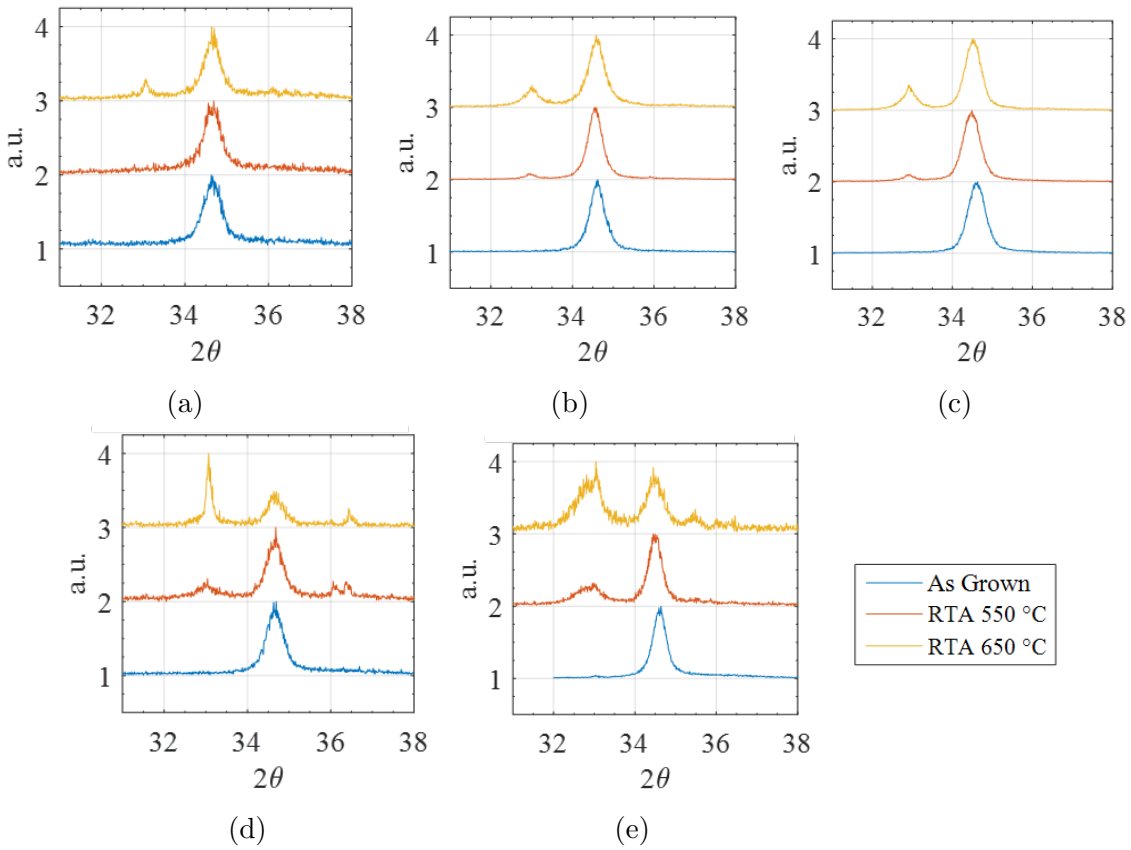

Figure 7.3: The XRD diffraction patterns for as-grown, RTA 500 °C, and RTA 650 °C for $GaN_{1-x}Sb_x$ samples with Sb = (a) 18% (b) 27% (c) 30% (d) 42% (e) 56%.

1). the activation of V_{Ga} and 2). the reduction of acceptor compensation by removing N_{Ga} donor-like defects upon annealing. Since the removal of N_{Ga} accompanied with the formation of V_{Ga}, the overall amount of ionized impurities stayed constant. Thus the carrier mobility does not show significant change. Similar effect is observed in low temperature grown GaAs:Be [10]: that under low temperature growth of GaAs, there is a high concentration of As_{Ga} native donor-like defects, and after annealing the formation of V_{Ga} diffuses to remove the As_{Ga} into As precipitates.

Dependence on Sb%

For samples with less than Sb <20%, a large increase in hole concentration is observed upon annealing (as-grown: 1×10^{18} cm^{-3}; RTA at 650°C: 2×10^{19} cm^{-3}). For samples with Sb > 30%, there is no obvious change in the hole concentration upon annealing. As suggested in the previous section, increase Sb% and annealing are expected to increase the hole concentration by activating V_{Ga} and the removal of N_{Ga}. The unchanged hole concentration for samples with Sb > 30% could be due to the improvement of sample crystallinity upon

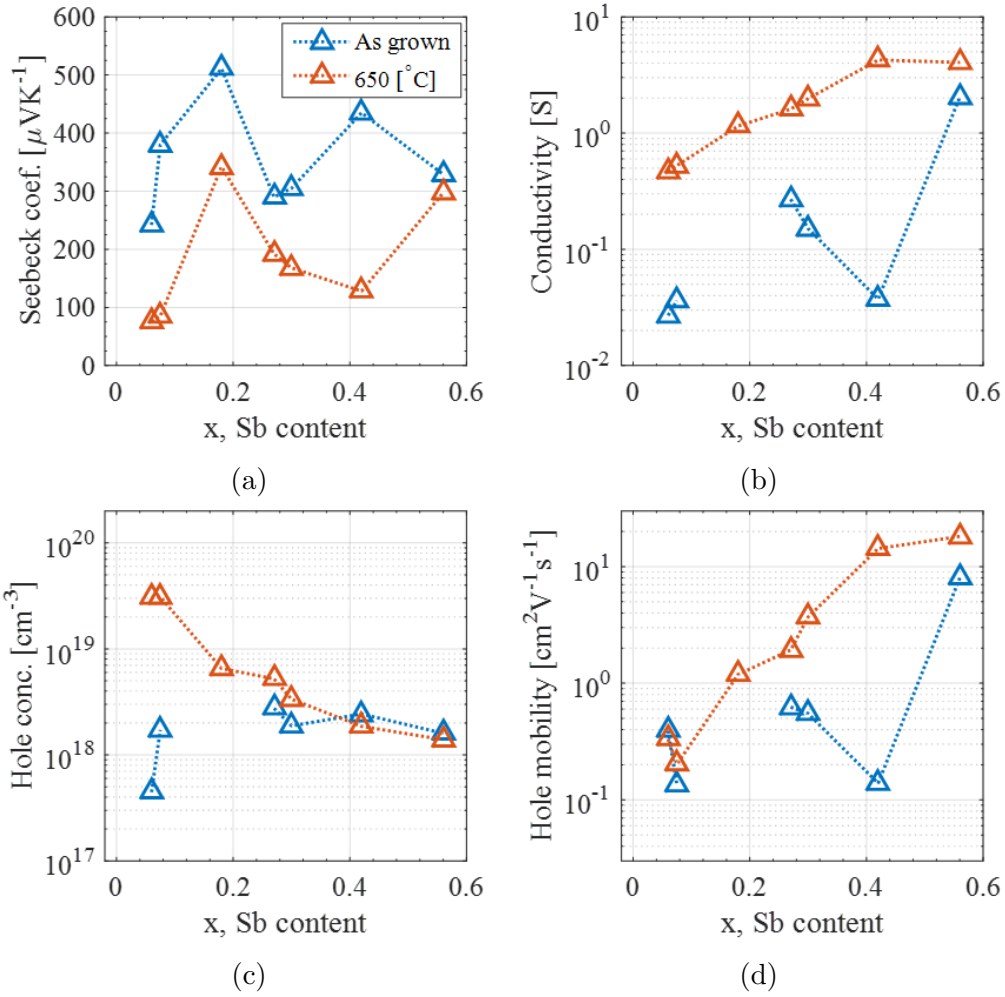

Figure 7.4: Electrical properties comparison of $GaN_{1-x}Sb_x$ with respect to Sb% between as-grown and RTA 650°C series: (a) Seebeck coefficient, (b) conductivity, (c) hole concentration, and (d) hole mobility.

annealing. As shown in Figure 7.3, more pronounced GaSb [210] phase is observed upon annealing for samples with high Sb%. Hence, the crystallinity improvement reduced the overall defect concentration, and resulted in the unchanged hole concentration upon annealing for $GaN_{1-x}Sb_x$ samples with Sb >30%.

7.2 BAC modeling of hole concentration

A thorough treatment of the perturbed DOS of $GaN_{1-x}As_x$ HMA was first introduced by Wu et al in [120]. It included the interaction of the localized and extended states in the Hamiltonian under the many-impurity Anderson formulation. The model was originally developed to describe the $s \cdot d$ hybridization between the localized magnetic impurity states and delocalized metallic element states [6]. In the framework of HMAs, such treatment provides a richer description the hybridization between the localized impurity states and extended host states. The following paragraphs summarize the major results of this model to provide the background for further modeling of the hole concentration in $GaN_{1-x}Sb_x$ at different Sb composition.

In pure semiconductors, the DOS is proportional to the square root of energy, at energy close to the band edges. The DOS of the CB per unit cell and energy unit follows equation:

$$\rho_0(E) = \frac{4\pi\sqrt{E - E_0^C}}{\epsilon_B^{3/2}} \tag{7.2}$$

where $\epsilon_B = \frac{\hbar^2}{2m_e^*}\left(\frac{2\pi}{b}\right)^2$, b is the lattice parameter and m_B^* is the electron effective mass.

Perturbation theory is applied to the HMAs by solving the Schrödinger equation using the Anderson Hamiltonian [6]. The Schrödinger equation is then solved by applying Green's function [24]. The Coherent potential approximation (CPA) is used to quantify the perturbation as a random distribution of isovalent impurities (e.g. Sb in GaN) [108]. The perturbation potential $V_{perturb}$ in system is linked to the fraction of impurities:

$$V_{perturb} = C\sqrt{x} \tag{7.3}$$

where C is the coupling constant described in Chapter 2.2 Equation 2.2. The approximated Green's function is:

$$G_{kk}(E) = \frac{E - (E^d + i\pi\beta V^2\rho_0(E^d))}{(E - E_k^C)(E - (E^d + i\pi\beta V^2\rho_0(E^d))) - V^2x} \tag{7.4}$$

where ρ_0 is the unperturbed DOS, and V is the perturbation potential. Finally, solving the poles of the Green's function, the solutions are given by an equivalent two-state-like eigen-value problem.

$$\begin{vmatrix} E_k^c - E(k) & C\sqrt{x} \\ C\sqrt{x} & E^d + i\Gamma_d - E(k) \end{vmatrix} = 0 \tag{7.5}$$

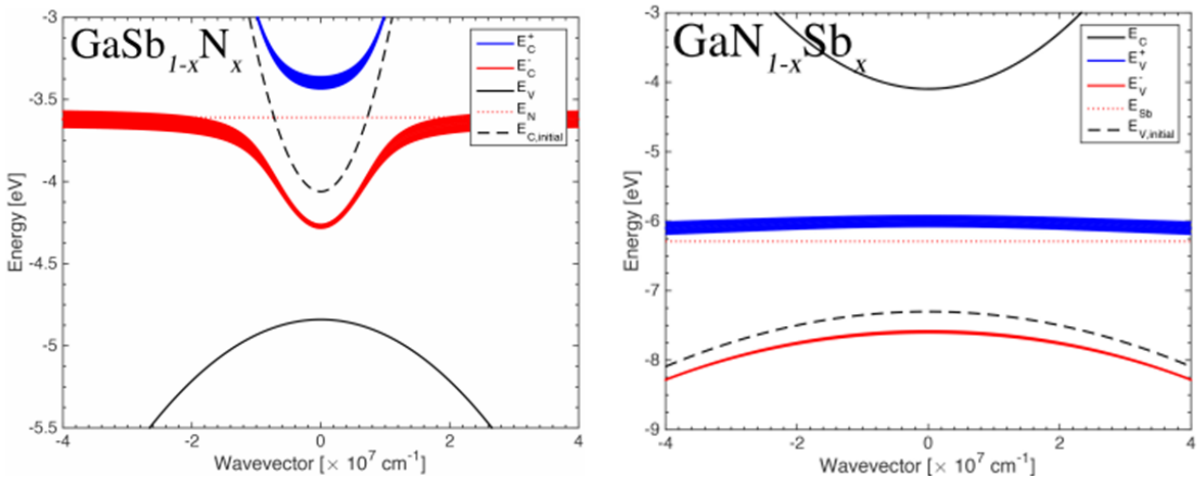

(a) CBAC in $GaN_{0.02}Sb_{0.98}$. (b) VBAC in $GaN_{0.98}Sb_{0.02}$.

Figure 7.5: Band structure of $GaN_{1-x}Sb_x$ alloys in (a) Sb-rich, and (b) N-rich composition regimes.

where $\Gamma_d = \pi\beta V^2\rho_0(E^d)$ is the broadening of the E^d in the single-impurity Anderson model. If $\Gamma_d = 0$, 7.5 is reduced to the BAC model for equation 2.2 with two restructured dispersions for the upper and lower conduction subbands. If the broadening Γ_d is nonzero but small, so that $C\sqrt{x} >> \Gamma_d$ and $(E_d^C - E^d) >> \Gamma_d$, an approximated analytical solution is obtained:

$$\widetilde{E}_{\pm}(k) \approx E_{\pm}(k) + i\Gamma_d \frac{E_{\pm}(k) - E_k^C}{[E_{\pm}(k) - E)k^C] + [E_{\pm}(k) - E^d]} \equiv E_{\pm}(k) + i\Gamma_{\pm}(k) \tag{7.6}$$

The state broadening within the band splitting is important for HMAs. Indeed the absence of broadening would result in an unphysical infinite DOS at the defect level. As the expression of the Green's function is obtained, the density of states of free electrons can be calculated from the imaginary part of the Green's function [24].

Finally, equation 7.7 shows the dispersion relations are similar to the ones obtained with the intuitive two-level system, with the exception that an imaginary broadening term is now included, see Figure 7.5.

$$E_{\pm}(k) = \frac{1}{2}\left(E_k^C \pm + E^d\sqrt{(E_k^C - E^d)^2 + 4C^2x}\right) + i\Gamma_L \frac{E_{\pm}(k) - E_k^C}{(E_{\pm}(k) - E_k^C) + (E_{\pm}(k) - E^d)} \tag{7.7}$$

As the expression of the Green's function is obtained, the density of sates of free electrons can be calculated from the imaginary part of the Green's function [24],

$$\rho(E) = \frac{1}{\pi}\Im\sum_k G_{kk}(E) = \int \rho_0(E_k^C)\Im[G_k k(E)]dE_k^C \tag{7.8}$$

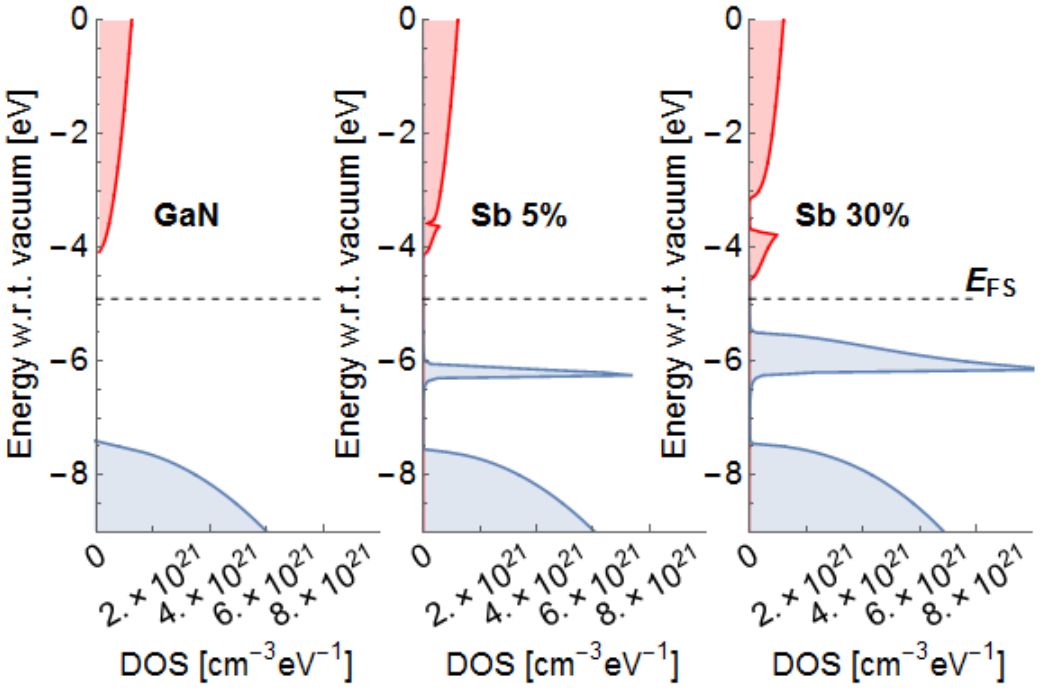

Figure 7.6: Perturbed DOS for both CB and VB of $GaN_{1-x}Sb_x$ alloys with x = 0, 0.05, and 0.3.

The calculated perturbed DOS for $GaN_{1-x}Sb_x$ with x = 0, 0.05, and 0.30 are shown in Figure 7.6. The anticrossing interaction leads to dramatic redistribution of the electronic states in both VB and CB. In the N-rich composition regime (i.e. Sb < 50%) the VBAC is the dominant effect. In Figure 7.6, the DOS in Sb-derived E_V^+ band increases as increasing Sb%. In addition, the development of the Sb-dervied band causes a drastic upward shift of VB which is further shifted upward upon increasing Sb%.

To calculate the carrier concentrations of $GaN_{1-x}Sb_x$, the DOS is integrated with the Fermi-distribution w.r.t. energy,

$$P(E_F, x, \Delta_V, T) = \int \rho_V(E, x, \Delta_V) \cdot \left(1 - \frac{1}{1 + \exp\left(\frac{E-E_F}{kT}\right)}\right) dE \tag{7.9}$$

Figure 7.7 shows both the hole and electron concentration calculated for the case of Sb = 0%, 5%, 30%, and 50% with respect to Fermi-level. In the Arrhenius plots, there are two distinctive regimes: non-degenerate (linear), and degenerate (non-linear). The two regimes are transitioned smoothly for conventional semiconductor, e.g. the curves for GaN. For $GaN_{1-x}Sb_x$ (Sb >0%), there is an abrupt plateau regime connecting the degenerate, and non-degenerate regimes. E.g. Sb = 5%, a plateau is observed in the range of -6 to -7.6 eV (-3 to -4.2 eV) in the VB (CB). The BAC interaction causes a splitting in the VB between

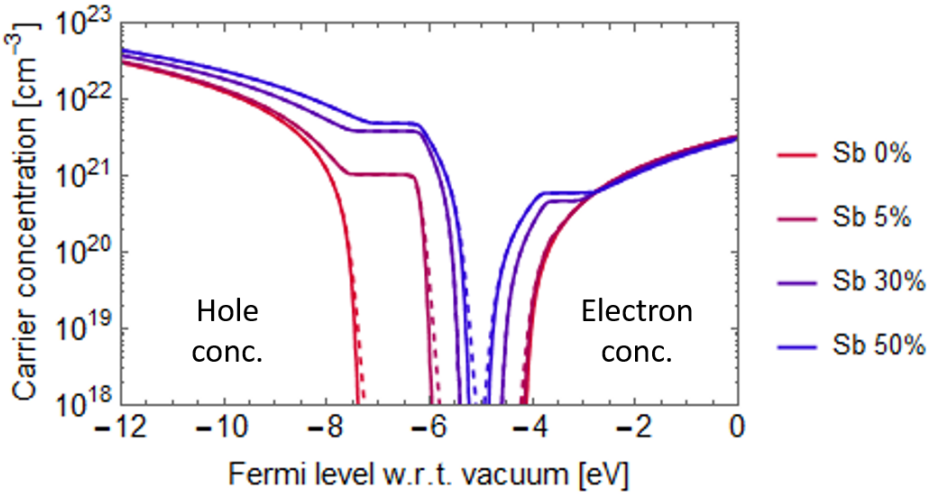

Figure 7.7: Carrier concentration of $GaN_{1-x}Sb_x$ with Sb = 0%, 5%, 30%, and 50% with respect to E_F position at T = 300 °C (solid line), and 600 °C (dash line).

the Sb-derived E_V^+, and modified host E_V^- (shown in Figure 7.5). Hence there is a gap with no states between the E_V^+, and the E_V^- bands. Similar behavior is observed in the CB.

To assess the tendency of conductivity type for $GaN_{1-x}Sb_x$, the hole and electron concentration are calculated at different Sb% assuming the E_F is pinned at E_{FS} for T = 300 °C, and 600 °C. The calculation result is shown in Figure 7.8. At x = 0, with E_F at E_{FS}, the hole concentration is negligible, thus the pure GaN has higher tendency to be N-type conductive. At x > 0, the VB has been pushed upward drastically, and thus making $GaN_{1-x}Sb_x$ has a higher tendency to be P-type conductive. As shown in Figure 7.8, the hole concentration at 600 °C is slightly lower than the electron concentration at 600 °C but much higher than the electron concentration at 300 °C. And the hole and electron concentration (600 °C) will cross at x = 0.7. In addition, the hole concentration increased drastically (over 4 orders of magnitude as temperature increased from 300 °C to 600 °C). At 600 °C the Fermi-distribution is more smeared out, thus both electron and hole concentration should be increased. In $GaN_{1-x}Sb_x$, due to the steep slope in DOS at the Sb-derived E_V^+ band edge, the hole concentration is increased more drastically than the increase in electron concentration upon temperature increase.

Figure 7.9 shows the hole concentration measured by Hall effect, and the calculated hole concentration at $E_F = E_V^+$, $E_V^+ + 50$meV, and $E_V^+ + 100$ meV with respect to Sb%. In general, the annealed samples have higher hole concentration, thus with E_F closer to the Sb-derive band edge. The as-grown samples have a relatively lower hole concentration, thus the E_F about 50 meV away from the Sb-derived band.

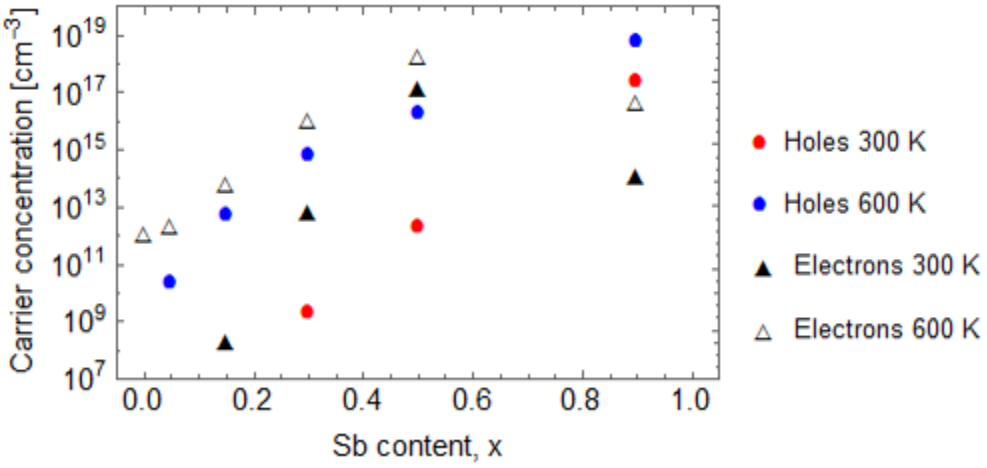

Figure 7.8: The electron and hole concentration calculated at $E_F = E_{FS}$ at x = 0, 0.15, 0.3, 0,5, and 0.9 for 300 °C and 600 °C.

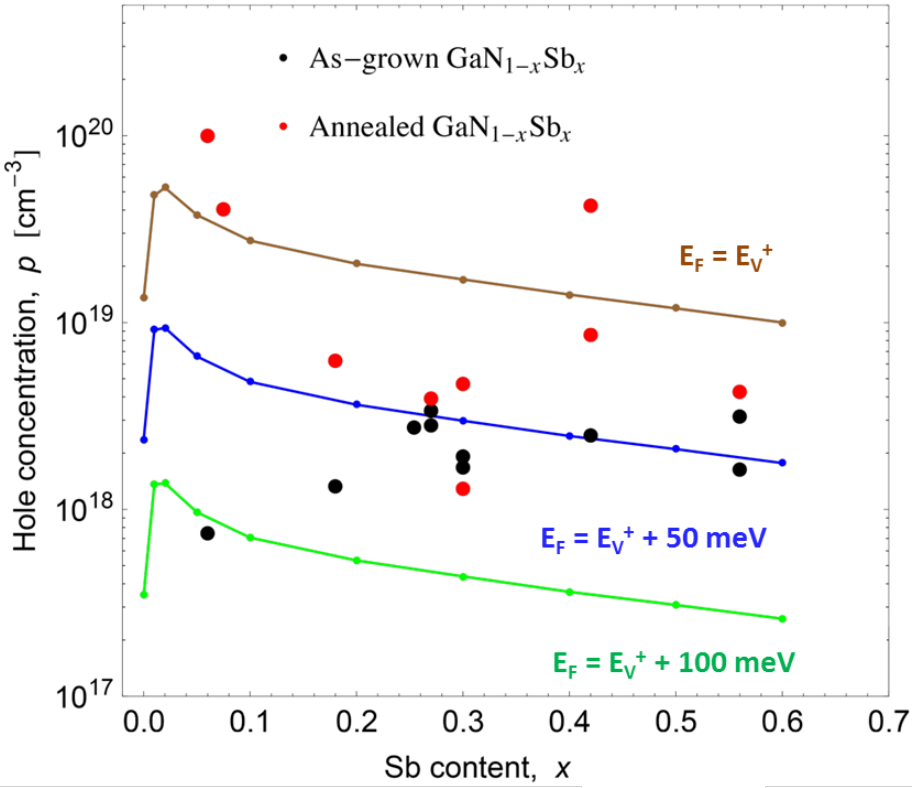

Figure 7.9: The hole concentration measured by Hall effect, and the calculated hole concentration at $E_F = E_V^+$, $E_V^+ + 50$meV, and $E_V^+ + 100$ meV at different Sb composition.

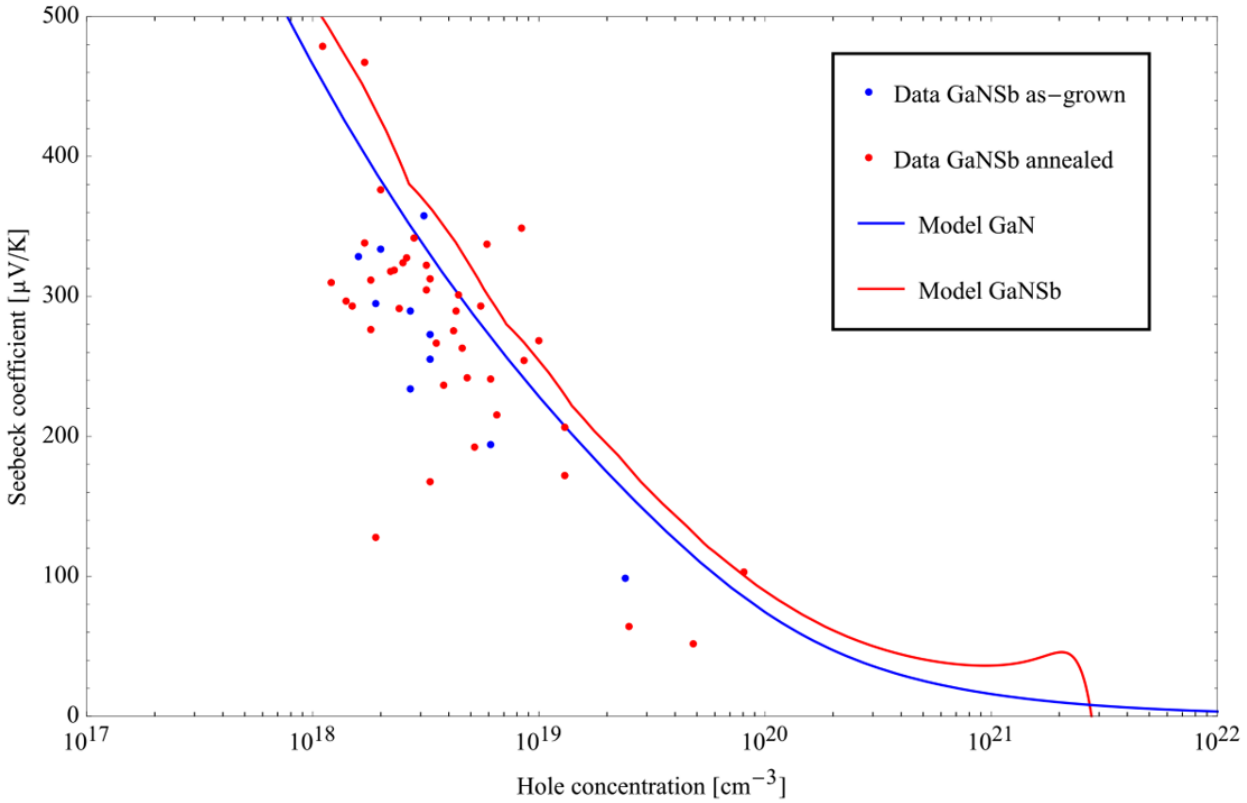

Figure 7.10: Comparison of Seebeck coefficient between BAC model calculation and experimental data for $GaN_{0.44}Sb_{0.56}$ with respect to hole concentration.

7.3 Seebeck coefficient and thermoelectric application

The calculation of the Seebeck coefficient follows the conventional formulation discussed in Section 5.2. Figure 7.10 shows the calculated Seebeck coefficient with experimental data for $GaN_{1-x}Sb_x$ with x = 0.56. The red curve represent the calculated value with BAC model, and the blue curve represents the value with GaN effectivemass model. For both cases, the scattering factor $\gamma = -\frac{1}{2}$ fits best to the experimental dataset, which indicates that the phonon scattering is the dominate carrier transport scattering mechanism in the $GaN_{0.44}Sb_{0.56}$ thin film alloy. Since the alloy material is highly defective (given the amorphous nature), it is likely that it has high compensation ratio. Hall effect measures the net carrier concentration, so it could underestimated the total carrier concentration in a highly compensated material, which is likely the case in our $GaN_{1-x}Sb_x$. Similar to the case of $ZnO_{1-x}Te_x$ discussed in Section 5.2, it is more likely that the impurity scattering is the dominate scattering mechanism in this alloy material.

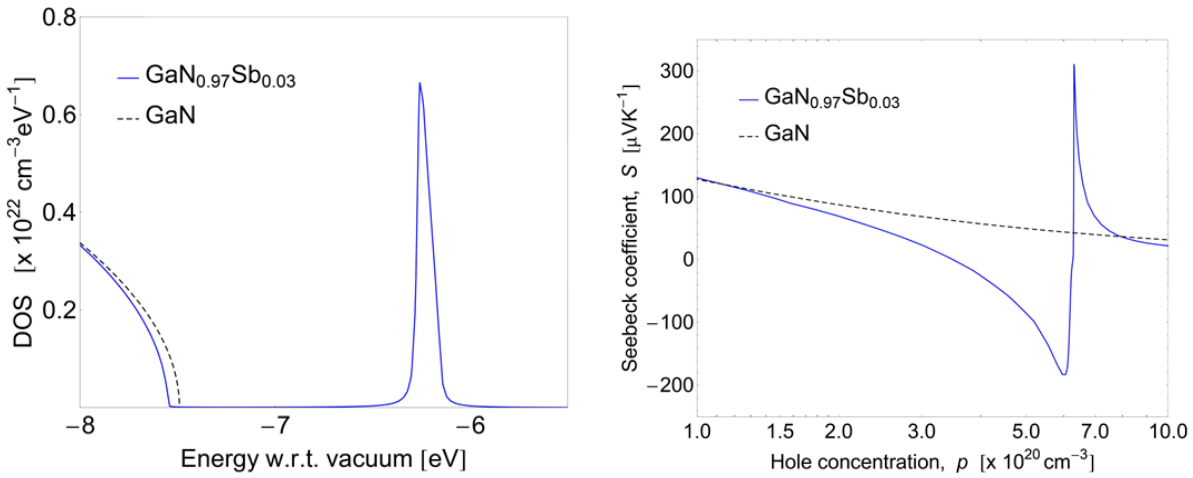

(a) DOS.

(b) Seebeck coefficient.

Figure 7.11: Calculated DOS and Seebeck Coefficient of $GaN_{1-x}Sb_x$ with Sb = 3%.

Thermoelectric application

Due to the non-parabolic dispersion relation and DOS, the thermopower of this alloy has an interesting behavior that there could potentially yield a material a large Seebeck coefficient with high carrier concentration, which is the major obstacle in thermoelectric technology. For conventional semiconductor, high Seebeck coefficient and high carrier concentration can not be achieved at the same time, because Seebeck coefficient is proportional to the $\frac{\partial DOS}{\partial E}$. The $\frac{\partial DOS}{\partial E}$ is largest at the band edges, but the carrier concentration is low when the E_F is near the band edges. The $\frac{\partial DOS}{\partial E}$ decreases when the E_F moves further into the band for degenerated doped semiconductor. Such fundamental dilemma has limited the overall efficiency of themoelectric materials. The abrupt changes in the DOS of $GaN_{1-x}Sb_x$ has the potential to break this fundamental dilemma. This idea was first proposed by Wu et al [59]. In Figure 7.11(b) shows that when the Fermi-level is at the Sb-level, hole concentration is high (7×10^{20} cm^{-3}) due to the DOS within the Sb-derive band. At the same time a large negative Seebeck coefficient is resulted from the steep downward slope of the DOS near the Sb-level.

7.4 Enhanced P-type ohmic contact in GaN-based light emitting diodes

The strong P-type conductivity of $GaN_{1-x}Sb_x$ in addition to the PV applications, the material can also help improving the ohmic contact in the P-type layer of the GaN devices.

GaN is a well-studied material for the application in blue light LEDs. For a semiconductor to be used in optoelectronic devices, besides good semiconductor quality, good ohmic contacts

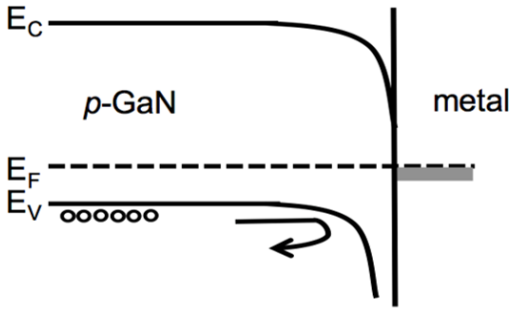

(a) p-GaN contact surface band bending.

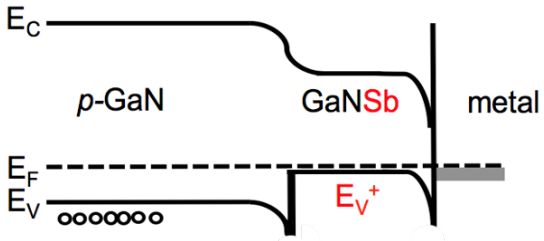

(b) Ohmic contact with $GaN_{1-x}Sb_x$ buffer layer.

Figure 7.12: Band diagram of contact barrier of (a) a typical P-type GaN, (b) using P-type $GaN_{1-x}Sb_x$ as a buffer layer to reduce the potential barrier height and width to provide a better ohmic contact to P-type GaN.

are also necessary to ensure efficient charge extraction.

As shown in Figure 2.1, GaN has a relatively low VB, and CB closer to the E_{FS}. Therefore undoped GaN tends to be N-type conductive natively, and the P-type doping in GaN is still not as efficient. Amano *et al.* [4] showed that the Mg-doped GaN layers grown by MOCVD became P-type conductive only after a low-energy electron beam irradiation (LEEBI). Later Nakamura *et al.* [78] obtained P-type GaN by thermal annealing of Mg-doped GaN at 700 °Cunder N_2-ambient. To date, the highest reported values on the hole concentration Mg-doped GaN are low 10^{18} cm^{-3} with corresponding resistivity of 0.5 Ω·cm [45].

The saturation in hole concentration in P-GaN has been attributed to an interplay between the high ionization energy of Mg dopants and self-compensation by native defects. Because of the high ionization energy, only a fraction of the introduced Mg atoms substitutes Ga and are activated as acceptors [107]. The residual Mg atoms stay typically in the form of precipitates, complexes, or structural defects [109].

Because of the absence of highly P-type P++ layer, good ohmic contact to P-GaN remains challenging. Typically metals with high workfunctions are necessary to decrease the contact potential barrier. However, given the low VB (-7.6 eV in absolute scale) of GaN, a metal with such high workfunction is unavailable. Therefore a tunnel junction is the only viable way of create a good ohmic contact to P-GaN. A tunnel junction requires a thin layer of doped P++ layer in order for the free holes to tunnel through the thinner potential barrier. With Mg doping, the potential barrier remains high and thick, and hence prevents efficient hole collection at the contact (see Figure 7.12(a)).

In this work, we demonstrated that $GaN_{1-x}Sb_x$ were P-type conductive for $x > 0.06$. In particular the hole concentration was found to be 1-2 orders of magnitude higher than that of P-GaN achieved by far. This opens a promising perspective to provide a good ohmic contact to P-GaN. As shown in Figure 7.12(b) it is expected that the E_F is pinned close the Sb-derived E_V^+ sub-band (see Figure 7.9). Thus a very thin $GaN_{1-x}Sb_x$ buffer layer deposited on top of P-type GaN layer could help reducing the contact barrier.

During a hole transport from the P-GaN layer through the $GaN_{1-x}Sb_x$ layer, first, the free hole in the P-GaN is transferred to the Sb-derived upper VB by tunneling through the thin potential barrier due to high doping level of $GaN_{1-x}Sb_x$. Then the hole transport from the $GaN_{1-x}Sb_x$ layer to the metal is facilitated by the lowered potential barrier height (from GaN VB (-7.6 eV) to Sb-derived subband (-5.9 eV)), and the tunnel junction due to high hole concentration in the $GaN_{1-x}Sb_x$ layer. The $GaN_{1-x}Sb_x$ buffer layer should remain thin because of its low E_{gap} relative to the 3.4 eV E_{gap} of GaN.

7.5 Summary

Electrically, the $GaN_{1-x}Sb_x$ changes from N-type to P-type as Sb% increases, and it shows strong P-type conductivity as Sb $\geq$ 6% (higher than the highest reported P-type conductivity for Mg doped P-type GaN [4][78][45]). The hole concentration and P-type conductivity are further increased upon rapid thermal annealing, these values reached their maximum upon annealing at 650°C. By modeling the hole concentration with the BAC, the E_F of this alloy is determined to be following the Sb-derived E_V^+ band (at 50 meV above) across the Sb% composition range studied.

Taking the advantage of the multiple abrupt DOS transitions, the $GaN_{1-x}Sb_x$ (or HMAs in general) can potentially be developed into a new type of thermoelectric material with high hole concentration and high Seebeck coefficient [59]. Lastly, the strongly P-type $GaN_{1-x}Sb_x$ can be applied to improve the ohmic contact in the P-type layer of the GaN LED devices.

Chapter 8

Energy conversion application and conclusion

8.1 $ZnO_{1-x}Te_x$ / $GaN_{1-x}Sb_x$ on Si double junction solar cell

As shown in previous chapters, $ZnO_{1-x}Te_x$ is readily N-type conductive and $GaN_{1-x}Sb_x$ is strongly P-type conductive, and the E_{gap} of these two alloys can be tuned to 1.8 eV with x = 0.23, and 0.07 for $ZnO_{1-x}Te_x$ and $GaN_{1-x}Sb_x$ respectively. It is viable to build a 1.8 eV band gap top cell with $ZnO_{0.77}Te_{0.23}$ and $GaN_{0.93}Sb_{0.07}$ heterojunction.

Besides the suitable band gap energy, the lattice mismatch and band edge alignment between the interfaces of $GaN_{0.93}Sb_{0.07}/ZnO_{0.77}Te_{0.23}$ and $ZnO_{0.77}Te_{0.23}$/Si are critical to the device performance.

Lattice matching

Between $GaN_{0.93}Sb_{0.07}$ and $ZnO_{0.77}Te_{0.23}$

Both GaN and ZnO are preferred to have Wurtzite structure with c-axis orientation, which are observed in XRD shown in figures 3.4 and 6.4 respectively. ZnO has lattice constants a = 3.25 Å, c = 5.21 Å, and GaN has lattice constants a = 3.19 Å, c = 2.48 Å [40].

Since $GaN_{1-x}Sb_x$ is expected to be grown on top of $ZnO_{1-x}Te_x$ in the proposed heterojunction structure, the misfit strain is calculated with equation 8.1:

$$misfit = \frac{a_{GaNSb} - a_{ZnOTe}}{a_{GaNSb}} \times 100\% \tag{8.1}$$

For pure GaN and ZnO (i.e. x = 0), the lattice mismatch is small, where the calculated misfit < 1.9 %. Because of the small misfit, bulk ZnO is a commonly used as a single crystal substrate for GaN growth [27].

ZnTe and GaSb (i.e. x = 1.0) naturally exist in zincblende crystal structure with lattice parameter a = 6.101 Å, and 6.096 Årespectively. The lattice parameter for zincblende ZnO and GaN are a = 4.6 Å, and 4.5 Å respective [66][94]. With the introduction of 7% Sb in GaN, the lattice constant is calculated to be a = 4.61 Å, and that for 23% Te in ZnO is a = 4.95 Å. And hence the misfit between $GaN_{0.93}Sb_{0.07}$ layer and $ZnO_{0.77}Te_{0.23}$ layer is $< 7.2\%$. Therefore the single crystal lattice misfit between the two layers is reasonably small.

The $GaN_{0.93}Sb_{0.07}$ obtained in this study is polycrystalline observed in TEM and XRD. The $ZnO_{0.77}Te_{0.23}$ is almost amorphous observed under XRD, and very small (< 5 nm) grains are only observed under TEM. Therefore lattice mismatching is not critical for stacking the polycrystalline layer on an amorphous substrate. However, the P-type $GaN_{0.93}Sb_{0.07}$ films in this work are grown on single crystal sapphire substrate, it is necessary to test growing this material on an amorphous substrate (such as on glass substrate) to determine if similar electrical properties could be retained.

Between $ZnO_{0.77}Te_{0.23}$ and Si

Si has diamond crystal structure with a lattice constant of 5.431 Å[56]. Wurtzite ZnO has a lattice constant a = 3.25 Å, thus the misfit between wurtzite ZnO and Si is large $> 67\%$. Zincblende ZnO has a lattice constant a = 4.6 Å, thus resulting in a more manageable misfit ($< 13\%$). Alloying Te in ZnO enlarges the lattice parameter, with x = 0.23, the misfit between $ZnO_{0.77}Te_{0.23}$ and Si is $< 7.9\%$. In literature, epitaxial ZnO has been successfully grown on Si (111) directly [58], or with a thin buffer layer [35].

In addition, Si (111) has been reported to favor the growth of the wurtzite nitrides due to the sixfold atomic arrangement at the surface, such as AlN-on-Si shown in Figure 8.1 [20]. And Si (111) is an emerging substrate choice for growing epitaxial GaN despite the lattice mismatch. Given the similar lattice structure between ZnO and GaN, the lattice mismatch between the $ZnO_{0.77}Te_{0.23}$ layer and Si substrate can be managed. Figure 8.2 shows the history of GaN-on-Si growth technology and its advancement from small size sample to multiple wafers on 200-mm-diameter Si (111) for high-electron-mobility-transistor (HEMT), and LED devices [74] [57].

Given the similarity between ZnO and GaN, and the lattice expansion brought by incorporating Te in ZnO lattice, we are optimistic to achieve reasonable good quality thin film of $ZnO_{0.77}Te_{0.23}$ on Si (111) substrate.

Electronic band edge alignment

The band edge positions for $ZnO_{0.77}Te_{0.23}$ and $GaN_{0.93}Sb_{0.07}$ are determined from the BAC and X-ray measurements shown in Chapter 4 and 5 respectively. Figure 8.3 shows the electronic band alignment of both these two layers with respect to Si.

Figure 8.4(top) shows the interface band bending for a E_F aligned device. The top cell is P-$GaN_{0.93}Sb_{0.07}$/N-$ZnO_{0.77}Te_{0.23}$ with $E_{gap} = 1.8$ eV, and bottom cell is Si with $E_{gap} = 1.1$ eV. $GaN_{0.93}Sb_{0.07}$ has a higher CB than that of $ZnO_{0.77}Te_{0.23}$ in absolute scale resulting in a

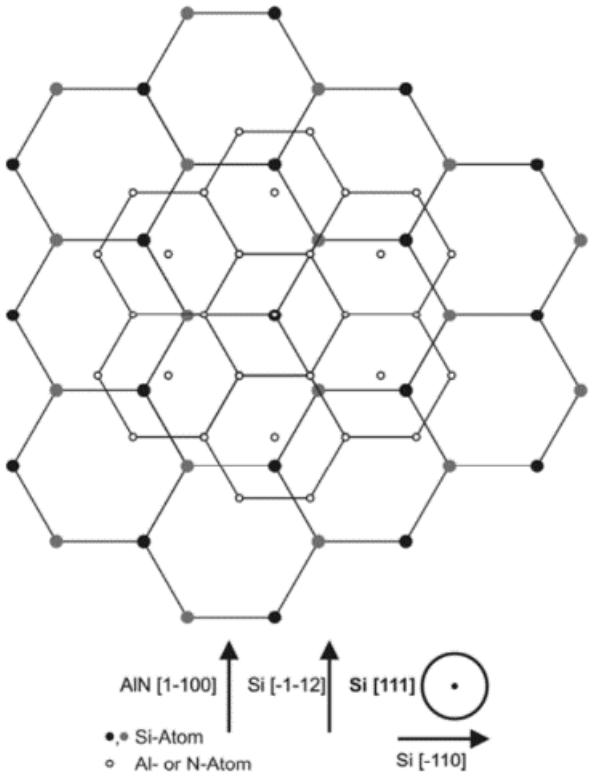

Figure 8.1: Atomic arrangement of Wurtzite AlN on Si (111) [20].

very large the band bending in the top cell. Such large band bending is favorable for a larger open circuit voltage in the top cell. In addition, the CB of $ZnO_{0.77}Te_{0.23}$ is very close to the VB of Si, therefore a tunnel junction is formed naturally without the additional n+/p+ layers. Ohmic contact between N-ZnO and P-Si has been verified in multiple reports [69]. Figure 8.4(bottom) shows the band bending of the double junction device under illumination. The electrons generated in the top cell diffuses toward the bottom cell, and recombines with the holes generated in the bottom cell at the N-$ZnO_{0.77}Te_{0.23}$ to P-Si interface. Careful layer thickness must be considered to ensure a matched current between top and bottom cells. The total open circuit voltage of the entire cell is the difference between the quasi-fermi level $E_{FP,Top}$ and $E_{FN,Bottom}$, with the overall current flowing from Si bottom cell to the GaNSb/ZnOTe top cell.

Layer thickness and contact metals

In the top cell, the N-type $ZnO_{0.77}Te_{0.23}$ should be used as the absorber layer because of better electron transport in its CB than the hole transport in the Sb-derived narrow E_V^+ band in $GaN_{0.93}Sb_{0.07}$.

The optical absorption coefficient for $ZnO_{0.77}Te_{0.23}$ at 1.8 eV is 2×10^4 cm^{-1} and its

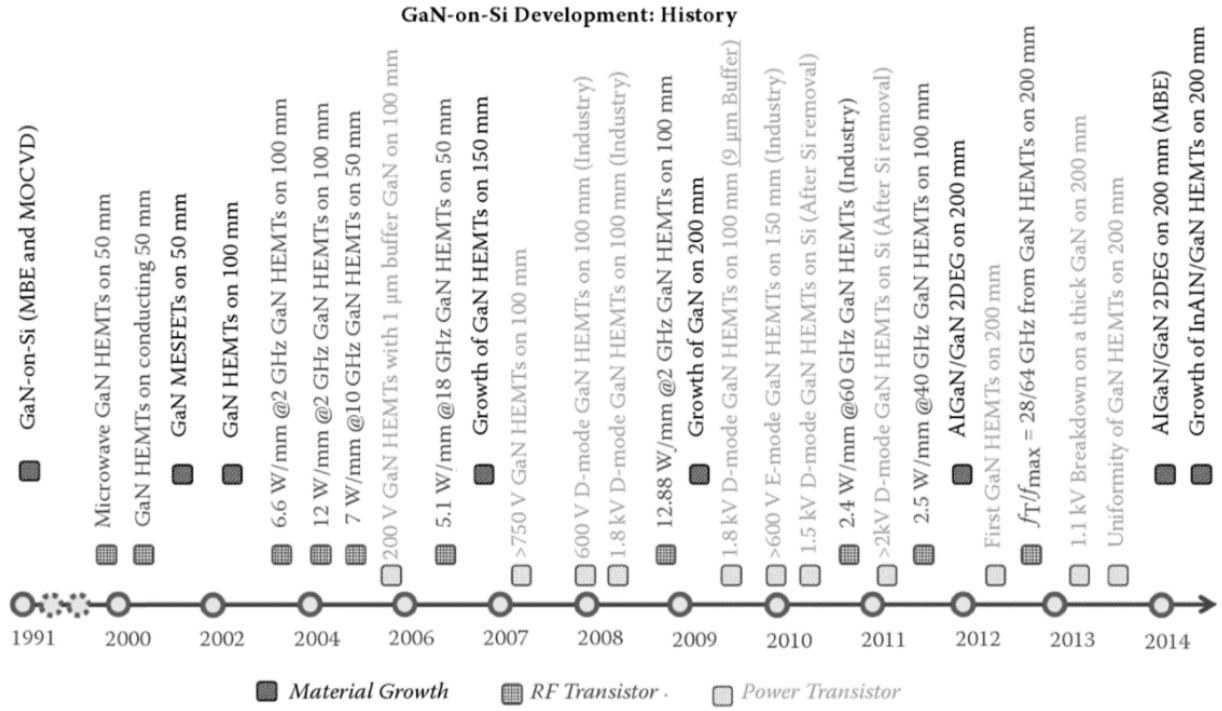

Figure 8.2: History of GaN-on-Si development from 1991 to 2014 for material growth, radio frequency transistors, and power transistors [74]

absorption coefficient increases with increasing photon energy. Therefore, the minimum thickness required for the $ZnO_{0.77}Te_{0.23}$ layer is 500 nm. And a very thin layer of $GaN_{0.93}Sb_{0.07}$ shall be used as a hole emitter.

The contact metal for N type Si, conventional Silver paste can be applied. For the P-type contact on $GaN_{0.77}Sb_{0.07}$, as shown in Figure 8.3, its E_F is at -5.9 eV, thus a high work function metal (such as NiAg used to contact P-type GaN) should be used to ensure a downward band bending to avoid contact barrier for holes.

Therefore, a device architecture shown in Figure 8.5 is proposed. A similar device architecture is found in GaN/Si tandem solar cell [84]. In the case of GaN/Si, the overall device efficiency suffered from the large E_{gap} of GaN (3.4 eV). In our case, with an optimal top cell E_{gap} and proper band alignment, it is more promising to achieve a highly efficient double junction solar cell.

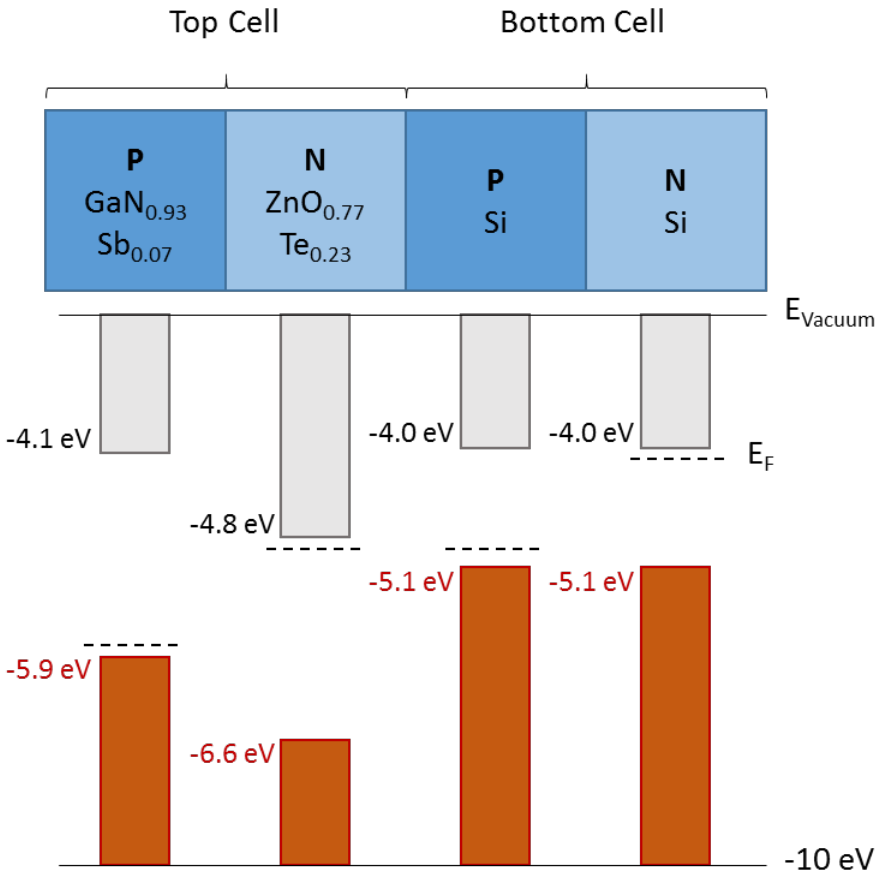

Figure 8.3: The electronic band alignment between $ZnO_{0.77}Te_{0.23}$, $GaN_{0.93}Sb_{0.07}$, and Si, with E_F shown as the black dash line.

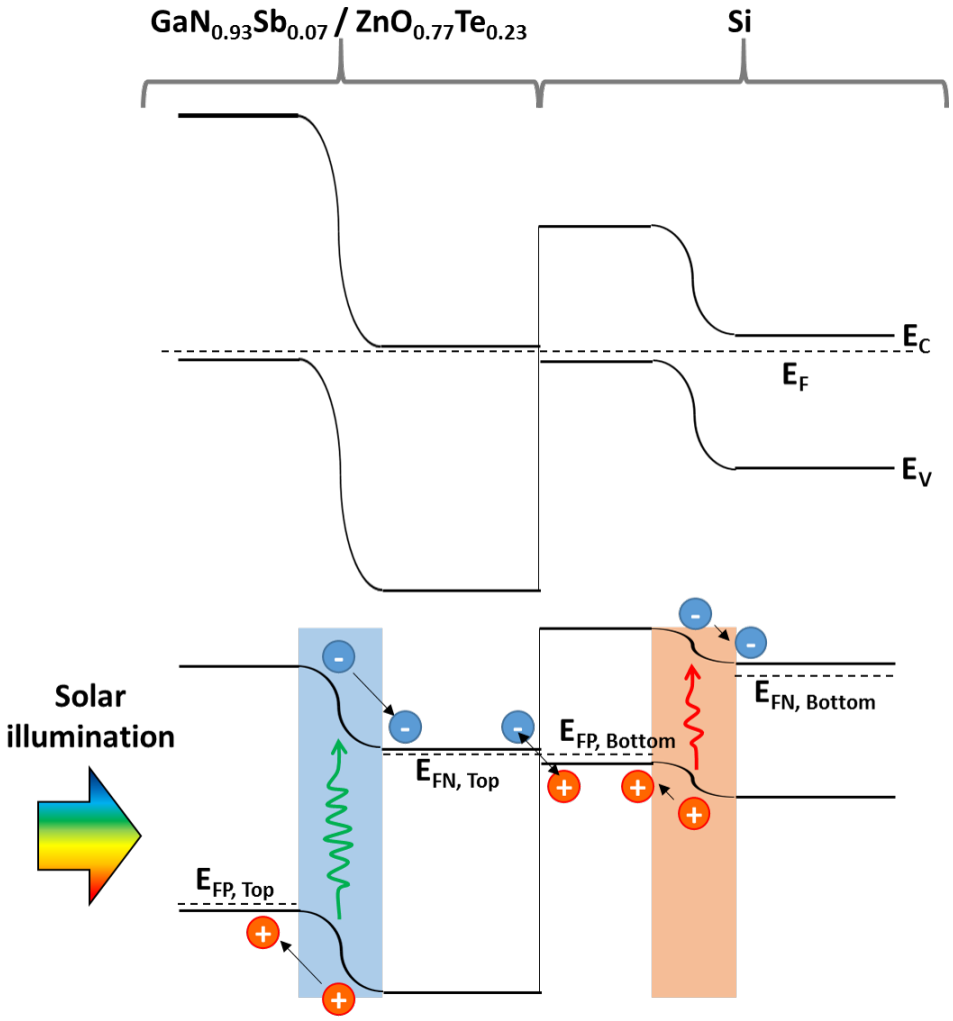

Figure 8.4: The electronic band bending between $ZnO_{0.77}Te_{0.23}$ / $GaN_{0.93}Sb_{0.07}$ top cell and Si bottom cell with aligned E_{gap} in equilibrium (top figure), and under solar illumination (bottom figure).

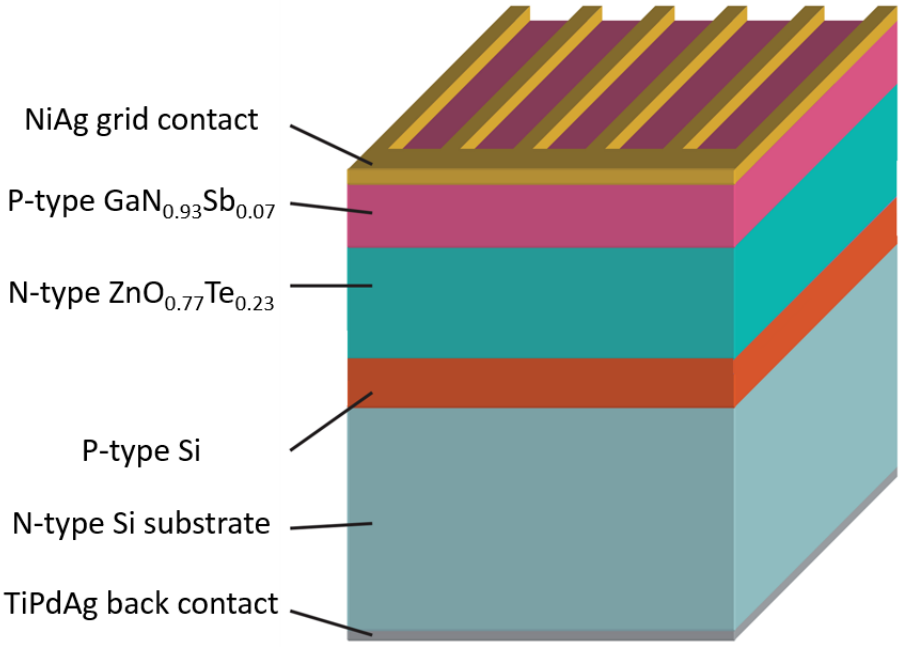

Figure 8.5: Device architecture of proposed $GaN_{0.93}Sb_{0.07}$-$ZnO_{0.77}Te_{0.23}$ on Si double junction solar cell.

Chapter 9

Conclusion and outlook

Band structure engineering is a powerful tool to tailor semiconductors for specific needs. Today, semiconductor devices are designed around material properties. PV, LED devices are designed around the semiconductor with the suitable E_{gap} energy. Transistors and computer chips are limited by the mobility silicon.

As our base of knowledge about semiconductor materials properties grows, we not only understand material limitations but also find solutions to overcome inconvenient properties. Now with the development of more advanced nanotechnologies (including the nano-scale 3D additive manufacturing techniques), we can imagine a world where interdisciplinary engineers can design a device structure to fulfill a particular application, then synthesize the material with the right properties to meet the device requirements.

In this context, this dissertation provides a roadmap for undertaking such a challenge. The ultimate application is to design the top cell for a double junction solar cell with Si-bottom cell. Therefore, a E_{gap} of 1.8 eV is required, and specific electronic band alignment is also needed to facilitate the charge transport across the layers. Therefore, the goal is to narrow the E_{gap} of wide E_{gap} oxide and nitride materials to meet the device requirement. Chapter 2 provided background information on the band structure engineering technique used in this work. Both $ZnO_{1-x}Te_x$, and $GaN_{1-x}Sb_x$ were theoretically designed based upon the integration of the top cell needs.

The next step was to choose an appropriate method of synthesis. In general, HMA are difficult to synthesis. For the initial growth of $ZnO_{1-x}Te_x$, and $GaN_{1-x}Sb_x$, non-equilibrium techniques PLD, and low temperature MBE are used to synthesize the alloys respectively. Further development of these material alloys for large scale manufacturing processes, alternative growth methods (sputtering, CVD, or evaporation) should be considered. Chapter 3 and 6 demonstrated the growth parameter space explored for both materials.

The band structure of $ZnO_{1-x}Te_x$ and $GaN_{1-x}Sb_x$ were characterized in Chapter 4 and 6 respectively. Since this is the first systematic study of both alloys, thorough band structure characterizations have been conducted. The movement of the valence/conduction band edge was directly observed with X-ray absorption and emission spectroscopies. The exact band structure was determined by modeling the optical absorption coefficient, the results of which

were in good agreement. Together these findings confirmed the theoretical prediction of the valence band anticrossing interaction, when Te is introduced in ZnO, and Sb is introduced in GaN. With this method, the E_{gap} of ZnO and GaN are narrowed from UV-range to absorb photons in the visible range.

Finally, the carrier transport effect is characterized in Chapter 5 and 7 for $ZnO_{1-x}Te_x$ and $GaN_{1-x}Sb_x$ respectively. The undoped $ZnO_{1-x}Te_x$ are strongly N-type at very dilute Te range (<5%), with electron concentration upto 4×10^{20} cm^{-3} and mobility upto 30 $cm^2V^{-1}s^{-1}$. For P-type doping, adding Te helped the acceptor activation by developing the Te-derived E_V^+ band above the nitrogen deep level. But at the same adding Te increased the carrier compensation ratio which also created donor-like defects compensating the activated acceptors. Therefore, techniques of quenching of N-type native defects are necessary to achieve stable P-type conductivity in $ZnO_{1-x}Te_x$. $GaN_{1-x}Sb_x$ showed strong P-type conductivity when Sb *geq* 6% , and the P-type conductivity is further enhanced upon annealing. The hole concentration and P-type conductivity achieved for $GaN_{1-x}Sb_x$ is higher than the highest reported values for Mg doped P-type GaN. Chapter 7 illustrated detailed modeling of the hole concentration under the VBAC framework. The modeling result showed that the E_F of this alloy are pinned at Sb-derived band disregard the alloy composition. The efficient hole transport within the Sb-derived band in $GaN_{1-x}Sb_x$ makes it a potential stepping stone material to enhance the P-contact in GaN devices.

Challenges and future work

Throughout this dissertation, we have laid out the band structure engineering of $ZnO_{1-x}Te_x$ and $GaN_{1-x}Sb_x$ with properly engineered E_{gap} and band alignment. There are a few interesting scientific pursuits and challenges to be overcome before both these material systems can be commercialized.

In Chapter 8, we proposed the architecture of a 1.8 eV E_{gap} heterojunction top cell of $ZnO_{0.77}Te_{0.23}$ N-type absorber and a thin layer of $GaN_{0.93}Sb_{0.07}$ hole emitter. A prototype device must be built to demonstrate the efficiency of such double junction device.

Another challenge is the synthesis method. Non-equilibrium synthesis techniques such as PLD and low temperature MBE are used in order trap large atoms (Te and Sb) in place of smaller atoms (O and N). However, the low temperature growth is known to lead to disrupted crystal structures. In the PLD growth of $ZnO_{1-x}Te_x$ thin films, we explored the contribution of Ar/O2 background gas ambient in both the Te-rich and O-rich growth regimes, and these parameter space could be used as guidance for more scalable synthesis methods: sputtering or evaporation.

A second synthesis challenge is to achieve stable P-type $ZnO_{1-x}Te_x$. In this work, P-type doping with N_2 gas has been tried. The original hope is that the high energy ablation plume in PLD can break the strong triple bond in an N_2 molecule, given the low acceptor activation rate with >3% total N measured in the sample, it is believed that nitrogen may still exist as N_2 molecule in the thin film. Post processing techniques could be tried by including ion implantation followed by an anneal with a capping layer or in a nitrogen / ammonia

environment. Ammonizing of the PLD target prior to growth could also be applied. Besides nitrogen, other group V elements (including P, As, and Sb) should be also tried as P-type dopant. Theoretical calculations have stated that all these group V elements exist as deep acceptor-levels in ZnO, which could potentially be overcome by the Te-derived E_V^+ band.

Lastly the inter-diffusion of group III-V elements into the II-VI may cause a short current passage within the heterojunction. In that case P-type ZnTe can be used to replace the P-typ GaNSb as hole emitter.

There are still many challenges in the development of Si-based double junction PV device. The study of $ZnO_{1-x}Te_x$, and $GaN_{1-x}Sb_x$ has followed one such thread. It revealed two extreme band structure engineering alloys and hope to motivate the future work in the exploration of novel material engineering techniques and energy conversion device designs.

Appendix A

Rutherford backscattering spectrometry

The RBS detects the energies and amount of the backscattered ions from a solid target. As shown in Figure A.1 the incident probe is a mono-energetic ion beam, typically MeV He ions (3.04 MeV ion beam is used in this work). The scattered α particles from the target are energy analyzed by a solid particle detector (Si surface barrier detector) positioned at a backscattered angle with respect to the incident ion beam (typicallying ranging from 100 - 170° depending on the specific analysis). The energy of the energy of the backscattered He ions are dictated by conservation of energy and momentum between the incident ion and scattering atom and can be related to the depth and mass of the target. The amount of the backscattered ions from any given element is proportional to its concentration. Therefore RBS is commonly used as a tool to investigate the depth profile of individual elements in a solid quantitatively.

Figure A.2 shows an RBS spectra for a $ZnO_{1-x}Te_x$ thing film sample with 12% Te and 239 nm thickness.

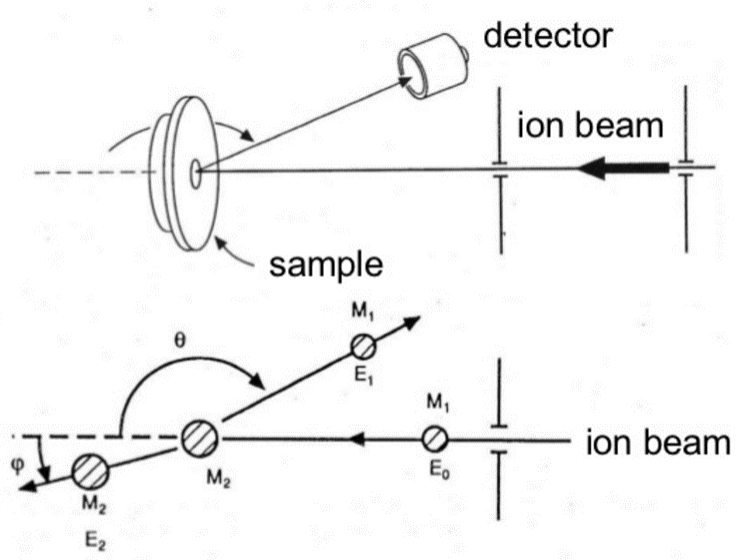

Figure A.1: Schematic illustration of the physical processes during a ion beam backscattering process.

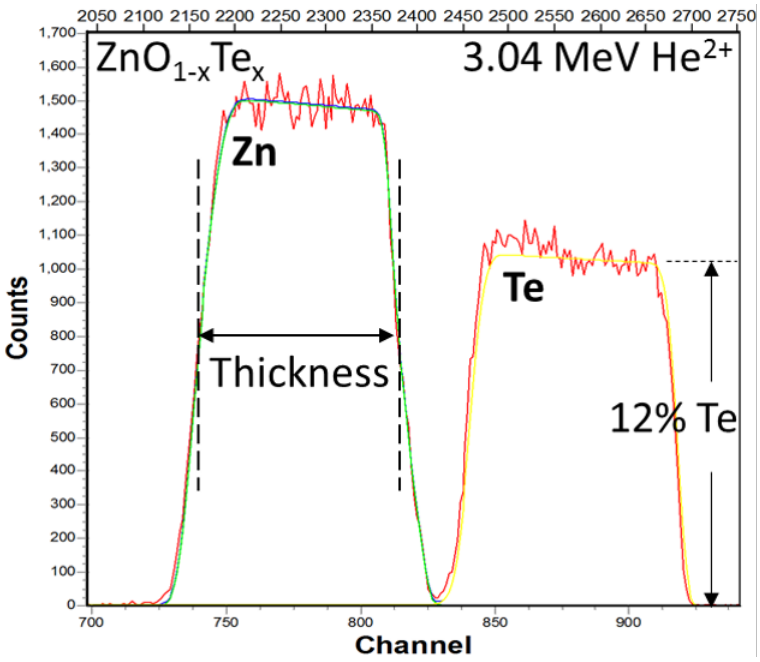

Figure A.2: The RBS spectra for a $ZnO_{1-x}Te_x$ thin film sample with 12% Te and 239 nm thickness.

Appendix B

Nuclear reaction experiment for nitrogen detection

When an energetic particle hits a nucleus in a target, depending on the mass of the particle, the mass of the target, and the energy of the particle, a variety of final products may form. RBS is a special case in such reaction in which the reaction products are the same as those before reaction. In cases where the incident beam energy exceeds a certain threshold value, other energetic particles appear in the spectrum. The detection of these particles usually provide information which is not obtainable from RBS. The Nulear Reaction Analysis (NRA) technique is very useful as a tool for the detection and profiling of light elements in heavy matrix. In many cases such particle-particle NRA can be carried out in a RBS setup with only minor modifications.

The NRA experiment has been applied to detect nitrogen content in the nitrogen-doped $ZnO_{1-x}Te_x$, which is otherwise too light to be detected by RBS. The experimental setup, and sample spectra are shown in Figure B.1. For the $ZnO_{1-x}Te_x$ deposited with PLD, with 1 mTorr of N_2 ambient pressure, 3% nitrogen is detected in the sample (Figure B.2), and the nitrogen content does not show clear change with PLD laser energy. Figure B.3 shows a sample NRA spectra for a ZnOTe:N thin film grown on Si substrate with 1.4% Te and 3% total nitrogen in the film.

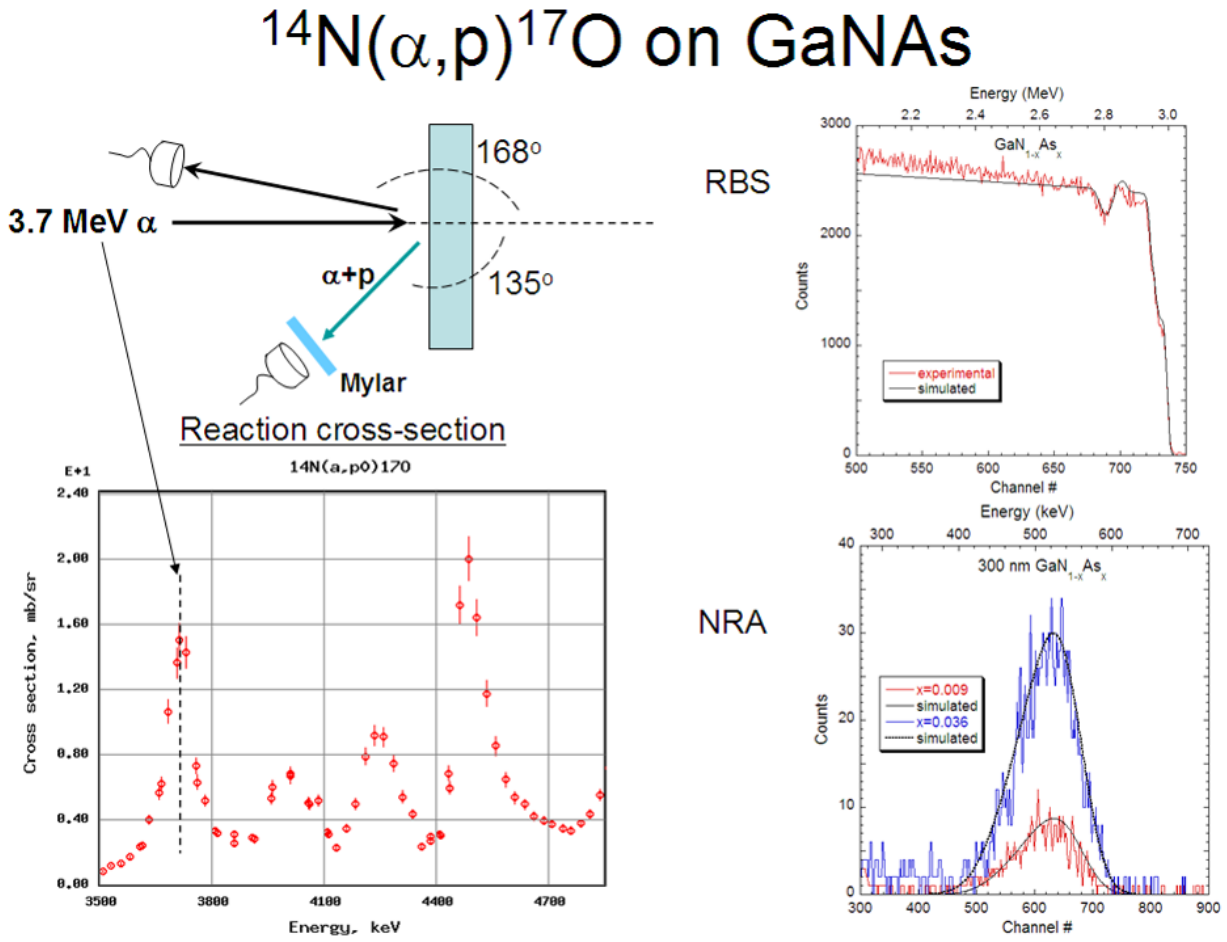

Figure B.1: The experimental setup, and sample spectra for the nitrogen detection experiment.

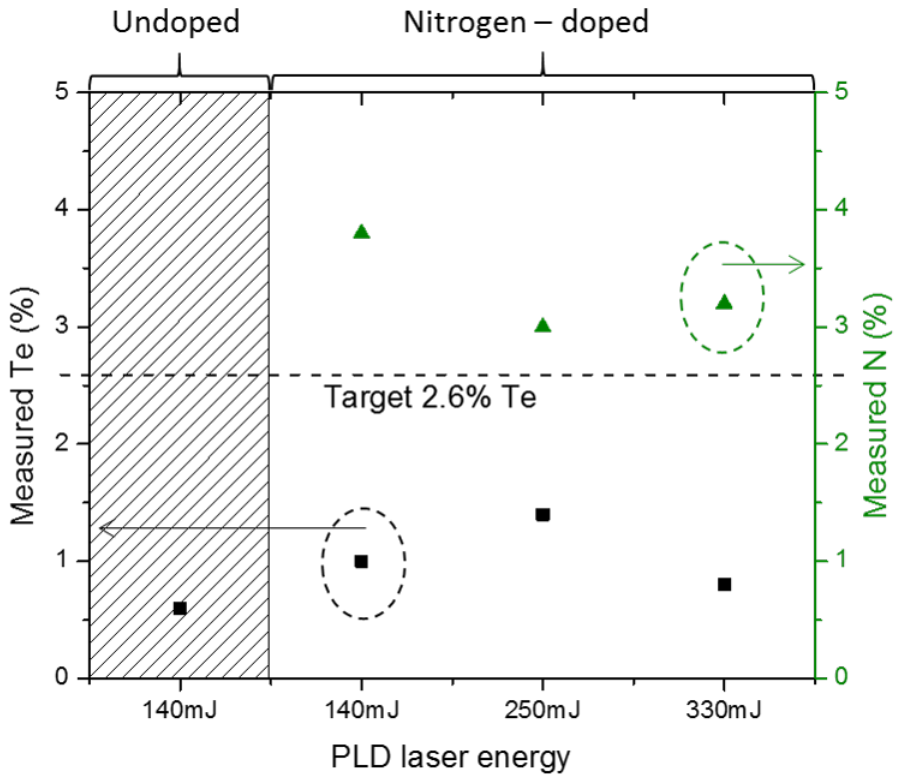

Figure B.2: The Te and N % in both unoped, and nitrogen doped $ZnO_{1-x}Te_x$ thin films with respect to PLD laser energy.

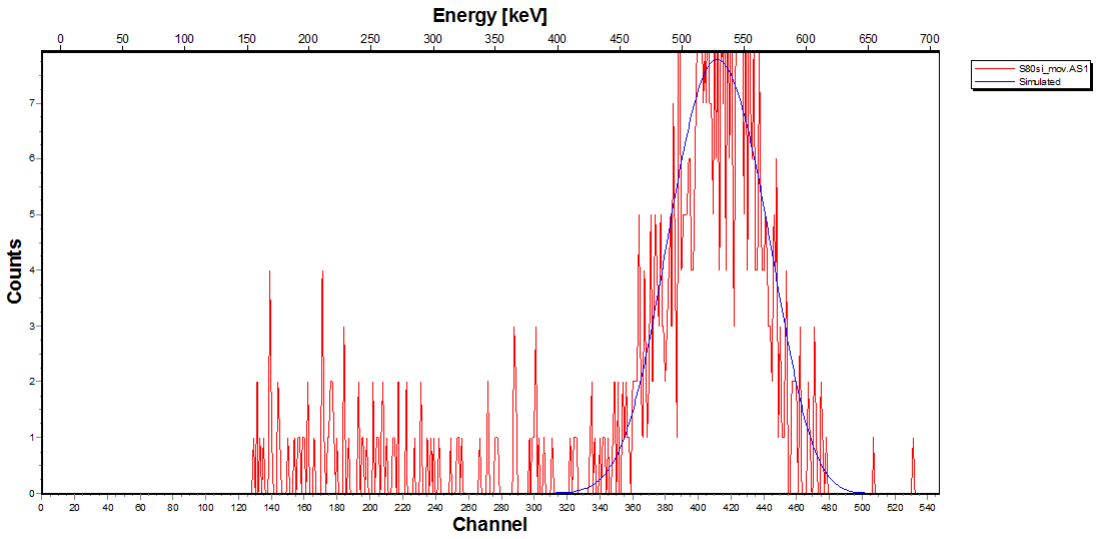

Figure B.3: The NRA spectra of a $ZnO_{1-x}Te_x$ sample with 1.4% Te and with 3% total nitrogen.

Appendix C

X-ray photoelectron spectroscopy full spectrum for $ZnO_{1-x}Te_x$

During the XPS experiment, the full spectrum from 1200 eV to 0 eV (i.e. E_F of the sample) is scanned (shown in Figure C.1). A few characteristic regimes of the electronic state of the elements in the sample are scanned with finer resolution: Te 3d, Zn 2p, O 1s, C 1s, and valence band regime. In Chapter 4, the VB regime of the spectra is studied in detail, and the C 1s peak is used to align the Fermi-energy for each sample.

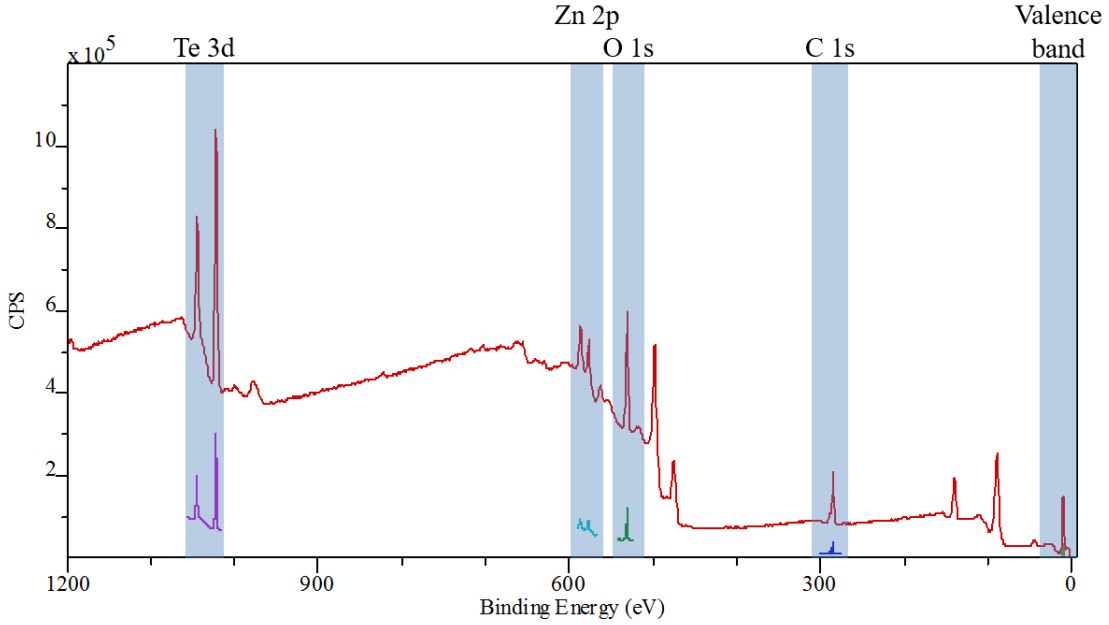

Figure C.1: The full XPS spectrum of a $ZnO_{1-x}Te_x$ sample with x = 0.006. The shaded regions are the characteristic spectra for the specific electronic state of the elements in the sample: Te 3d, Zn 2p, O 1s, C 1s, and valence band.

Appendix D

Low temperature hall effect measurement of $GaN_{1-x}Sb_x$

Low temperature hall effect measurement were conducted on as-grown $GaN_{1-x}Sb_x$ samples by Prof. Kin Man Yu at the City University of Hong Kong. Only the $GaN_{0.44}Sb_{0.56}$ sample can be measured at 77K, whereas all the other samples present contact difficulties during the measurement. Figure D.1(a) shows the resistivity as a function of reciprocal temperature $\frac{1}{T}$. At low temperature a deviation from the typical thermally-activated behavior ($\rho = \rho_0 \exp(\frac{E_A}{kT})$) is observed. The deviation of the linear trend at low temperature can be the result of a change of conduction mechanism. In Figure D.1(b), the measurement data shows better agreement with $(\frac{1}{4})^{\frac{1}{4}}$. Such behavior could be attributed to the hopping type of transport between poorly mobiles states at low temperature. This conduction model, derived by Mott [76], describes the tunnelling of carriers between localized states. This behavior is commonly observed in disordered materials, such as amorphous Si, C, Ge, and low-temperature grown GaAs:Be [10]. In the case of as-grown $GaN_{1-x}Sb_x$, the Fermi level is expected to be above the E_V^+ band, based on our calculation in 7.2. At low temperature only a few mobile holes can participate to transport. In addition, the immobile states are located above the E_V^+, which are likely to conduct via hole hopping.

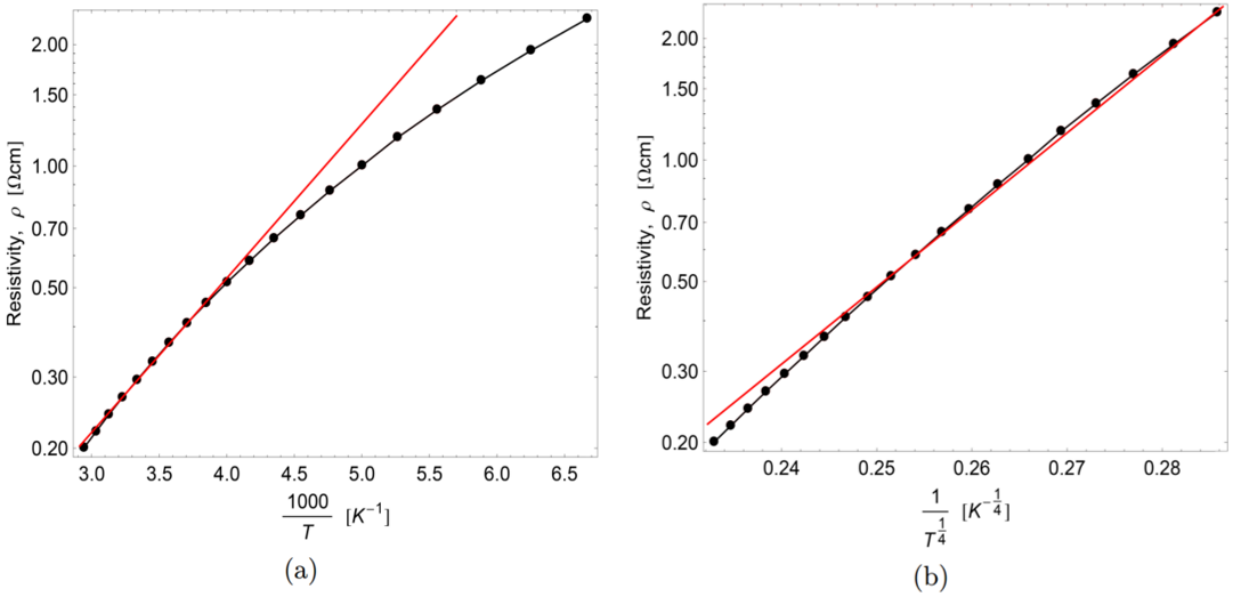

Figure D.1: Resistivity of $GaN_0.44Sb0.56$ with respect to (a) $\frac{1}{T}$ (b) $\frac{1}{T^4}$.

Appendix E

Low temperature hall effect measurement of $ZnO_{1-x}Te_x$

Low temperature hall effect measurement was also conducted on as-grown $ZnO_{1-x}Te_x$ samples. The N-type samples are conductive under 77 K. Figure E.1 shows the temperature variable resistivity of a pure ZnO and $ZnO_{0.92}Te_{0.08}$. Both samples show monotonic decrease in resistivity with increasing temperature.

For ZnO, the decrease in resistivity is majorly brought by the increase in electron mobility E.2(left) (relative constant electron concentration with increasing temperature E.2(right)). In single crystal semiconductor, a decrease in mobility is expected with increasing temperature due to the increase in phonon scattering. The samples in this study are polycrystalline,

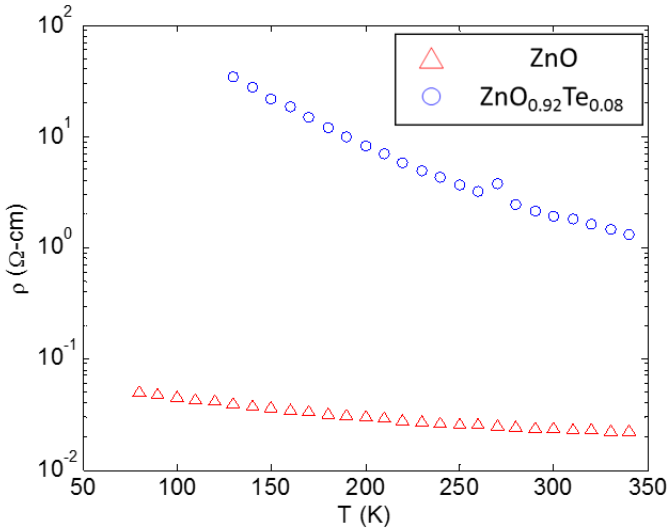

Figure E.1: The temperature variable resistivity of pure ZnO, and $ZnO_{0.92}Te_{0.08}$ thin film samples synthesized in this study.

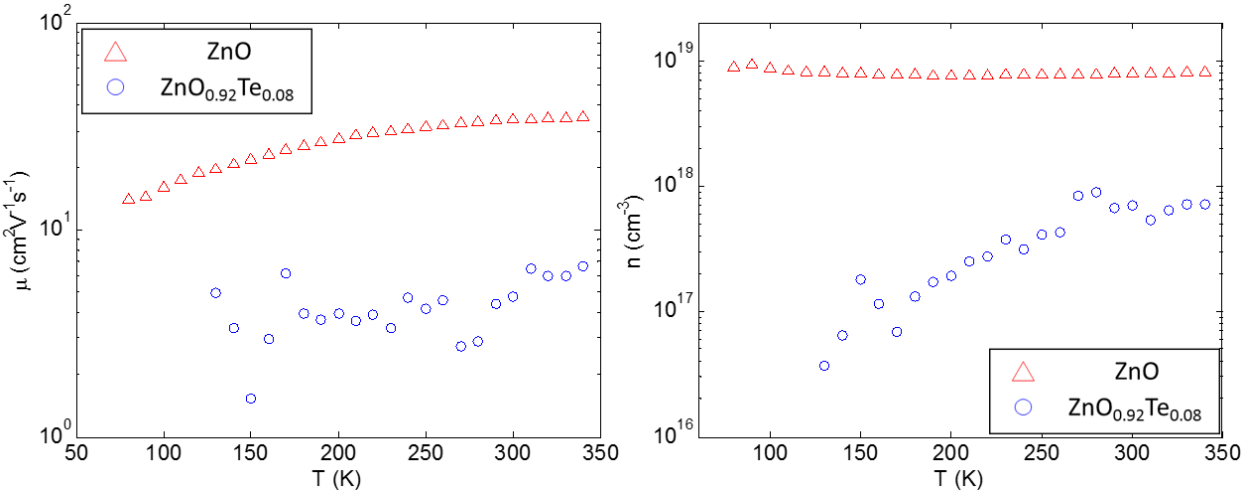

Figure E.2: The temperature variable (left). electron mobility and (right). electron concentration of pure ZnO, and $ZnO_{0.92}Te_{0.08}$ thin film samples synthesized in this study.

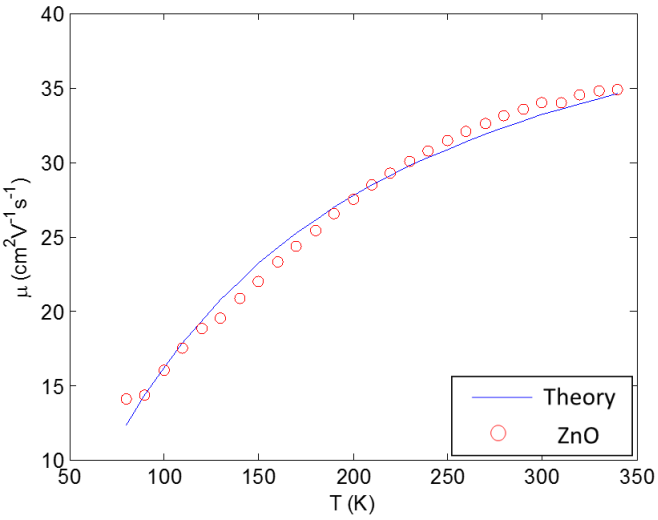

Figure E.3: The fitting of temperature variable electron mobility of ZnO with grain boundary scattering model [29].

therefore grain boundary scattering effect is attributed to the increase in electron mobility upon increasing temperature. The grain barrier model is well-described by Ellmer [29] with the following equation: $\mu = \mu_{grain} \exp(-\frac{\Phi_b}{kT})$, where Φ_b is the grain barrier height and ν_{grain} is the carrier mobility within the grain. Figure E.3 shows the fitting with the grain barrier model, with $\nu_{grain} = 47.5$ $cm^2V^{-1}s^{-1}$and $\Phi_b = 9.3$ meV. The results are in reasonable agreement with the fitting results found in Ellmers study of polycrystalline ZnO [29].

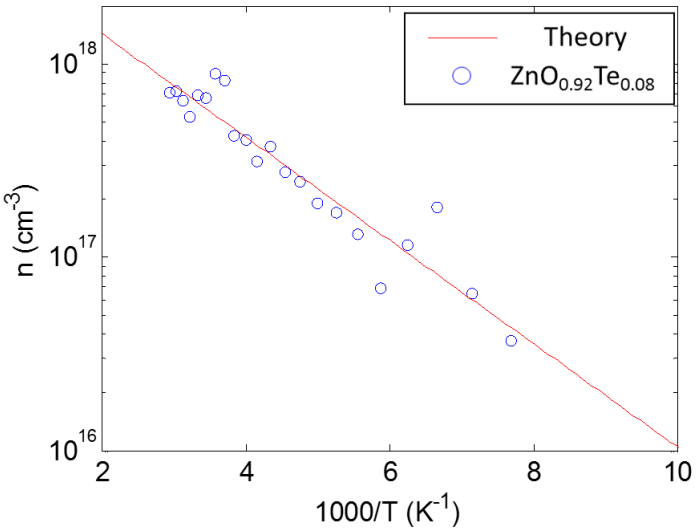

Figure E.4: The fitting of temperature variable electron concentration with the electron activation model.

For $ZnO_{0.92}Te_{0.08}$, the decrease in resistivity is majorly caused by the activation of mobile electrons. The fitting of electron activation with temperature is shown in Figure E.4. The donor activation energy is found to be $E_D = 52.9$ meV with the donor concentration $N_D = 1.62 \times 10^{19}$ cm$^-3$ which is comparable to the value reported for crystal ZnO [63]. Donor concentration in our sample is over two orders of magnitude higher than the value reported for the bulk single crystal ZnO [63]. In addition, the fitting shown assumed zero acceptor concentration $N_A = 0$. As discussed in Chapter 4, the thin films synthesized in this study have high carrier compensation ratio, therefore the N_D expected to be higher than the to be much higher than that in the bulk single crystal ZnO.

Appendix F

Atomic force microscopy for $\mathbf{ZnO_{1-x}Te_x}$

Figure F.1 shows the phase scan of the atomic force microscopy of $ZnO_{1-x}Te_x$ samples grown on Si substrate, which x = 0.016, 0.06, 0.096, 0.146, 0.236, and 0.316. All the samples scanned are grown under 5 mtorr of Ar gas ambient, except the sample with 14.6% Te which is grown under 1 mtorr of Ar gas ambient. The bright spots on the surface are regarded as the surface particulates formed during the PLD film growth. It is worth noticing that the particulate density increases with increasing Te content, thus it is related to Te concentration in the laser induced plume. As discussed in Chapter **??**, Te is preferentially deposited under higher ambient gas pressure due its higher atomic mass (relative to the other species in the sample). This also explains the lower surface particulate density in the sample with 14.6% sample which is grown under slightly lower Ar pressure at 1 mtorr.

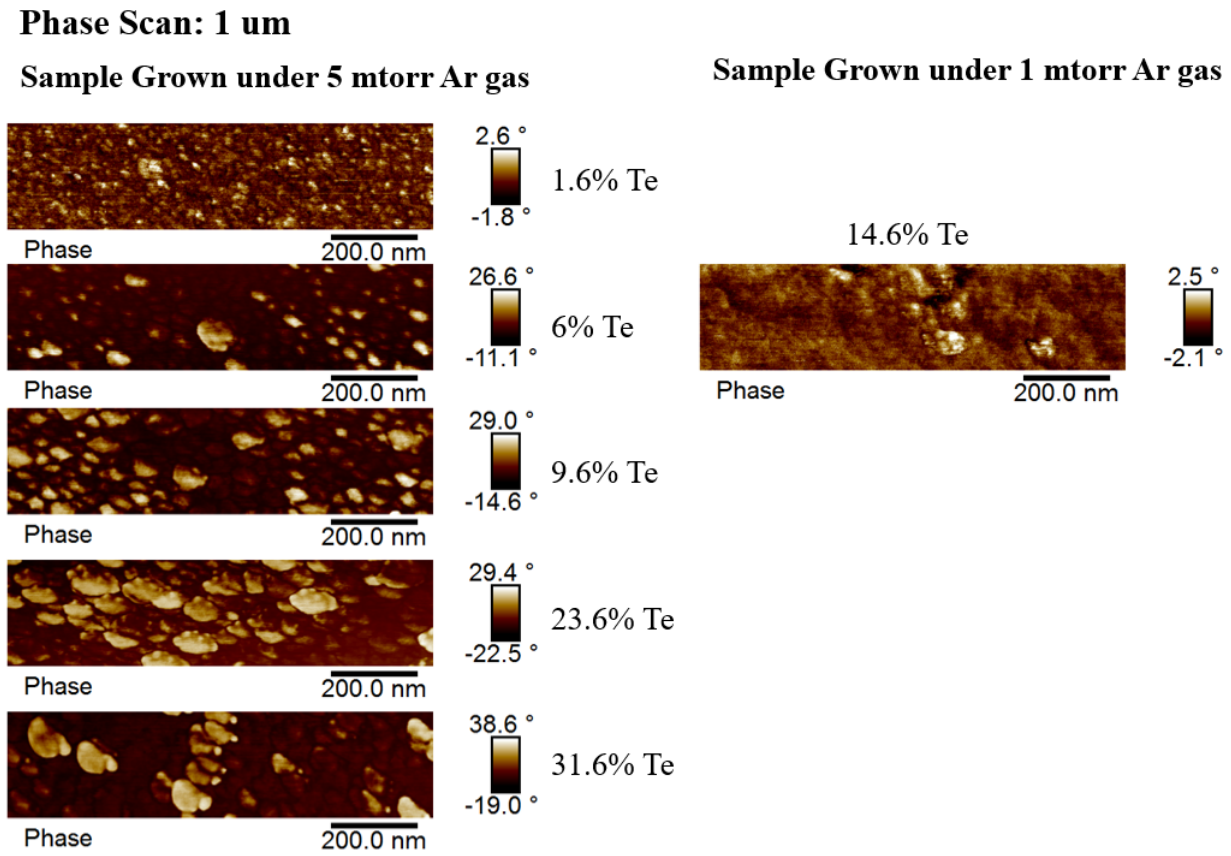

Figure F.1: The atomic force microscopy phase scan images for six $ZnO_{1-x}Te_x$ samples grown on Si substrate, which x = 0.016, 0.06, 0.096, 0.146, 0.236, and 0.316.

Appendix G

Photoluminescence of $ZnO_{1-x}Te_x$

The low-temperature (8 K) photoluminescence spectra of three $ZnO_{1-x}Te_x$ is shown in Figure G.1 for x = 0.04, 0.086, and 0.134. The most dominant peak observed is 3.3 eV, which is expected to be optical coupling between the E_V^- and the conductive band. It is worth noticing that the PL intensity decreases with increasing Te content. Such behavior is attributed to the decrease in grain size with increasing Te content, which increases the defect concentration in the sample and thus increases the rate of non-radiative recombination.

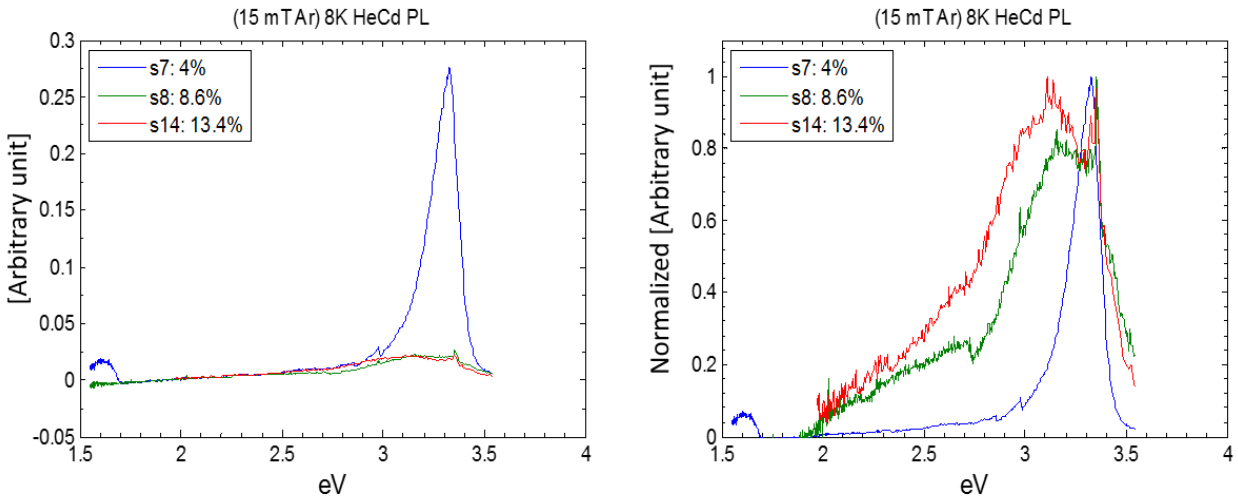

Figure G.1: The photoluminescence spectroscopy of $ZnO_{1-x}Te_x$ with x = 0.04, 0.086, and 0.134. (Left) Raw spectra; (Right) Normalized spectra.

Appendix H

Seebeck coefficient measurement

The Seebeck coefficient data reported in this dissertation are measured by a home-built setup. The setup is located in Lab 237 in Building 2 of the LBNL.

As illustrated in Figure **??**, the sample is placed on two heating stages. During the measurement, one stage is powered to heat up the sample, and hence creates a temperature gradient across the sample. Two thermocouples are attached on both hot and cold side of the sample. The larger mean free path of hot carriers resulted in an accumulation of charges on the cold side of sample, and thus an electrical voltage is induced by the thermal gradient. The voltage across the sample is measured through the thermocouples. With the measured voltage, and temperature difference the Seebeck coefficient is calculated as equation H.1.

$$S = \frac{-\Delta V}{\Delta T} \tag{H.1}$$

As shown in Figure H.2, T-type (Copper Constantan) thermocouples are used in the

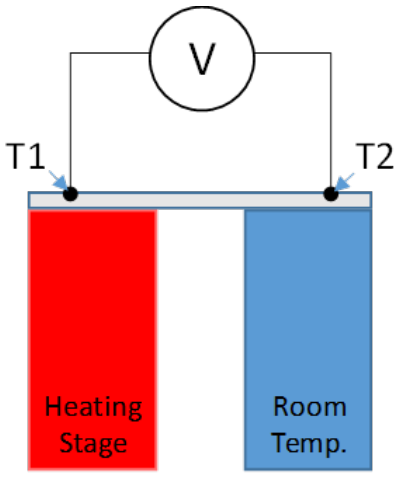

Figure H.1: The schematic of home-built Seebeck coefficient measurement setup in B2 LBNL lab 237.

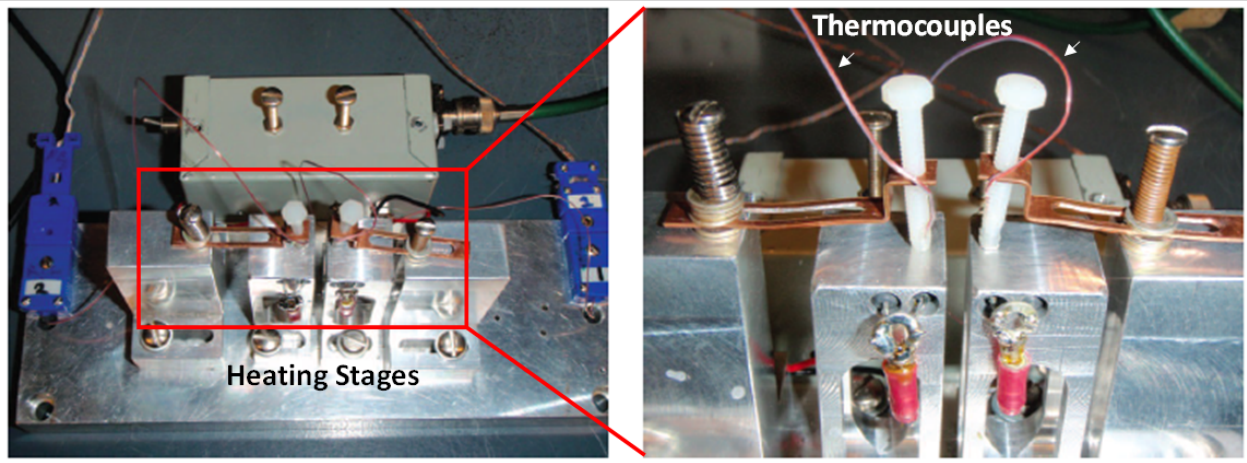

Figure H.2: Photographs taken for the Seebeck coefficient measurement setup.

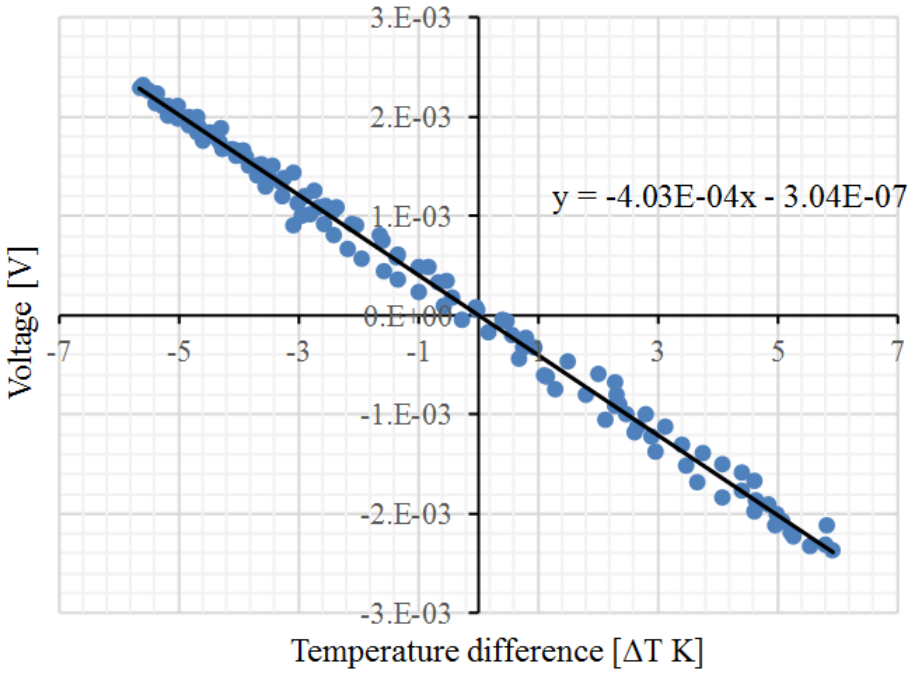

Figure H.3: Sample data for a single Seebeck Coefficient measurement.

setup which are rated and calibrated with error less than 1°Cfor room temperature measurements. Figure H.3 shows the data collected for a single measurement. Multiple scans are performed to ensure measurement consistency. For this measurement, the Seebeck coefficient is determined as -403 $\mu V/K$ from the slope of the linearly fitted data points.

Bibliography

[1] K. Alberi et al. "Formation of Mn-derived impurity band in III-Mn-V alloys by valence band anticrossing". In: *Phys. Rev. B* 78 (7 Aug. 2008), p. 075201. DOI: 10.1103/PhysRevB.78.075201. URL: http://link.aps.org/doi/10.1103/PhysRevB.78.075201.

[2] K. Alberi et al. "Valence-band anticrossing in mismatched III-V semiconductor alloys". In: *Phys. Rev. B* 75 (4 Jan. 2007), p. 045203. DOI: 10.1103/PhysRevB.75.045203. URL: http://link.aps.org/doi/10.1103/PhysRevB.75.045203.

[3] Samy Almosni et al. "Correlations between electrical and optical properties in lattice-matched GaAsPN/GaP solar cells". In: *Solar Energy Materials and Solar Cells* 147 (2016), pp. 53–60.

[4] Hiroshi Amano et al. "P-type conduction in Mg-doped GaN treated with low-energy electron beam irradiation (LEEBI)". In: *Japanese Journal of Applied Physics* 28.12A (1989), p. L2112.

[5] Paul M Amirtharaj and David G Seiler. "Optical properties of semiconductors". In: *Handbook of Optics* 2 (1995), pp. 36–1.

[6] Philip Warren Anderson. "Localized magnetic states in metals". In: *Physical Review* 124.1 (1961), p. 41.

[7] Michael NR Ashfold et al. "Pulsed laser ablation and deposition of thin films". In: *Chemical Society Reviews* 33.1 (2004), pp. 23–31.

[8] Colin D. Bailie et al. "Semi-transparent perovskite solar cells for tandems with silicon and CIGS." In: *Energy Environmental Science* 8.3 (2015), p. 956. ISSN: 17545692. URL: http://search.ebscohost.com/login.aspx?direct=true&db=edb&AN=101433587&site=eds-live.

[9] Uwe Bergmann and Pieter Glatzel. "X-ray emission spectroscopy". In: *Photosynthesis research* 102.2-3 (2009), pp. 255–266.

[10] DE Bliss et al. "Annealing studies of low-temperature-grown GaAs: Be". In: *Journal of applied physics* 71.4 (1992), pp. 1699–1707.

[11] PHILIP M. BOFFEY. *ATOM BY ATOM, PHYSICISTS CREATE MATTER THAT NATURE HAS NEVER KNOWN BEFORE*. 1962. URL: http://www.nytimes.com/1982/06/01/science/atom-by-atom-physicists-create-matter-that-nature-has-never-known-before.html.

[12] P Bogusl, Emil L Briggs, Jerzy Bernholc, et al. "Native defects in gallium nitride". In: *Physical Review B* 51.23 (1995), p. 17255.

[13] D. Briggs and M. P. Seah. *Practical surface analysis: by auger and X-ray photoelectron spectroscopy*. Wiley New York, 1983.

[14] Gang Chen. *Nanoscale energy transport and conversion: a parallel treatment of electrons, molecules, phonons, and photons*. Oxford University Press, USA, 2005. Chap. 5, p. 166.

[15] Gang Chen. *Nanoscale energy transport and conversion: a parallel treatment of electrons, molecules, phonons, and photons*. Oxford University Press, USA, 2005.

[16] Yefan Chen et al. "Plasma assisted molecular beam epitaxy of ZnO on c-plane sapphire: Growth and characterization". In: *Journal of Applied Physics* 84.7 (1998), pp. 3912–3918. DOI: http://dx.doi.org/10.1063/1.368595. URL: http://scitation.aip.org/content/aip/journal/jap/84/7/10.1063/1.368595.

[17] AY Cho and JR Arthur. "Molecular beam epitaxy". In: *Progress in solid state chemistry* 10 (1975), pp. 157–191.

[18] Supab Choopun, Hitoshi Tabata, and Tomoji Kawai. "Self-assembly ZnO nanorods by pulsed laser deposition under argon atmosphere". In: *Journal of crystal growth* 274.1 (2005), pp. 167–172.

[19] Frederik Claeyssens et al. "Studies of the plume accompanying pulsed ultraviolet laser ablation of zinc oxide". In: *Journal of applied physics* 92.11 (2002), pp. 6886–6894.

[20] A Dadgar et al. "Epitaxy of GaN on silicon impact of symmetry and surface reconstruction". In: *New Journal of Physics* 9.10 (2007), p. 389.

[21] Douglas M Detert et al. "Fermi level stabilization and band edge energies in CdxZn1-xO alloys". In: *Journal of Applied Physics* 115.23 (2014), p. 233708.

[22] F. Dimroth et al. "Four Junction Wafer-Bonded Concentrator Solar Cells". In: *IEEE JOURNAL OF PHOTOVOLTAICS* 6 (2015), pp. 343–349. ISSN: 2156-3381. DOI: 10.1109/JPHOTOV.2015.2501729.

[23] Michael John DiNezza. "Monocrystalline ZnTe/CdTe/MgCdTe Double Heterostructure Solar Cells Grown on InSb Substrates by Molecular Beam Epitaxy". In: (2014). URL: http://repository.asu.edu/attachments/140866/content/DiNezza_asu_0010E_14385.pdf.

[24] Sebastian Doniach and Ernst H Sondheimer. "Green's functions for solid state physicists". In: (1974).

[25] Victor Drits, Jan Srodon, and DD Eberl. "XRD measurement of mean crystallite thickness of illite and illite/smectite: Reappraisal of the Kubler index and the Scherrer equation". In: *Clays and clay minerals* 45.3 (1997), pp. 461–475.

[26] James H Edgar. "Properties of group III nitrides". In: Institution of Electrical Engineers. 1994.

[27] Dirk Ehrentraut, Elke Meissner, and Michal Bockowski. *Technology of gallium nitride crystal growth*. Vol. 133. Springer Science & Business Media, 2010.

[28] Albert Einstein. "Zur Elektrodynamik bewegter Körper. (German) [On the electrodynamics of moving bodies]". In: *Annalen der Physik* 322.10 (1905), pp. 891–921. DOI: http://dx.doi.org/10.1002/andp.19053221004.

[29] Klaus Ellmer and Rainald Mientus. "Carrier transport in polycrystalline ITO and ZnO: Al II: the influence of grain barriers and boundaries". In: *Thin Solid Films* 516.17 (2008), pp. 5829–5835.

[30] P Fons et al. "Growth of high-quality epitaxial ZnO films on α-Al2O3". In: *Journal of Crystal Growth* 201-202 (1999), pp. 627–632. ISSN: 0022-0248. DOI: http://dx.doi.org/10.1016/S0022-0248(98)01427-4. URL: http://www.sciencedirect.com/science/article/pii/S0022024898014274.

[31] JGE Gardeniers, ZM Rittersma, and GJ Burger. "Preferred orientation and piezoelectricity in sputtered ZnO films". In: *Journal of Applied physics* 83.12 (1998), pp. 7844–7854.

[32] Paolo Gondoni et al. "Fabrication of nano-engineered transparent conducting oxides by pulsed laser deposition". In: *Journal of visualized experiments: JoVE* 72 (2013).

[33] Jian Gong, B. Darling Seth, and Fengqi You. "Perovskite photovoltaics: life-cycle assessment of energy and environmental impacts." In: *Energy Environmental Science* 7 (2015). ISSN: 1754-5692. URL: http://search.ebscohost.com/login.aspx?direct=true&db=edsknv&AN=edsknv.ka3DNYL8B2&site=eds-live.

[34] Martin A. Green et al. "Solar cell efficiency tables (Version 45)." In: *Progress in Photovoltaics* 23.1 (2015), pp. 1–9. ISSN: 10627995. URL: http://search.ebscohost.com/login.aspx?direct=true&db=eih&AN=100066210&site=eds-live.

[35] W Guo et al. "Epitaxial ZnO films on (111) Si substrates with Sc2O3 buffer layers". In: *Applied Physics Letters* 94.12 (2009), p. 122107.

[36] Xin-Li Guo, Hitoshi Tabata, and Tomoji Kawai. "Epitaxial growth and optoelectronic properties of nitrogen doped ZnO films on (1120) Al2O3 substrate". In: *Journal of crystal growth* 237 (2002), pp. 544–547.

[37] Akihiro Hachigo et al. "Heteroepitaxial growth of ZnO films on diamond (111) plane by magnetron sputtering". In: *Applied physics letters* 65.20 (1994), pp. 2556–2558.

[38] Yoshihiro Hamakawa. *Thin-Film Solar Cells. [electronic resource] : Next Generation Photovoltaics and Its Applications.* Springer Series in Photonics: 13. Berlin, Heidelberg : Springer Berlin Heidelberg, 2004., 2004. ISBN: 9783662105498. URL: http://search.ebscohost.com/login.aspx?direct=true&db=cat04202a&AN=ucb.b21025876&site=eds-live.

[39] C. Hammond. *The basics of crystallography and diffraction.* International Union of Crystallography monographs on crystallography: 21. Oxford : Oxford University Press, 2015., 2015. ISBN: 9780191801938. URL: http://search.ebscohost.com/login.aspx?direct=true&db=cat04202a&AN=ucb.b23128513&site=eds-live.

[40] T Hanada. *Basic properties of ZnO, GaN, and related materials*. Springer, 2009, pp. 1–19.

[41] Shunichi Hayamizu et al. "Preparation of crystallized zinc oxide films on amorphous glass substrates by pulsed laser deposition". In: *Journal of applied physics* 80.2 (1996), pp. 787–791.

[42] Uzu Hisashi et al. "High efficiency solar cells combining a perovskite and a silicon heterojunction solar cells via an optical splitting system." In: *Applied Physics Letters* 106.1 (2015), pp. 1–4. ISSN: 00036951. URL: http://search.ebscohost.com/login.aspx?direct=true&db=a9h&AN=100416832&site=eds-live.

[43] John R Howell, Robert Siegel, and M Pinar Menguc. *Thermal radiation heat transfer*. CRC press, 2010.

[44] L Hsu et al. "Electron mobility in InN and III-N alloys". In: *Journal of Applied Physics* 102.7 (2007), p. 073705.

[45] Christophe A Hurni et al. "Effects of growth temperature on Mg-doped GaN grown by ammonia molecular beam epitaxy". In: *Applied Physics Letters* 101.10 (2012), p. 102106.

[46] NJ Ianno, L McConville, and N Shaikh. "Characterization of pulsed laser deposited zinc oxide". In: *MRS Proceedings*. Vol. 276. Cambridge Univ Press. 1992, p. 59.

[47] Ta ao Ishida. "GaN HEMT technologies for space and radio applications". In: (2011).

[48] Chennupati Jagadish and Stephen J Pearton. *Zinc oxide bulk, thin films and nanostructures: processing, properties, and applications*. Elsevier, 2011. Chap. 4.

[49] Anderson Janotti and Chris G Van de Walle. "Fundamentals of zinc oxide as a semiconductor". In: *Reports on Progress in Physics* 72.12 (2009), p. 126501.

[50] M Jaquez et al. "Growth and characterization of ZnO1-xSx highly mismatched alloys over the entire composition". In: *Journal of Applied Physics* 118.21 (2015), p. 215702.

[51] BJ Jin, S Im, and SY Lee. "Violet and UV luminescence emitted from ZnO thin films grown on sapphire by pulsed laser deposition". In: *Thin Solid Films* 366.1 (2000), pp. 107–110.

[52] H. Karzel et al. "Lattice dynamics and hyperfine interactions in ZnO and ZnSe at high external pressures." In: *Physical Review B (Condensed Matter)* 53.17 (1996), pp. 11425–11438. URL: http://search.ebscohost.com/login.aspx?direct=true&db=inh&AN=5295955&site=eds-live.

[53] Masanobu Kasuga and Masami Mochizuki. "Orientation relationships of zinc oxide on sapphire in heteroepitaxial chemical vapor deposition". In: *Journal of Crystal Growth* 54.2 (1981), pp. 185–194.

[54] TE Kazior. "Beyond CMOS: heterogeneous integration of III-V devices, RF MEMS and other dissimilar materials/devices with Si CMOS to create intelligent microsystems." In: *PHILOSOPHICAL TRANSACTIONS OF THE ROYAL SOCIETY A-MATHEMATICAL PHYSICAL AND ENGINEERING SCIENCES* 372.2012 (n.d.). ISSN: 1364503X. URL: http://search.ebscohost.com/login.aspx?direct=true&db=edswsc&AN=000332381100004&site=eds-live.

[55] Sang Sub Kim and Byung-Teak Lee. "Effects of oxygen pressure on the growth of pulsed laser deposited ZnO films on Si (001)". In: *Thin Solid Films* 446.2 (2004), pp. 307–312.

[56] Charles Kittel. *Introduction to solid state*. John Wiley & Sons, 1966.

[57] SA Kukushkin et al. "Substrates for epitaxy of gallium nitride: new materials and techniques". In: *Rev. Adv. Mater. Sci* 17.1/2 (2008), pp. 1–32.

[58] Byung-Teak Lee et al. "Growth and characterization of device quality ZnO on Si (111) and c-sapphire using a conventional rf magnetron sputtering". In: *Journal of electroceramics* 17.2-4 (2006), pp. 305–310.

[59] Joo-Hyoung Lee, Junqiao Wu, and Jeffrey C Grossman. "Enhancing the thermoelectric power factor with highly mismatched isoelectronic doping". In: *Physical review letters* 104.1 (2010), p. 016602.

[60] Alejandro X Levander et al. "Growth and transport properties of p-type GaNBi alloys". In: *Journal of Materials Research* 26.23 (2011), pp. 2887–2894.

[61] SX Li et al. "Fermi-level stabilization energy in group III nitrides". In: *Physical Review B* 71.16 (2005), p. 161201.

[62] Ying Liu et al. "Ultraviolet detectors based on epitaxial ZnO films grown by MOCVD". In: *Journal of Electronic Materials* 29.1 (2000), pp. 69–74.

[63] David C Look et al. "Electrical properties of bulk ZnO". In: *Solid state communications* 105.6 (1998), pp. 399–401.

[64] M Lorenz et al. "Room-temperature cathodoluminescence of n-type ZnO thin films grown by pulsed laser deposition in N 2, N 2 O, and O 2 background gas". In: *Thin Solid Films* 486.1 (2005), pp. 205–209.

[65] "Zinc oxide (ZnO) distances, ionic radii, further lattice parameters". English. In: *II-VI and I-VII Compounds; Semimagnetic Compounds*. Ed. by O. Madelung, U. Rassler, and M. Schulz. Vol. 41B. Landolt-Bornstein - Group III Condensed Matter. Springer Berlin Heidelberg, 1999, pp. 1–4. ISBN: 978-3-540-64964-9. DOI: 10.1007/10681719_287. URL: http://dx.doi.org/10.1007/10681719_287.

[66] Otfried Madelung. *Semiconductors: group IV elements and III-V compounds*. Springer Science & Business Media, 2012.

[67] J.P. Mailoa et al. "A 2-terminal perovskite/silicon multijunction solar cell enabled by a silicon tunnel junction." In: *Applied Physics Letters* 106.12 (2015), p. 121105. URL: http://search.ebscohost.com/login.aspx?direct=true&db=inh&AN=14998789&site=eds-live.

[68] M. A. Mayer et al. "Electronic structure of $Ga_{1-x}Mn_xAs$ analyzed according to hole-concentration-dependent measurements". In: *Phys. Rev. B* 81 (4 Jan. 2010), p. 045205. DOI: 10.1103/PhysRevB.81.045205. URL: http://link.aps.org/doi/10.1103/PhysRevB.81.045205.

[69] Marie Annette Mayer. *Band structure engineering for solar energy applications : ZnO1-xSex films and devices. [electronic resource]*. Berkeley, CA, 2012., 2012. URL: http://search.ebscohost.com/login.aspx?direct=true&db=cat04202a&AN=ucb.b20247958&site=eds-live.

[70] Marie A. Mayer et al. "Band Gap Engineering of Oxide Photoelectrodes: Characterization of $ZnO_{1-x}Se_x$". In: *The Journal of Physical Chemistry C* 116.29 (2012), pp. 15281–15289. DOI: 10.1021/jp304481c. eprint: http://dx.doi.org/10.1021/jp304481c. URL: http://dx.doi.org/10.1021/jp304481c.

[71] Marie A. Mayer et al. "Band structure engineering of $ZnO_{1-x}Se_x$ alloys". In: *Applied Physics Letters* 97.2, 022104 (2010). DOI: http://dx.doi.org/10.1063/1.3464323. URL: http://scitation.aip.org/content/aip/journal/apl/97/2/10.1063/1.3464323.

[72] Matthew D. McCluskey and Eugene E. Haller. *Dopants and defects in semiconductors*. Boca Raton, FL : CRC Press, c2012., 2012. ISBN: 9781439831526. URL: http://search.ebscohost.com/login.aspx?direct=true&db=cat04202a&AN=ucb.b18613512&site=eds-live.

[73] W Patrick McCray. "MBE deserves a place in the history books". In: *Nature nanotechnology* 2.5 (2007), pp. 259–261.

[74] Farid Medjdoub. *Gallium Nitride (GaN): Physics, Devices, and Technology*. Vol. 47. CRC Press, 2015.

[75] S.J Moon et al. "The dependence of the structural and optical properties on the Te mole fraction in $ZnS_{1-x}Te_x$/GaAs heterostructures." In: *Journal of Physics and Chemistry of Solids* 64 (2003), pp. 535–538. ISSN: 0022-3697. URL: http://search.ebscohost.com/login.aspx?direct=true&db=edselp&AN=S0022369702002883&site=eds-live.

[76] Nevill Francis Mott and Edward A Davis. *Electronic processes in non-crystalline materials*. OUP Oxford, 2012.

[77] John F Moulder, Jill Chastain, and Roger C King. *Handbook of X-ray photoelectron spectroscopy: a reference book of standard spectra for identification and interpretation of XPS data*. Perkin-Elmer Eden Prairie, MN, 1992.

[78] Shuji Nakamura et al. "Thermal annealing effects on p-type Mg-doped GaN films". In: *Japanese Journal of Applied Physics* 31.2B (1992), p. L139.

[79] Lothar Nordheim. "Zur Elektronentheorie der Metalle. I." In: *Annalen der Physik* 401.5 (1931), p. 607. ISSN: 00033804. URL: http://search.ebscohost.com/login.aspx?direct=true&db=edb&AN=91300869&site=eds-live.

[80] Juan E Peralta et al. "Spin-orbit splittings and energy band gaps calculated with the Heyd-Scuseria-Ernzerhof screened hybrid functional". In: *Physical Review B* 74.7 (2006), p. 073101.

[81] *Photovoltaics Report*. Tech. rep. Fraunhofer Institute, Nov. 2015.

[82] HL Porter et al. "Enhanced photoconductivity of ZnO films Co-doped with nitrogen and tellurium". In: *Applied Physics Letters* 86.21 (2005), p. 1918.

[83] HL Porter et al. "Enhanced photoconductivity of ZnO films Co-doped with nitrogen and tellurium". In: *Applied Physics Letters* 86.21 (2005), p. 1918.

[84] Lothar A Reichertz et al. "Demonstration of a III–nitride/silicon tandem solar cell". In: *Applied physics express* 2.12 (2009), p. 122202.

[85] Zhibin Ren et al. "The ballistic nanotransistor: A simulation study". In: *Electron Devices Meeting, 2000. IEDM'00. Technical Digest. International*. IEEE. 2000, pp. 715–718.

[86] M. Repoux. "Comparison of background removal methods for XPS". In: *Surface and Interface Analysis* 18 (1992), pp. 567–570.

[87] D Richardson and R Hill. "The origins of energy gap bowings in substitutional semiconductor alloys". In: *Journal of Physics C: Solid State Physics* 5.8 (1972), p. 821. URL: http://stacks.iop.org/0022-3719/5/i=8/a=008.

[88] A Sarkar et al. "Studies on electron transport properties and the Burstein-Moss shift in indium-doped ZnO films". In: *Thin Solid Films* 204.2 (1991), pp. 255–264.

[89] Christof W Schneider and Thomas Lippert. "Laser ablation and thin film deposition". In: *Laser Processing of Materials*. Springer, 2010, pp. 89–112.

[90] Natalie Segercrantz et al. "Increased p-type conductivity in GaNxSb1- x, experimental and theoretical aspects". In: *Journal of Applied Physics* 118.8 (2015), p. 085708.

[91] N Segercrantz et al. "Electronic band structure of highly mismatched GaN1- xSbx alloys in a broad composition range". In: *Applied Physics Letters* 107.14 (2015), p. 142104.

[92] W. Shan et al. "Band anticrossing in GaInNAs alloys." In: *Physical Review Letters* 82.6 (1999), pp. 1221–1224. URL: http://search.ebscohost.com/login.aspx?direct=true&db=inh&AN=6180424&site=eds-live.

[93] William Shockley and Hans J. Queisser. "Detailed Balance Limit of Efficiency of p-n Junction Solar Cells." In: *Journal of Applied Physics* 32.3 (1961), p. 510. ISSN: 00218979. URL: http://search.ebscohost.com/login.aspx?direct=true&db=edb&AN=73287033&site=eds-live.

[94] Michael S Shur. *Handbook series on semiconductor parameters*. Vol. 1. World Scientific, 1996.

[95] V Srikant and D R_ Clarke. "On the optical band gap of zinc oxide". In: *Journal of Applied Physics* 83.10 (1998), pp. 5447–5451.

[96] P Swift. "Adventitious carbon–The panacea for energy referencing?" In: *Surface and Interface Analysis* 4.2 (1982), pp. 47–51.

[97] MC Tarun, M Zafar Iqbal, and MD McCluskey. "Nitrogen is a deep acceptor in ZnO". In: *Aip Advances* 1.2 (2011), p. 022105.

[98] *Thickness Effect of Al-Doped ZnO Window Layer on Damp Heat Stability of CuInGaSe2 Solar Cells. [electronic resource] : Preprint*. Washington, D.C. : United States. Dept. of Energy. Office of Solar Electric Technology, 2011, 2011. URL: http://search.ebscohost.com/login.aspx?direct=true&db=cat04202a&AN=ucb.b21222112&site=eds-live.

[99] A. G. Thompson and J. C. Woolley. "Energy gap variation in mixed III-V alloys." In: *Canadian Journal of Physics* 45.2 (1967), pp. 255–261. DOI: 10.1139/p67-026. URL: http://stacks.iop.org/0022-3719/5/i=8/a=008.

[100] SK Tiku, CK Lau, and KM Lakin. "Chemical vapor deposition of ZnO epitaxial films on sapphire". In: *Applied Physics Letters* 36.4 (1980), pp. 318–320.

[101] M Ting et al. "Electronic band structure of ZnO-rich highly mismatched ZnO1- xTex alloys". In: *Applied Physics Letters* 106.9 (2015), p. 092101.

[102] RJ Trew. "SiC and GaN transistors-is there one winner for microwave power applications?" In: *Proceedings of the IEEE* 90.6 (2002), pp. 1032–1047.

[103] Terry M Tritt. *Thermal conductivity: theory, properties, and applications*. Springer Science & Business Media, 2004. Chap. 1.2, p. 36.

[104] Atsushi Tsukazaki et al. "Blue light-emitting diode based on ZnO". In: *Japanese Journal of Applied Physics* 44.5L (2005), p. L643.

[105] Raymond T Tung. "Chemical bonding and Fermi level pinning at metal-semiconductor interfaces". In: *Physical review letters* 84.26 (2000), p. 6078.

[106] K. Uesugi, N. Morooka, and I. Suemune. "Reexamination of N composition dependence of coherently grown GaNAs band gap energy with high-resolution X-ray diffraction mapping measurements." In: *Applied Physics Letters* 74.9 (1999), pp. 1254–1256. URL: http://search.ebscohost.com/login.aspx?direct=true&db=inh&AN=6176578&site=eds-live.

[107] Chris G Van de Walle and Jörg Neugebauer. "First-principles calculations for defects and impurities: Applications to III-nitrides". In: *Journal of Applied Physics* 95.8 (2004), pp. 3851–3879.

[108] B Velickỳ. "Theory of electronic transport in disordered binary alloys: Coherent-potential approximation". In: *Physical Review* 184.3 (1969), p. 614.

[109] P Vennegues et al. "Influence of high Mg doping on the microstructural and optoelectronic properties of GaN". In: *Materials Science and Engineering: B* 93.1 (2002), pp. 224–228.

[110] R. D. Vispute et al. "Heteroepitaxy of ZnO on GaN and its implications for fabrication of hybrid optoelectronic devices". In: *Applied Physics Letters* 73.3 (1998), pp. 348–350. DOI: http://dx.doi.org/10.1063/1.121830. URL: http://scitation.aip.org/content/aip/journal/apl/73/3/10.1063/1.121830.

[111] I. Vurgaftman and J.R. Meyer. "Band parameters for nitrogen-containing semiconductors." In: *Journal of Applied Physics* 94.6 (2003), p. 3675. ISSN: 00218979. URL: http://search.ebscohost.com/login.aspx?direct=true&db=a9h&AN=11026091&site=eds-live.

[112] W Walukiewicz. "Amphoteric native defects in semiconductors". In: *Applied physics letters* 54.21 (1989), pp. 2094–2096.

[113] W. Walukiewicz et al. "Interaction of Localized Electronic States with the Conduction Band: Band Anticrossing in II-VI Semiconductor Ternaries". In: *Phys. Rev. Lett.* 85 (7 Aug. 2000), pp. 1552–1555. DOI: 10.1103/PhysRevLett.85.1552. URL: http://link.aps.org/doi/10.1103/PhysRevLett.85.1552.

[114] W. Walukiewicz et al. "Interaction of localized electronic states with the conduction band: band anticrossing in II-VI semiconductor ternaries." In: *Physical Review Letters* 85.7 (2000), pp. 1552–1555. URL: http://search.ebscohost.com/login.aspx?direct=true&db=inh&AN=6707682&site=eds-live.

[115] W Wang et al. "Optical characteristics of ZnTeO thin films synthesized by pulsed laser deposition and molecular beam epitaxy". In: *Journal of Electronic Materials* 38.1 (2009), pp. 119–125.

[116] Jue Wei et al. "Pulsed laser deposition of zinc oxide luminescent thin films". In: *Journal of Vacuum Science & Technology B* 19.3 (2001), pp. 1082–1084.

[117] Jeremie Werener, Ching-Hsun Weng, and Arnaud Walter. "Efficient Monolithic Perovskite/Silicon Tandem Solar Cell with Cell Area > 1 cm^2." In: *The Journal of Physical Chemistry Letters* 7 (2015). DOI: 10.1021/acs.jpclett.5b02686. URL: http://pubs.acs.org/doi/abs/10.1021/acs.jpclett.5b02686.

[118] J Wu, W Shan, and W Walukiewicz. "Band anticrossing in highly mismatched III-V semiconductor alloys". In: *Semiconductor Science and Technology* 17.8 (2002), p. 860. URL: http://stacks.iop.org/0268-1242/17/i=8/a=315.

[119] J Wu, W Shan, and W Walukiewicz. "Band anticrossing in highly mismatched III–V semiconductor alloys". In: *Semiconductor Science and Technology* 17.8 (2002), p. 860.

[120] Junqiao Wu. *Band anticrossing effects in highly mismatched semiconductor alloys. [electronic resource].* 2002., 2002. URL: http://search.ebscohost.com/login.aspx?direct=true&db=cat04202a&AN=ucb.b21323318&site=eds-live.

[121] Junqiao Wu. *Semiconductor Materials*. University Lecture. 2013.

[122] J. Wu et al. "Origin of the large band-gap bowing in highly mismatched semiconductor alloys". In: *Phys. Rev. B* 67 (3 Jan. 2003), p. 035207. DOI: 10.1103/PhysRevB.67.035207. URL: http://link.aps.org/doi/10.1103/PhysRevB.67.035207.

[123] J. Wu et al. "Valence band hybridization in N-rich $GaN_{1-x}As_x$ alloys". In: *Phys. Rev. B* 70 (11 Sept. 2004), p. 115214. DOI: 10.1103/PhysRevB.70.115214. URL: http://link.aps.org/doi/10.1103/PhysRevB.70.115214.

[124] Masafumi Yamaguchi et al. "Multi-junction III V solar cells: current status and future potential". In: *Solar Energy* 79.1 (2005), pp. 78–85. ISSN: 0038-092X. DOI: http://dx.doi.org/10.1016/j.solener.2004.09.018. URL: http://www.sciencedirect.com/science/article/pii/S0038092X04002944.

[125] Takafumi Yao and Soon-Ku Hong. *Oxide and nitride semiconductors. [electronic resource] : processing, properties and applications.* Advances in materials research: 12. Berlin ; London : Springer, 2009, 2009. ISBN: 9783540888475. URL: http://search.ebscohost.com/login.aspx?direct=true&db=cat04202a&AN=ucb.b18037386&site=eds-live.

[126] KM Yu et al. "Diluted II-VI oxide semiconductors with multiple band gaps". In: *Physical Review Letters* 91.24 (2003), p. 246403.

[127] KM Yu et al. "Effects of native defects on properties of low temperature grown, non-stoichiomtric gallium nitride". In: *Journal of Physics D: Applied Physics* 48.38 (2015), p. 385101.

[128] KM Yu et al. "Growth and characterization of highly mismatched GaN1- xSbx alloys". In: *Journal of Applied Physics* 116.12 (2014), p. 123704.

[129] KM Yu et al. "Highly mismatched crystalline and amorphous GaN1- xAsx alloys in the whole composition range". In: *Journal of Applied Physics* 106.10 (2009), p. 103709.

[130] K.M. Yu et al. "Synthesis of GaNxAs1-x thin films by pulsed laser melting and rapid thermal annealing of N+-implanted GaAs." In: *Journal of Applied Physics* 94.2 (2003), pp. 1043–1049. URL: http://search.ebscohost.com/login.aspx?direct=true&db=inh&AN=7674885&site=eds-live.

[131] Young-Moon Yu et al. "Variation of band gap energy and photoluminescence characteristics with Te composition of $ZnS_{1-x}Te_x$ epilayers grown by hot-wall epitaxy." In: *Applied Surface Science* 182 (2001), pp. 159–166. ISSN: 0169-4332. URL: http://search.ebscohost.com/login.aspx?direct=true&db=edselp&AN=S0169433201005505&site=eds-live.

[132] BL Zhu et al. "The effects of substrate temperature on the structure and properties of ZnO films prepared by pulsed laser deposition". In: *Vacuum* 82.5 (2008), pp. 495–500.